CHAPTER VI

Spanwise Data

As noted in §1.2, this chapter provides the first detailed velocity measurements of a three-dimensional inlet shock wave boundary layer (3DI-SBLI) imaged from the centerline all the way into the corner. Two spanwise planes, TV1 and TV2, were recorded upstream of the interaction and image the entire tunnel span. A third spanwise plane, TV10, also images the entire span downstream of the interaction. Data from these 'full span' (FS) planes, $54 \times 35\, mm^2$, are not 'full span' because light reflections obscure $\approx 1.5\, mm$ from the sidewall glass. Reflection from the bottom wall also obscures data taking by $\approx 1\, mm$. Seven spanwise planes, TV3-TV9, focus on the corner through the 3DI-SBLI region, or 'interaction region' (IR). These image planes are $25 \times 35\, mm^2$ and focus on the bottom left corner of the wind tunnel looking upstream. The locations of the data planes (excluding TV1) are shown in Fig. 6.1. The planes are labeled TV designating they are oriented with the transverse (i.e. spanwise) vertical direction and the numbering scheme starts closest to the nozzle exit, with increasing numbers indicating movement downstream. The locations TV3 through TV9 appear to miss the invicid shock reflection point, however the viscous interaction foot moves upstream(not pictured) and the reflection region begins closer to $x = 80\, mm$. The transverse planes begin upstream slightly and capture and track

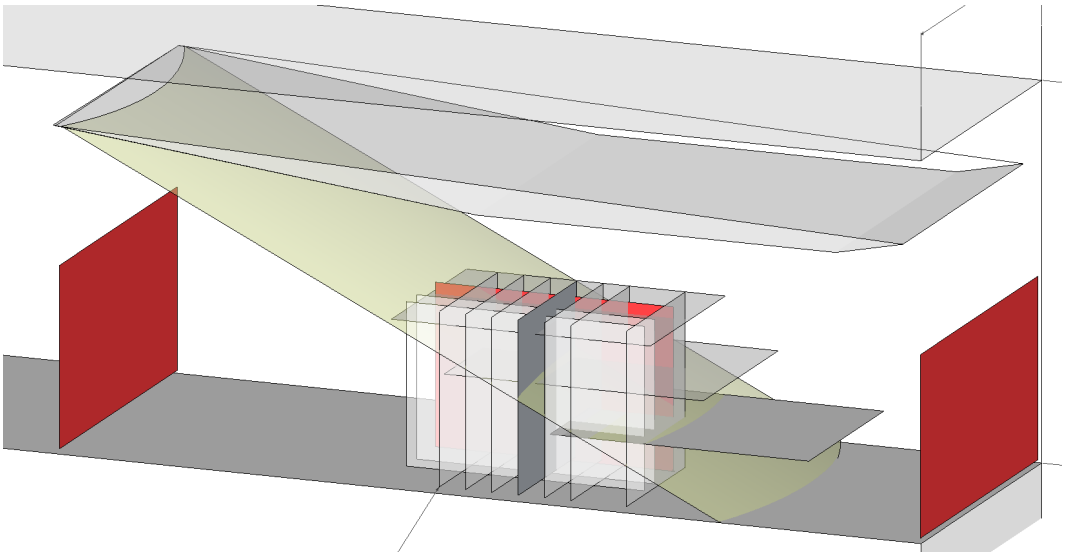

Figure 6.1: Scale drawing of the location of the data planes relative to the shock generator and the inviscid shock location(yellow). Table 6.1 provides labels and locations for each plane pictured except for TV1, the most upstream data plane, which is only pictured in Fig. 3.1.

the motion of coherent streamwise vorticity predicted by the SFSC using a CPT description of the oil flow.

However before that, the spanwise planes are first used to asses variation in the boundary layer health over the tunnel width. Then prominent three-dimensional features of the interaction in the sidewall that were explained by the secondary flow separation concept (SFSC) are assessed using the streamwise vorticity component, ω_x.

6.1 Boundary Condition Assessment

Traditional inlet boundary layer investigations are limited to streamwise data taken along the tunnel centerline. Interpreting the usage of these profiles give the impression that the boundary layer has no spanwise variability, that it, it assumes that flows are two-dimensional! As we stated from the outset, the purpose of the current work is to presume the opposite. Thus boundary layer studies were performed

Image Plane	x[mm]	y[mm]	z[mm]
TV1(FS)	-144	1-36	1.5-54.5
TV2(FS)	0	1-30	1.5-54.5
TV3(IR)	71	1-25	2-35
TV4(IR)	76	1-25	2-35
TV5(IR)	81	1-25	2-35
TV6(IR)	86	1-25	2-35
TV7(IR)	91	1-25	2-35
TV8(IR)	96	1-25	2-35
TV9(IR)	107	1-25	2-35
TV10(FS)	160	1-36	1.5-54.5

Table 6.1: Image Plane Streamwise Locations, $x = 0$ at Shock Generator Leading Edge (for reference geometry see please Appendix A.)

in the transverse plane to attempt to provide measurements of three-dimensionality variability induced by the geometrical effects.

Figure 6.2 presents the velocity profile in the boundary layer corner at $x = 0\,mm$. Presuming that the boundary layer below the shock impingement at TV3 can be characterized as an 'unperturbed' boundary layer, an analysis of the numerical data was performed to assess how the boundary layer properties vary across the span and between the streamwise and spanwise planes. This technique uses a discrete trapezoidal integration method to calculate displacement and momentum thickness from the averaged velocity data. However, the lack of information in the region closest to the wall boundary layer can significantly alter these results for displacement and momentum thickness.

Previous studies to characterize the mean boundary layer behavior had predicted a boundary layer height of $10\,mm$ entering the interaction. Table 6.3 compares previous values from inflow planes of Lapsa (2009) to the current study.

	SV1 x=71	TV3 z=28	SV3 x=71	TV3 z= 17
U_∞,(m/s)	595	605	593	598
δ (mm)	8.74	9.60	9.2	9.9
δ^* (mm)	1.0	1.3	1.8	1.9
θ (mm)	0.7	0.9	1.0	1.3
H	1.37	1.37	1.73	1.47
Re_{δ^*}	8,500	11000	15,700	15900
Re_θ	6,200	8000	9,100	10800

Table 6.2: Comparison of two spanwise locations at $x = 71\,mm$ showing the boundary layer thickness, δ, displacement thickness δ^*, momentum thickness θ, shape factor H, associated Reynolds numbers computed in streamwise and spanwise planes.

	$x = -182$	$x = -25$	(TV2) x = -120	(SV3) x = -60
U_∞,(m/s)	613(?)	613(?)	600	593
δ (mm)	6.3	10.0	5.17	9.22
δ^* (mm)	1.03	1.47	0.51	1.8
θ (mm)	0.74	1.08	0.39	1.0
H	1.40	1.36	1.3	1.7
Re_{δ^*}	9,200	13,100	4,500	15,700
Re_θ	6,600	9,600	3,500	9100

Table 6.3: Boundary layer quantities at the two previous upstream locations(relative to inviscid shock foot), and two current measurements ($\sim$ relative to shock foot) showing the boundary layer thickness δ, displacement thickness δ^*, momentum thickness θ, shape factor H, associated Reynolds numbers.

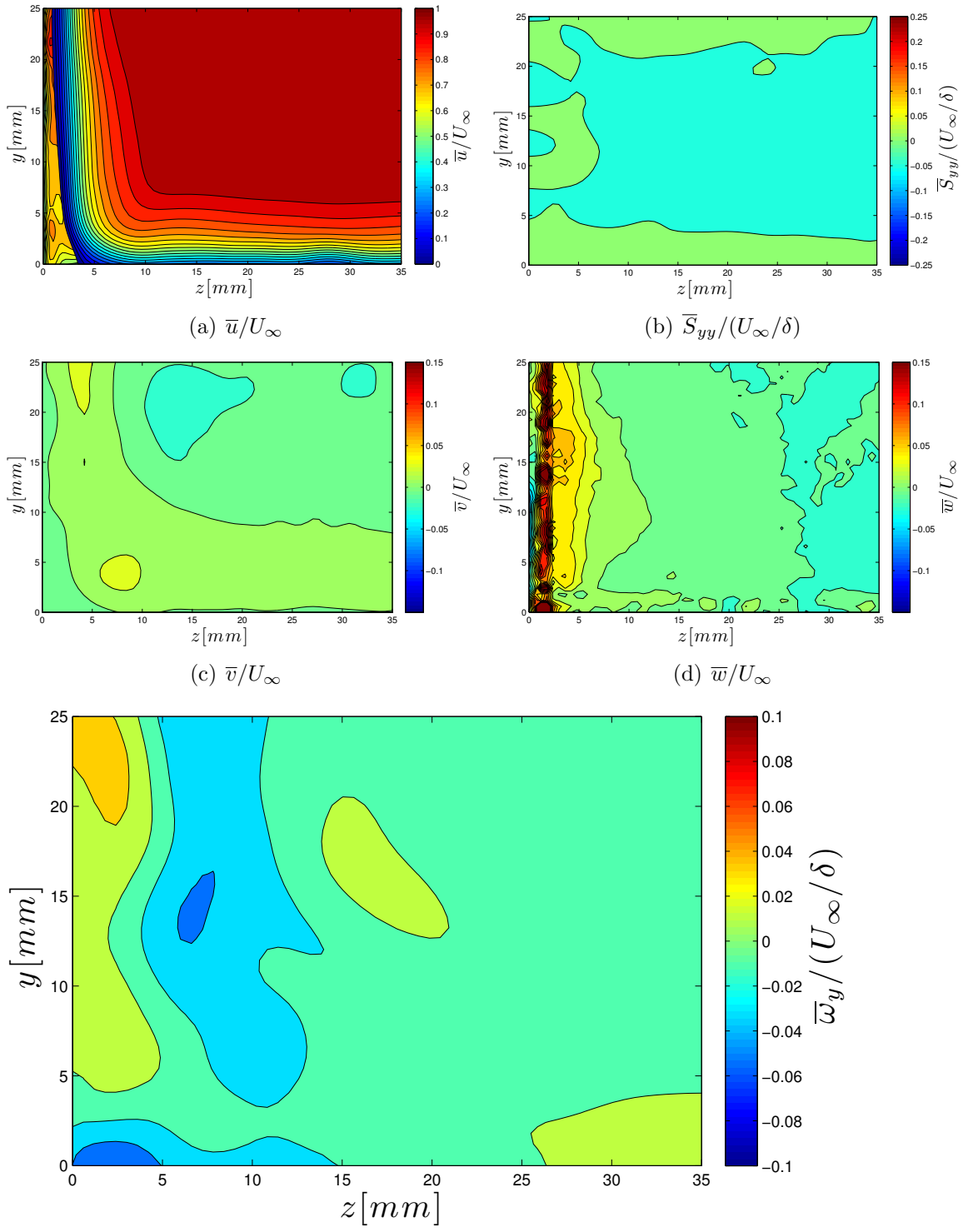

(a) $\overline{u}/U_\infty$

(b) $\overline{S}_{yy}/(U_\infty/\delta)$

(c) $\overline{v}/U_\infty$

(d) $\overline{w}/U_\infty$

(e) $\overline{\omega}_z/(U_\infty/\delta)$

Figure 6.2: Velocities: streamwise(a), vertical(b), transverse(c), computed streamwise normal strain(d) and streamwise vorticity(e) at $x = 0\,mm$ (plane TV2.)

6.2 Three-Dimensionality in the Interaction

This section outlines the three-dimensionality present in the 3DI-SBLI. As with the previous SBLI data, each figure (e.g. Fig. 6.3) will present three components of velocity (Fig. 6.3a-c), a computed normal strain (Fig. 6.3d) and the vorticity (Fig. 6.3e). The contours of streamwise velocity component (see Fig. 6.3a) can be used to deduce three dimensionality of the boundary layer. The vertical velocity contours (see Fig.6.3b) depict the incoming shock since down flow occurs above the shock wave, as well as the foot of the reflected region where upwash occurs. The transverse velocity (see Fig. 6.3c) is useful to confirm secondary flow towards the centerline ahead of shock impingement. The PIV data confirms the secondary flow separation concept explanation of the oil flow, i.e. that this secondary flow is driven by a half a horseshoe vortex created in the bottom wall, moving away from the corner towards the centerline (see Fig. 6.3e - 6.5e.) In Fig. 6.3d, the normal strain is a good quantitative look at the compression strength (negative strain) induced by the shock and the variation in shock strength across the tunnel.

The impinging shock, visualized by the normal strain, S_{yy}, in Fig. 6.3d is highly three-dimensional across the narrow wind tunnel. In agreement with previous data, it shows a dramatic curvature across the entire span, and a discernible decrease in the shock strength as the side wall boundary layer is approached.

Presented in Fig. 6.3c, the transverse velocity confirms the secondary flow towards the tunnel centerline that was observed in the spanwise image planes. Along the sidewall, there is significant down flow caused by the superposition of the two-dimensional flow caused by the impinging shock and the vortex flow bound under the shock foot. This is apparent in Fig. 6.3(c). However, the primary benefit of the

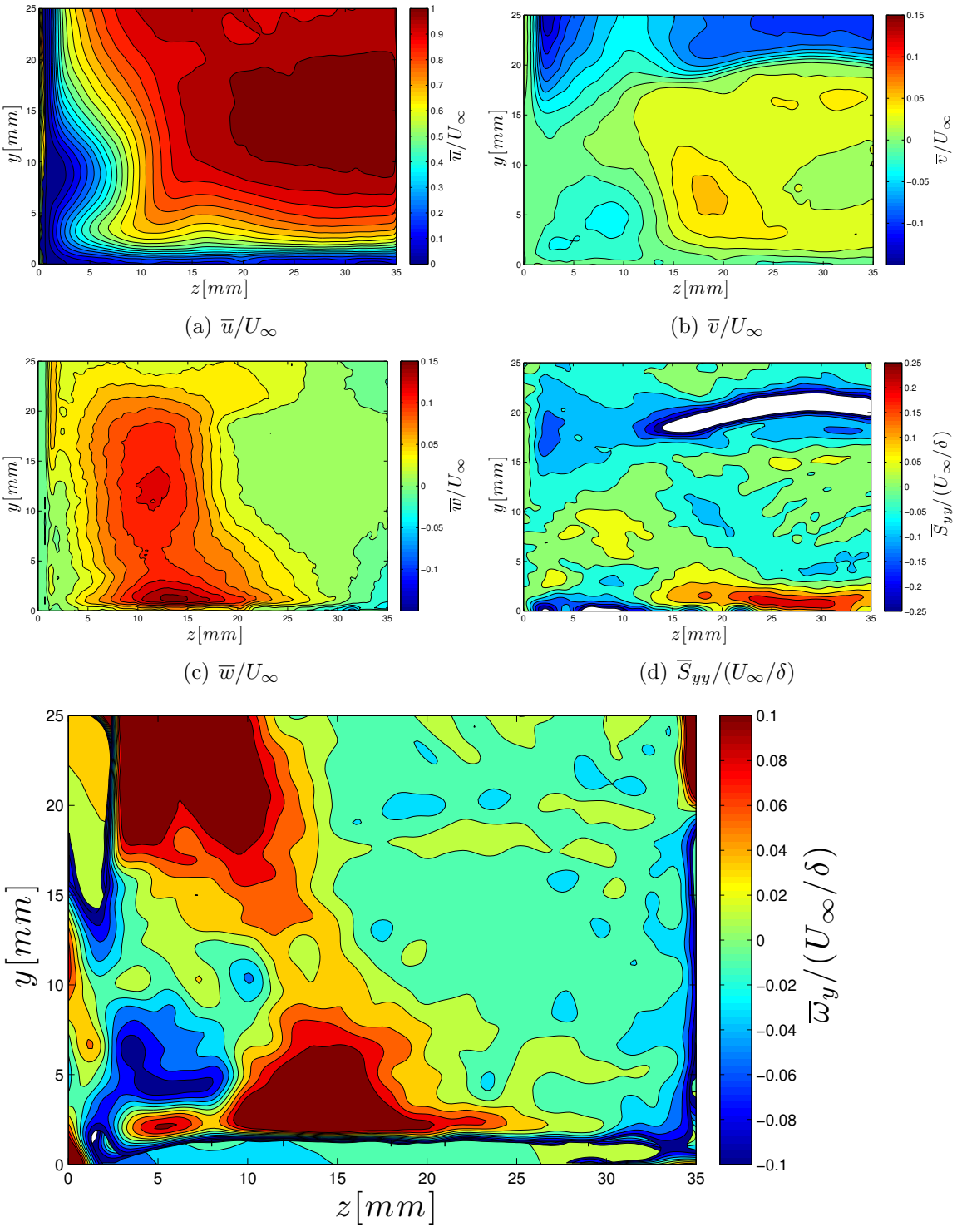

(a) $\overline{u}/U_\infty$ (b) $\overline{v}/U_\infty$

(c) $\overline{w}/U_\infty$ (d) $\overline{S}_{yy}/(U_\infty/\delta)$

(e) $\overline{\omega}_z/(U_\infty/\delta)$

Figure 6.3: Velocities: streamwise(a), vertical(b), transverse(c), computed normal strain(d) and streamwise vorticity(e) $x = 76\,mm$ (plane TV4.)

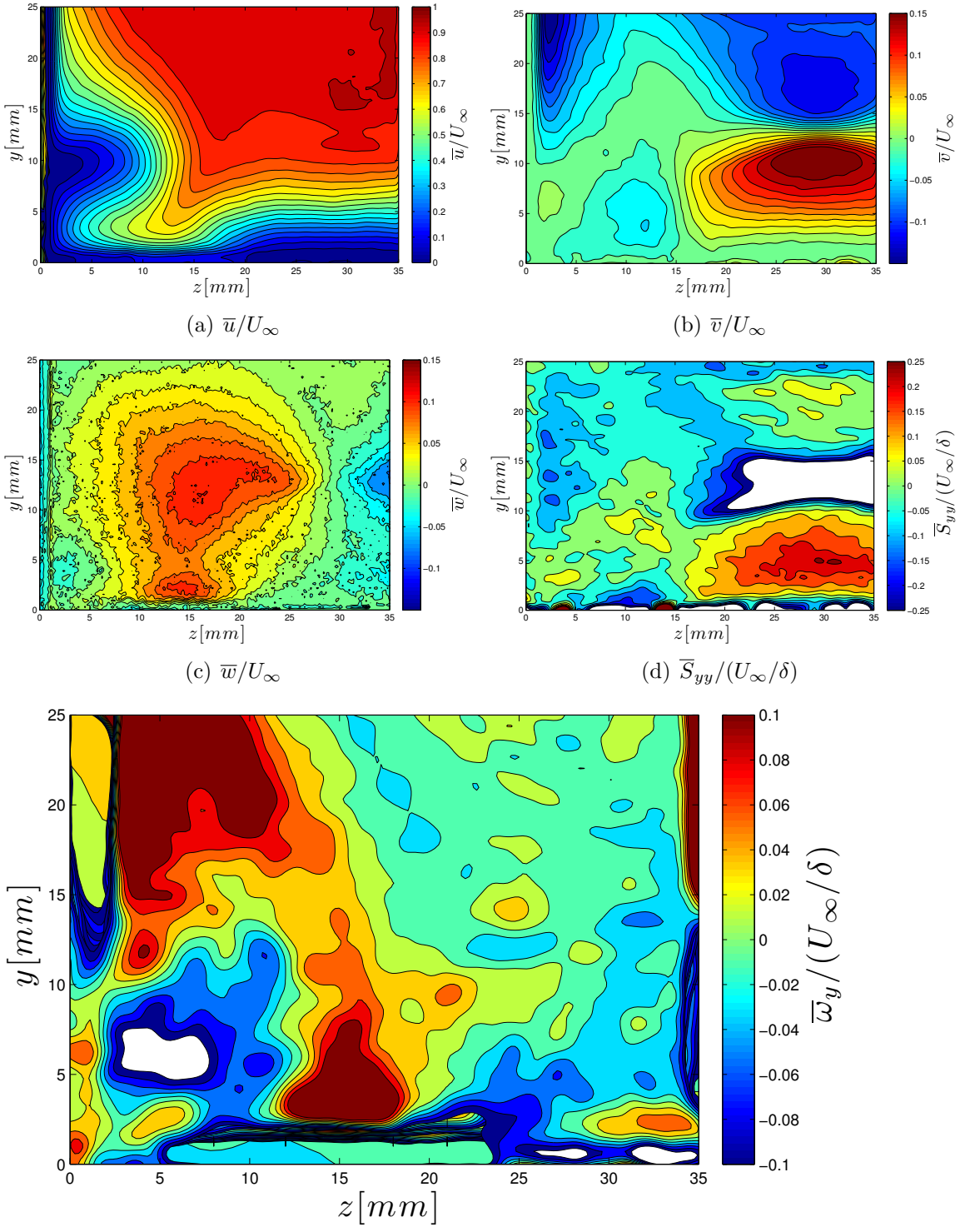

(a) $\overline{u}/U_\infty$

(b) $\overline{v}/U_\infty$

(c) $\overline{w}/U_\infty$

(d) $\overline{S}_{yy}/(U_\infty/\delta)$

(e) $\overline{\omega}_z/(U_\infty/\delta)$

Figure 6.4: Velocities: streamwise(a), vertical(b), transverse(c), computed normal strain(d) and streamwise vorticity(e) $x = 91\,mm$ (plane TV7.)

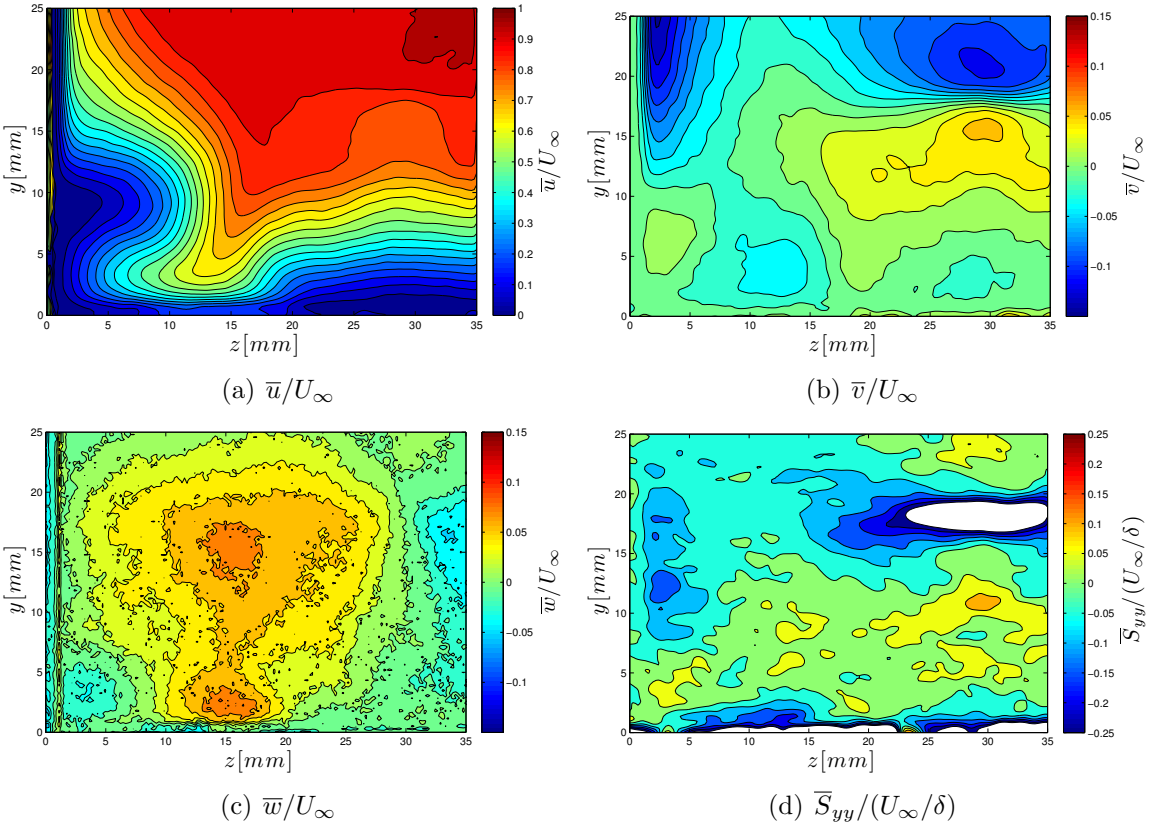

(a) $\overline{u}/U_\infty$ (b) $\overline{v}/U_\infty$

(c) $\overline{w}/U_\infty$ (d) $\overline{S}_{yy}/(U_\infty/\delta)$

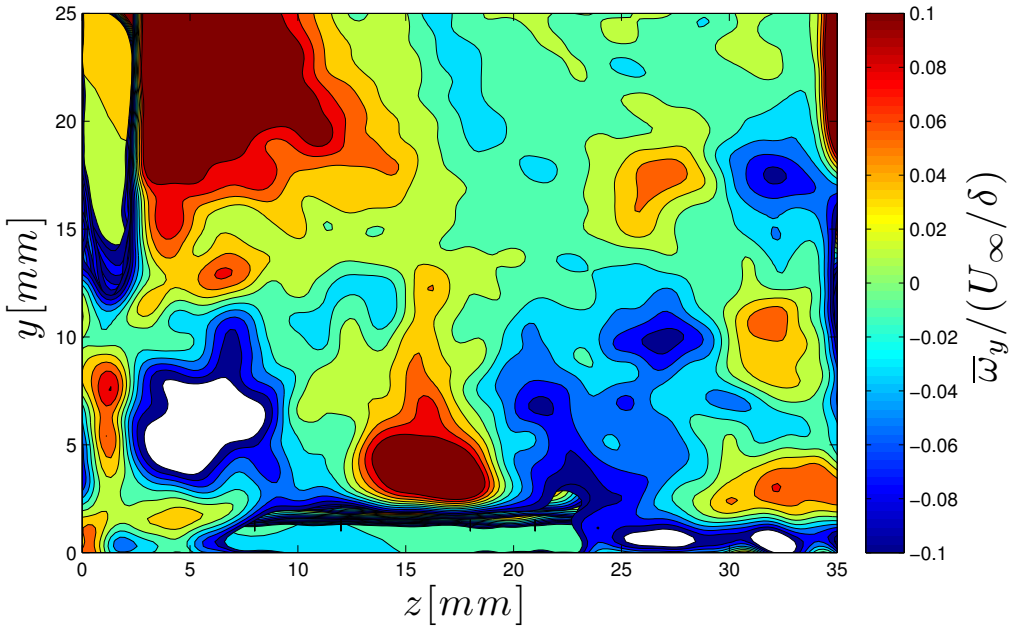

(e) $\overline{\omega}_z/(U_\infty/\delta)$

Figure 6.5: Velocities: streamwise(a), vertical(b), transverse(c), computed normal strain(d) and streamwise vorticity(e) $x = 96\,mm$ (plane TV8.)

spanwise planes is the determination of the streamwise vorticity. This metric will be used in the next section to evaluate the SFSC.

6.3 Vorticity in the Corner Interaction

Tracking the generation of vorticity through the interaction allows for a quantitative evaluation of the secondary flow separation concept. Upstream of the interaction, vorticity in the boundary layers is concentrated strictly close to the wall with diffusion and turbulence in the boundary layer producing a gradient towards the free stream. From Fig. 6.3e - 6.5e, the notable corner motion of the vortex cores is discussed below (See Appendix D for all image planes.)

A large region of positive vorticity along the sidewall is indicative of the vortex structure which propagates with the impinging shock. While in the corner, a large negative vorticity region concentrates immediately downstream of the fin-plate interaction point, but ahead of the inviscid shock location. Immediately to the right, and moving towards the centerline the last large pocket of vorticity in Fig. 6.3(e) merges towards the centerline drawn there by the significant spanwise flow visible in Fig. 6.3(d). This large region of positive vorticity mirrors with a large region of negative vorticity from the other sidewall which merge at the centerline ($z = 28\,mm$). Underneath the shock foot on the sidewall is a large positive component of vorticity. This vorticity component has been discussed before, and is generated and maintained by the fin-plate interaction. In tracking the motion of all these vortexes through the data planes, note that the 'primary' separations remain close to the walls, while the secondary separation appears to leave the wall surface, leaving behind vorticity on the wall which is of the opposite sign.

The symmetry about the mid-plane is apparent in the shock curvature and in the spanwise flows which go to zero near the centerline. The convergence of the spanwise flow in Figs. 6.3 and 6.4(c) confirms that a nodal point is present at the centerline upstream of the separation, consistent with the SFSC. Visible in Figs. 6.4(e) and 6.5(e) along the centerline are smaller pockets of vorticity in the vicinity of the reflected shock 6.4(b). The lift off of these vortical structures from the floor of the tunnel is particularly apparent in 6.5(e). This confirms the picture of secondary separation as the liftoff of counter rotating vortical structures which have merged at the centerline.

Examining TV8 using a using the vortex line method in Fig. 6.6, we see that the shock wave in three-dimensions also appears as a node, the corner region appears as a focus in the flow, and several saddle points separate boundary layer flows from the rest. Vortex lines for are TV1 and TV10 full span boundary conditions are plotted in Figs. 6.7 and 6.8. Upstream the slight asymmetry is exaggerated by the visualization method, while the downstream plane, described in detail in the next section, shows good symmetry.

6.4 Downstream Boundary

The outflow boundary condition is shown in Fig. 6.9. This measurement location is sufficiently far downstream to allow for some boundary layer relaxation to take place after the SBLI. By this location the magnitude of the spanwise flows have abated to less than 10% of the free stream. However, non-uniform cross flow is still visible as is the boundary layer thickening due to the streamwise vorticity generated in the interaction region. Particularly notable are the two visible boundary layer

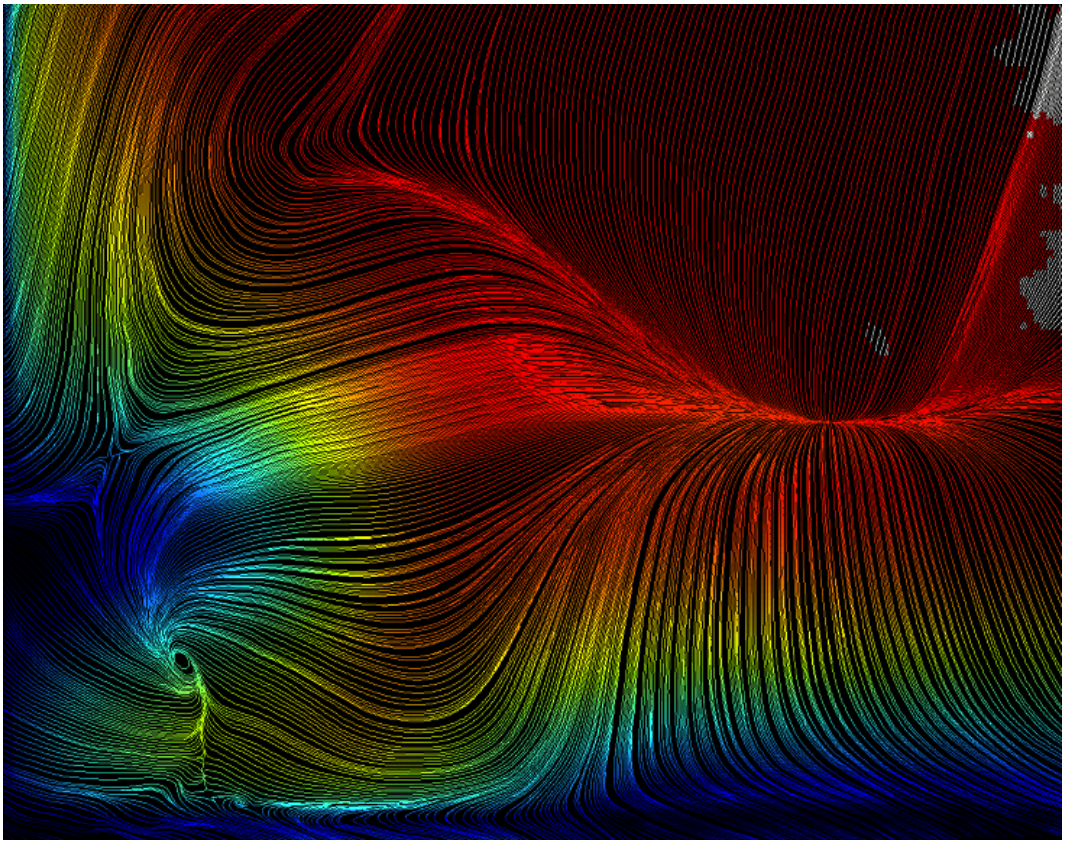

Figure 6.6: Vortex lines of TV8, downstream of impingement showing corner focus and boundary layer saddle points.

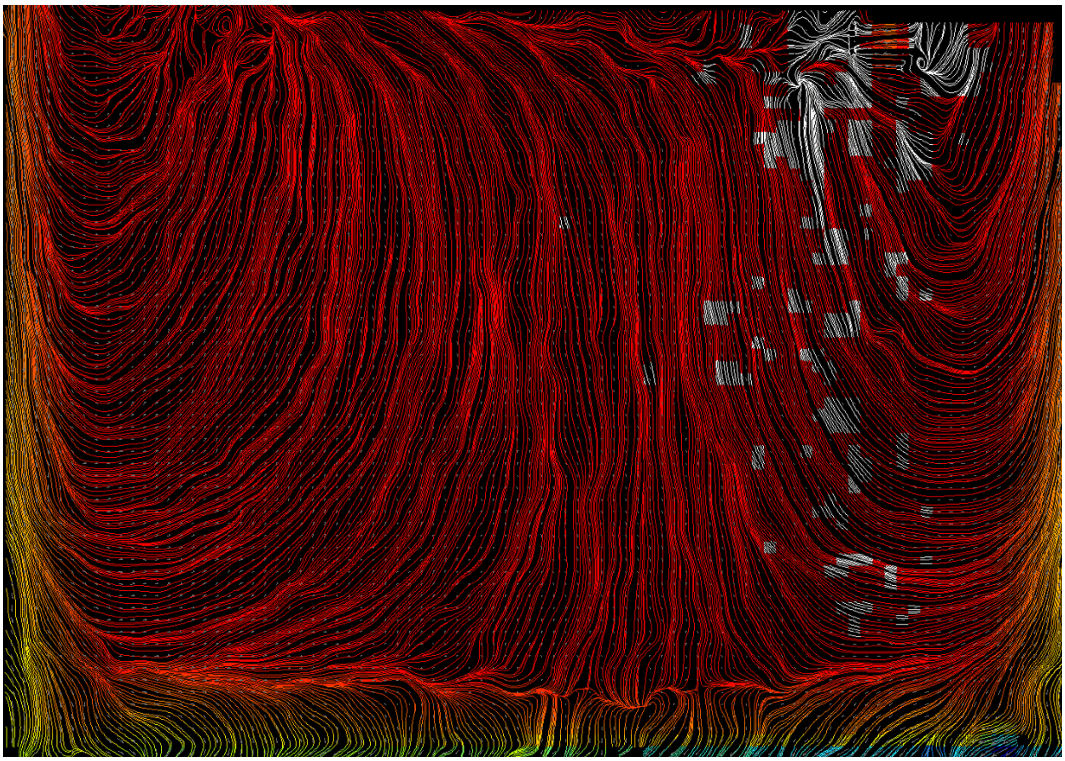

Figure 6.7: Vortex lines of TV1, showing large scale vortex motion and boundary layer saddle points.

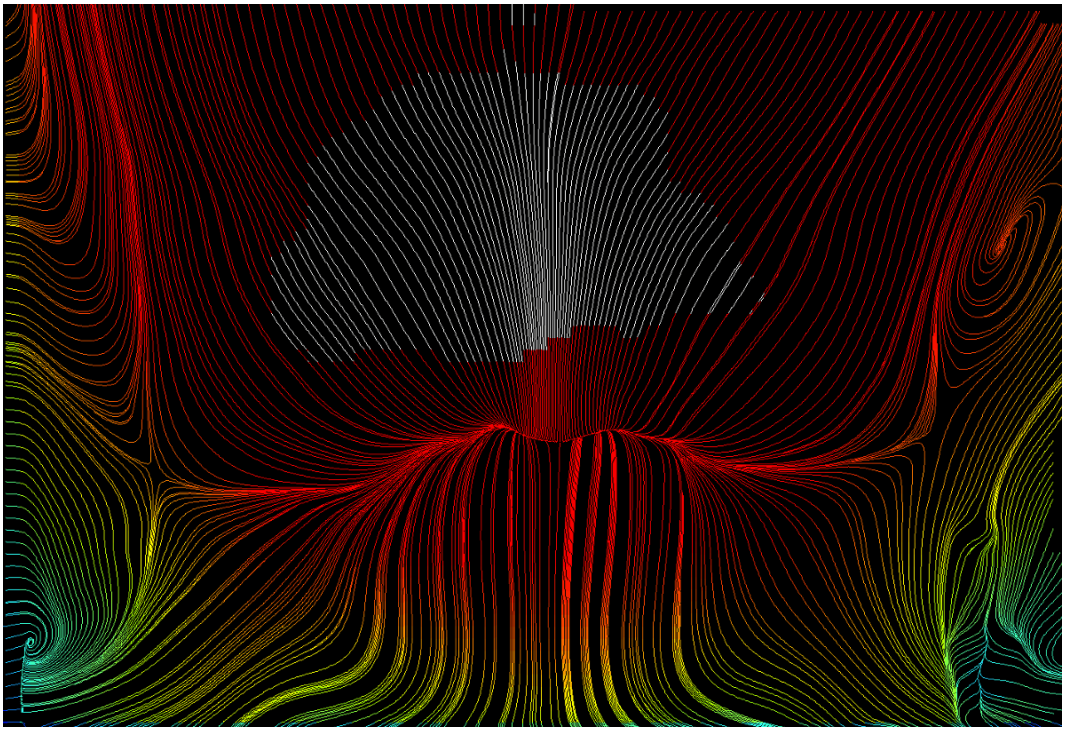

Figure 6.8: Vortex lines in TV10, downstream boundary of the measurement domain. No shock is visible in data, so convergence is exaggerated by the method.

bulges which are due to the spreading vortex structures that form in the wake of the secondary flow separations.

6.5 Summary

The following conclusions can be drawn from the spanwise planes:

1) Incoming boundary layer calculations are consistent across multiple planes and show consistent spanwise variability.

2) Substantial three-dimensionality visible upstream of the interaction as the curvature of the impinging shock (Fig. 6.3b) confirms the three-dimensionality measured by the streamwise horizontal planes.

3) The sidewall separation zone occurs at the intersection of two regions of vorticity of opposite sign. One originates from the corner interaction and the other is from the foot of the swept shock. A pocket of low momentum fluid occurs at the intersection and coincides with the stagnated oil flow region from Chapter IV.

4) Flow converges towards the centerline upstream of significant boundary layer thickening. Thus the centerline separation is seen to be the nodal type.

5) The streamwise vorticity component, ω_x measured through the interaction (TV3-TV9) indicate two visible secondary separations, one in the sidewall coincident with the oil flow separation region, and a second along the centerline where previously 'attached' flow was presumed due to the oil flow.

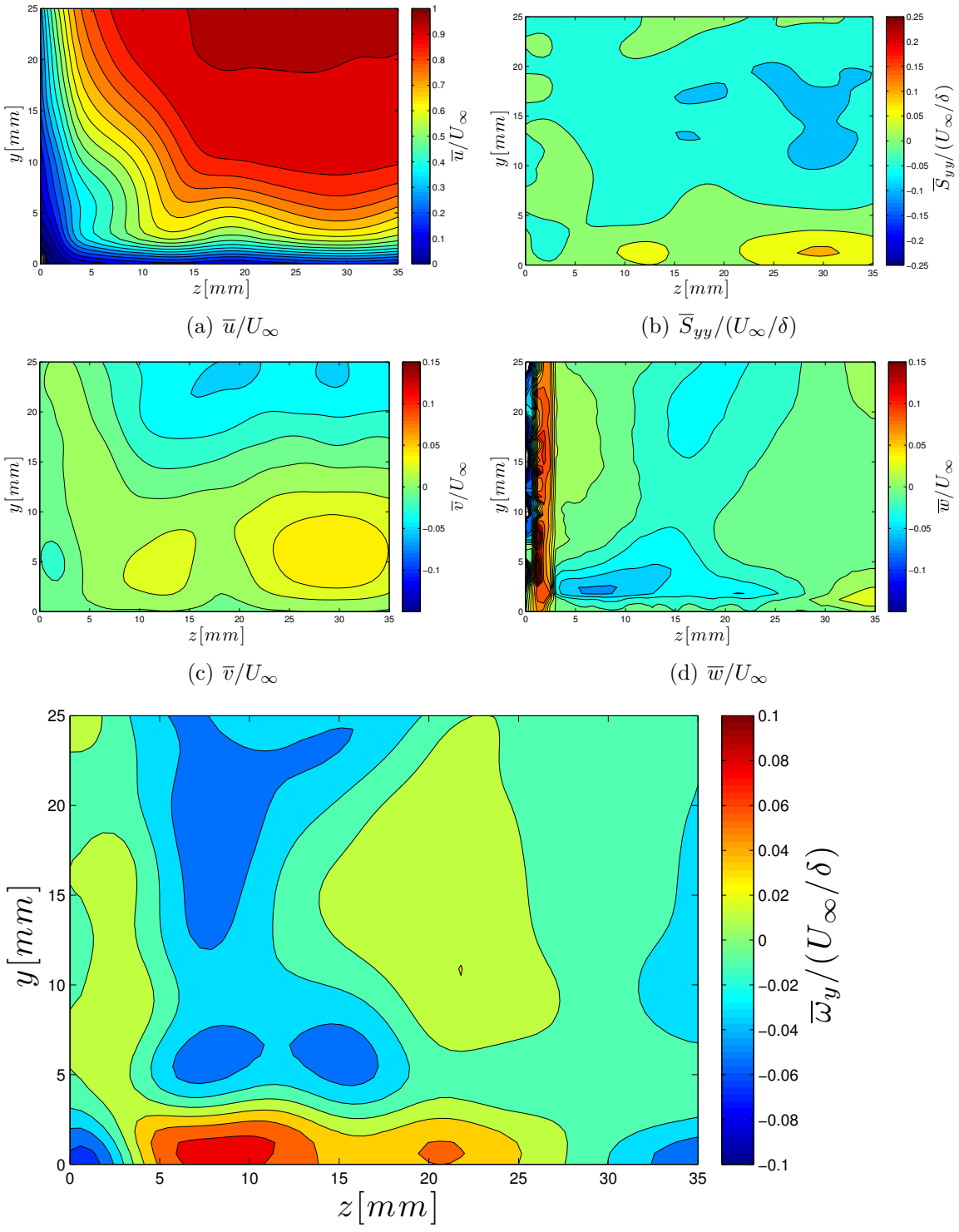

(a) $\overline{u}/U_\infty$

(b) $\overline{S}_{yy}/(U_\infty/\delta)$

(c) $\overline{v}/U_\infty$

(d) $\overline{w}/U_\infty$

(e) $\overline{\omega}_z/(U_\infty/\delta)$

Figure 6.9: Velocities: streamwise(a), vertical(b), transverse(c), computed normal strain(d) and streamwise vorticity(e) $x = 160\,mm$ (plane TV10.)

Taken together items 3-5 confirm the secondary flow separation hypothesis. Major conclusions are presented in the next section.

CHAPTER VII

Conclusions

A single three-dimensional inlet shockwave boundary layer interaction has been investigated with stereo PIV for the purpose of understanding the prominent interactive features, including aspects of oblique-impinging shocks, crossing shocks, SBLI, and corner flows. Significant extra care in the experimental design and data gathering phases makes this dataset uniquely amenable for CFD validation. Traditional two-dimensional understanding of SBLI does not yield a flow field that agrees with the measurements. The three-dimensional nature of the separation requires a careful examination of (and explanations for) anomalous behavior, such as the large scale vortical structures near the corners, and the change in separation type along the centerline when compared with previous '2D' studies. To better understand these interactions, a fully three dimensional picture is created using critical point theory to explain how features arising out of the side wall shock and corner flow combine and affect flow on the centerline. Critical point theory provides a versatile vocabulary for this and other three dimensional flows and the underlying mathematical framework. Examining how these features must join together while remaining topologically consistent (and thus physically realizable), a new 'secondary flow separation concept' is proposed to explain how to make 'connections' between critical points. That is,

SFSC explains how the interaction of lines on the surface (and hence vorticity in the flow field) can drive the development of new critical points.

(1) The secondary flow separation concept developed in this thesis provides a new methodology for SBLI analysis. It combines elements of three-dimensional flow separation critical point theory with physical intuition about vortex induced secondary flows to predict flow behavior downstream of 'primary separations'. PIV measurements of local velocity and vorticity validate that this method provides a useful grammar with which to describe three-dimensional SBLI, which is needed to supplant entrenched notions of two-dimensionality (Chapters II,VI)

(2) Large scale vortical structures (CPT foci) that appear in sidewall oil flow visualizations upstream of the inviscid shock locations which were previously unexplained are now understood using secondary flow separation concepts. The bifurcation of a local flow separation structure (topology preserving) into a global separation (topology altering) occurs at a corner location where the upstream influence line for a fin-plate SBLI intersects with the bottom wall. These features went previously unnoticed, however, because their three-dimensionality is not clear in span averaged density visualization methods such as Schlieren or shadowgraph diagnostics. (Chapters II,IV)

(3) Streamwise PIV measurements confirm the oil flow results. Both methods indicate significant three-dimensionality is present in all aspects of the interaction, and none of the interaction should be considered '2D'. (Chapters IV, V)

(4) Spanwise PIV measurements confirm that the side wall vortex structure is created by the interaction of induced downwash from the vortex structure under

the foot of the impinging shock in the side wall and the upper branch of the horseshoe vortex created by the corner separation. (Chapter VI)

(5) Generally, topological changes result when lines of separation meet in the flow field because of the interaction between the vortical structures that drive them. Thus, the position, strength, and trajectory of the sidewall separation structures potentially impacts the centerline separation topology. In this case, secondary flow originating with the corner horseshoe vortex penetrates all the way to the centerline prior to oblique shock impingement. For inlets with sufficiently narrow span, such as the tunnel under investigation, secondary flows from the corners interact with flow along both the bottom wall and prevent primary separation from occurring at the centerline. (Chapters IV,V,VI)

The results cumulatively demonstrate that the effects secondary flows induced by shock boundary layer interactions can be explained through the vorticity field and how the nature of the vorticity field is determined through the distribution of critical points. Lines of separation which can be identified in the oil, act as markers of the impact of these vortices as they migrate through the flow. In such cases, the secondary flow separation concept successfully describes the topological shift that occurs when two lines of separation meet through the interaction of the vorticity which drives them. In this regard, it is a considerable improvement over standard two-dimensional characterizations of SBLI induced separation. It should be noted that slicing a primary or a secondary flow separation along it's vertical plane of symmetry recreates an indistinguishable picture of a traditional two-dimensional flow separation. This flow character easily accounts for the lack of consensus regarding previous measurements of 2D flow separations as these two types could not previously

be contrasted.

Direction for future work

The interaction of shock waves and boundary layers is still often conceptually decoupled into boundary layers in adverse pressure gradients and shock waves which respond to geometry changes. Current analysis avoids discussion of the structure and nature of the coupling between the entropy generated in the shock and the entropy generated in the boundary layer. Thermodynamic principles regarding the entropy generated through irreversibility brought on by viscous interaction and finite-time processes is still underdeveloped.

The link between vortex structures and local topological structure was shown for one type of flow separation, however a generalizable formula for such interactions is left outstanding.

Simultaneous measurements of the instantaneous density and velocity fields can be achieved by combining the present SPIV technique with Rayleigh scattering. Such measurements would enable computation of the Favre averaged mean and fluctuation statistics, and therefore more directly account for the effects of compressibility. Coupling these measurements with static wall-pressure measurements would furthermore enable good approximations of the thermodynamic state variables and transport quantities throughout the SBLI. In turn, these will enable more accurate accounts of the dissipation rate, for example, and can be used to more rigorously assess the validity of the popular Boussinesq hypothesis as well as the improvements provided by non-equilibrium RANS models presently under development.

Ongoing work on robust methods for PIV uncertainty was not documented here. In particular, synthetic PIV image generation needs to expand into the physical

realm. Providing fool-proof methods for installing physical-synthetic PIV images to be imaged would provide a simple cost-effective means of estimating uncertainty from the imaging and velocimetry portion of PIV. Methods associated with particle seeding, delivery, and flow field following may also offer means of improving data collection. In particular, fluorescent particles enable camera filters to remove or diminish laser reflections at the wall which obscure data in the present measurements. Lastly, emergent work by Mitchell et al. (2011) on uncertainty of PIV tracer particles in shock waves conflicts with previous 'good agreement' between PIV and LDV in shock regions and requires further assessment.

Increasing the dynamic range of PIV images is also a fruitful avenue, using a triple pulsed laser and three cameras (or a triple shifted camera mask) could dramatically increase the dynamic range of the PIV technique. In a personal communication, Ron Adrian, one of the principle developers of PIV, laments that most current applications of PIV "are like using a two digit voltmeter." Methods to increase the dynamic range of measurements in these devices are necessary to simultaneously resolve the large field of view spatial gradients with the small scale turbulent fluctuations.

Uncovering the three-dimensional nature of SBLI opens a number of questions regarding the optimal control of such flows. Considering severe negative impact the change in behavior between 2D and 3D flows creates, methods to mitigate such three-dimensionality should be the focus of control efforts. A study of three-dimensionality in the compression ramp and in particular the normal shock interaction should be considered vital. Oil flow is an indispensable first step to determine regions of interest and the scale of the three-dimensionality, considering the misleading two-dimensionality suggested by Schlieren.

The control of SBLI did not receive attention in this thesis; however, control

strategies can be considered in terms of the secondary flows they produce, and the effects such secondary flow has on the natural structure of SBLI. The primary strategies, bleed effects and passive ramp control already help to reduce the amount of three-dimensionality that is possible in the incoming shock fronts by replacing primary separations with local secondary flow separations helping to return the flow to a more two-dimensional character. In practice this advice is always applicable. Large 'Primary' separations should be avoided because they invariably lead to secondary separations. Thus small primary separations which quickly terminate in secondary separations should be favored. Furthermore, given the susceptibility of a 90 degree to primary separation, other manufacturing methods should be considered to reduce such junctions. Absent that, this thesis has presented the SFSC to help better understand and predict these corner separations.

APPENDICES

APPENDIX A

Test section dimensions

The critical dimensions necessary to model or reproduce the present experiment are offered in this section. Figure A.1 shows a streamwise-oriented cross-sectional view of the test section. The leading edge of the wedge, marks the $x = 0$ location, 61mm upstream of the Strut Leading Edge from Lapsa (2009), and produces an oblique shock wave which propagates at angle $\beta = 25.8$. The inviscid extension of the shock wave impinges on the opposite boundary at $x = 120mm$.The bulk flow moves from left to right and is deflected by an angle θ via a wedge mounted 9.7mm from the top boundary of the test section by the pictured strut. The wedge projects a frontal dimension of 9.3-mm which is optimized to separate the expansion fan off of the corner with the wind tunnel starting limits. This wedge design also provides 2° of relief, rather than a flat top to account for the presence of the strut. This helps to avoid separation above the wedge by developing a favorable pressure gradient. The downstream face is formed at an 8.5-deg angle.

Figure A.2 gives the corresponding dimensions in the spanwise-oriented cross-section, showing in particular the full-spanwise extent of the shock-generating wedge. As previously noted, the test section has a 57.2 × 69.8-mm (2.25 × 2.75-in) cross-section.

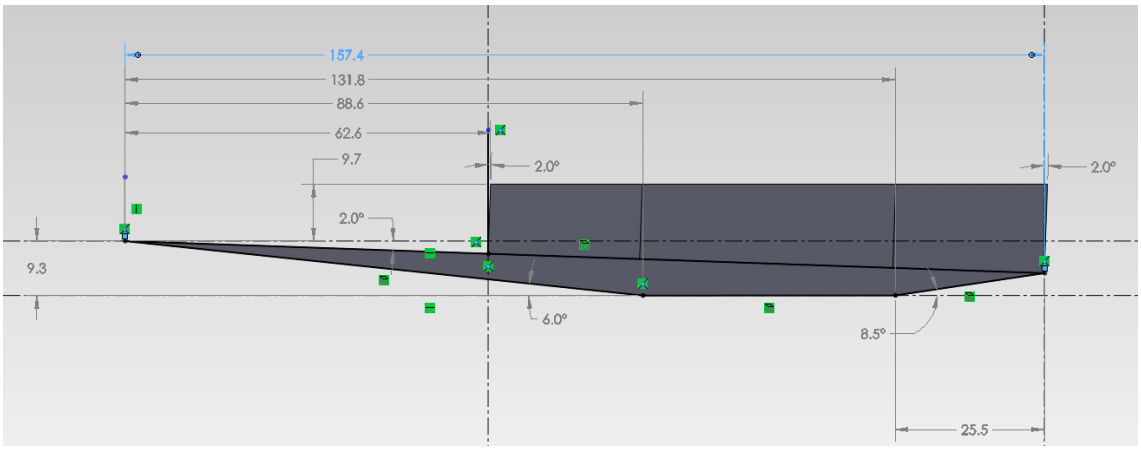

Figure A.1: Wedge and strut geometry dimensions from a side view.

θ (deg)	β (deg)	x_{LE} (mm)	$x_{InvisImpinge}$ (mm)
6.0	25.8	0	120

Table A.1: Defining dimensions for the geometry used in the present study, corresponding to Fig. A.1.

The geometry of the converging-diverging nozzle is also potentially critical for computational simulation of the present geometry. An under-sampled array of 163 defining coordinates are reprinted in Table A.2 from Lapsa (2009). In this, the $x = 0$ location corresponds to the nozzle throat, which is located 538.1-mm upstream of the strut leading edge, x_{SLE}, from Fig. **??**. The throat has height 0.742-in, giving a total expansion ratio of $A/A^* = 3.706$. The supersonic nozzle contour is determined using the NOZCS code which considers the growth of a turbulent boundary layer via the displacement thickness and compensates for this extra blockage via slight overexpansion.

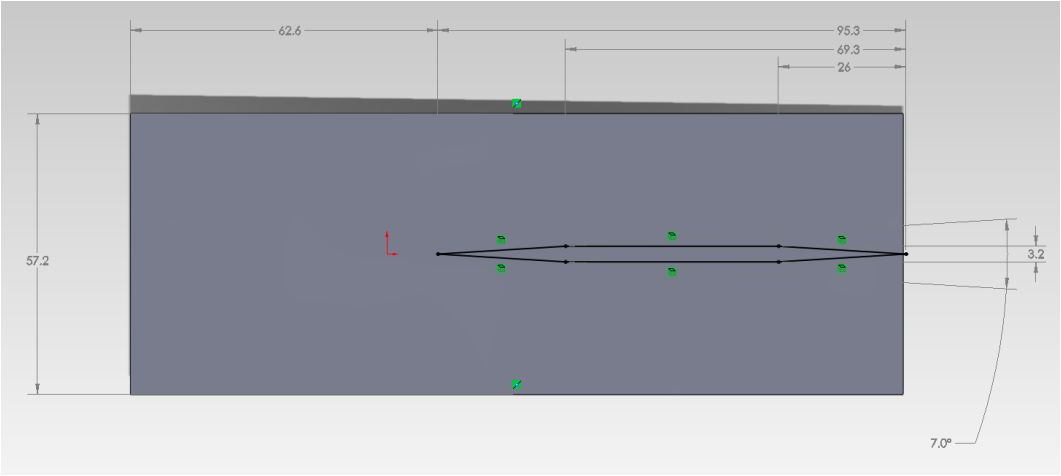

Figure A.2: Wedge and strut geometry dimensions from a top view.

Nozzle Coordinates ($M = 2.75$)									
x (in)	y (in)	x (in)	y (in)	x (in)	y (in)	x (in)	y (in)	x (in)	y (in)
-12.215	10.000	-1.164	0.977	2.584	1.661	5.995	2.407	9.406	2.709
-11.664	9.992	-1.003	0.915	2.684	1.692	6.095	2.421	9.506	2.713
-11.343	9.968	-0.843	0.863	2.784	1.723	6.196	2.435	9.607	2.717
-11.022	9.925	-0.682	0.821	2.885	1.753	6.296	2.448	9.707	2.721
-10.701	9.865	-0.522	0.788	2.985	1.782	6.396	2.461	9.807	2.724
-10.380	9.787	-0.361	0.764	3.085	1.810	6.497	2.474	9.908	2.727
-10.059	9.689	-0.201	0.749	3.186	1.838	6.597	2.486	10.008	2.730
-9.738	9.571	-0.040	0.742	3.286	1.866	6.697	2.498	10.108	2.733
-9.417	9.432	0.000	0.742	3.386	1.892	6.798	2.510	10.209	2.735
-9.095	9.269	0.075	0.745	3.487	1.918	6.898	2.521	10.309	2.738
-8.774	9.081	0.176	0.758	3.587	1.944	6.998	2.532	10.409	2.740
-8.453	8.865	0.276	0.779	3.687	1.969	7.098	2.543	10.510	2.742
-8.132	8.616	0.376	0.810	3.788	1.993	7.199	2.553	10.610	2.744
-7.811	8.330	0.477	0.848	3.888	2.017	7.299	2.563	10.710	2.745
-7.490	7.997	0.577	0.892	3.988	2.040	7.399	2.573	10.811	2.746
-7.139	7.583	0.677	0.935	4.089	2.063	7.500	2.582	10.911	2.747
-6.732	7.089	0.778	0.978	4.189	2.085	7.600	2.591	11.011	2.748
-6.324	6.612	0.878	1.021	4.289	2.107	7.700	2.600	11.112	2.749
-5.916	6.126	0.978	1.063	4.390	2.128	7.801	2.608	11.212	2.749
-5.509	5.640	1.079	1.106	4.490	2.149	7.901	2.617	11.312	2.750
-5.101	5.154	1.179	1.148	4.590	2.169	8.001	2.625	11.413	2.750
-4.693	4.668	1.279	1.189	4.691	2.189	8.102	2.633	11.513	2.750
-4.286	4.182	1.380	1.230	4.791	2.208	8.202	2.640	11.613	2.750
-3.878	3.697	1.480	1.269	4.891	2.227	8.302	2.647	11.714	2.750
-3.470	3.211	1.580	1.309	4.992	2.246	8.403	2.654	11.814	2.750
-3.063	2.725	1.681	1.347	5.092	2.264	8.503	2.661	11.914	2.750
-2.655	2.239	1.781	1.385	5.192	2.281	8.603	2.667	12.015	2.750
-2.288	1.801	1.881	1.422	5.293	2.298	8.704	2.673		
-2.127	1.627	1.982	1.459	5.393	2.315	8.804	2.679		
-1.967	1.477	2.082	1.494	5.493	2.332	8.904	2.685		
-1.806	1.347	2.182	1.529	5.594	2.347	9.005	2.690		
-1.646	1.234	2.283	1.563	5.694	2.363	9.105	2.695		
-1.485	1.136	2.383	1.596	5.794	2.378	9.205	2.700		
-1.324	1.050	2.483	1.629	5.895	2.393	9.306	2.704		

Table A.2: Sampled coordinates for $M = 2.75$ nozzle.

APPENDIX B

Streamwise Vertical Data

This section presents data from the streamwise vertical planes which were not presented in the main body of the thesis. The data is presented in a consistent format first in a perspective view of all three planes oriented along a consistent axis, followed by individual profiles from each plane. Table B.1 presents the order of the quantities considered. The individual profiles displayed from the the contour map are presented along vertical planes cut by the transverse views in Appendix D and labeled 3 to 9. Profile '0' is closest profile possible to an 'input' location for each view.

U Velocity	u_x
V Velocity	u_y
W Velocity	u_z
Spanwise Vorticity	ω_z
X Normal Strain	S_{xx}
Y Normal Strain	S_{yy}
X-Y Shear Strain	S_{xy}
X Reynolds Stress	u'^2
Y Reynolds Stress	v'^2
Z Reynolds Stress	w'^2
Turbulence Kinetic Energy	$\sqrt{\overline{k}}$
XY Reynolds Stress	$u\prime v\prime$
XZ Reynolds Stress	$u\prime w\prime$
YZ Reynolds Stress	$v\prime w\prime$

Table B.1: Presented PIV velocity data and derived quantities.

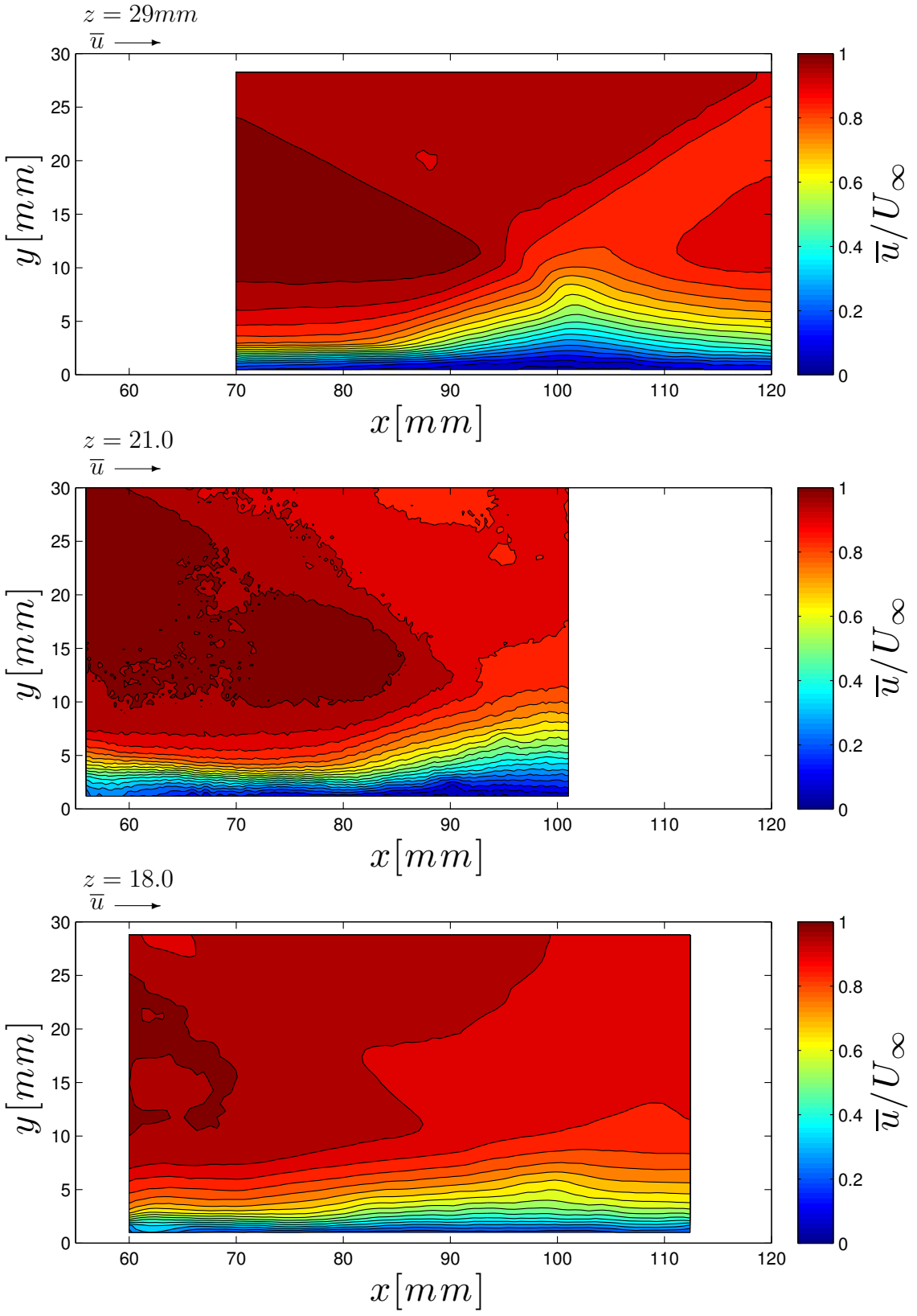

Figure B.1: Visualizations of the velocity component $\overline{u}$ for each of the three vertical planes oriented in the streamwise direction.

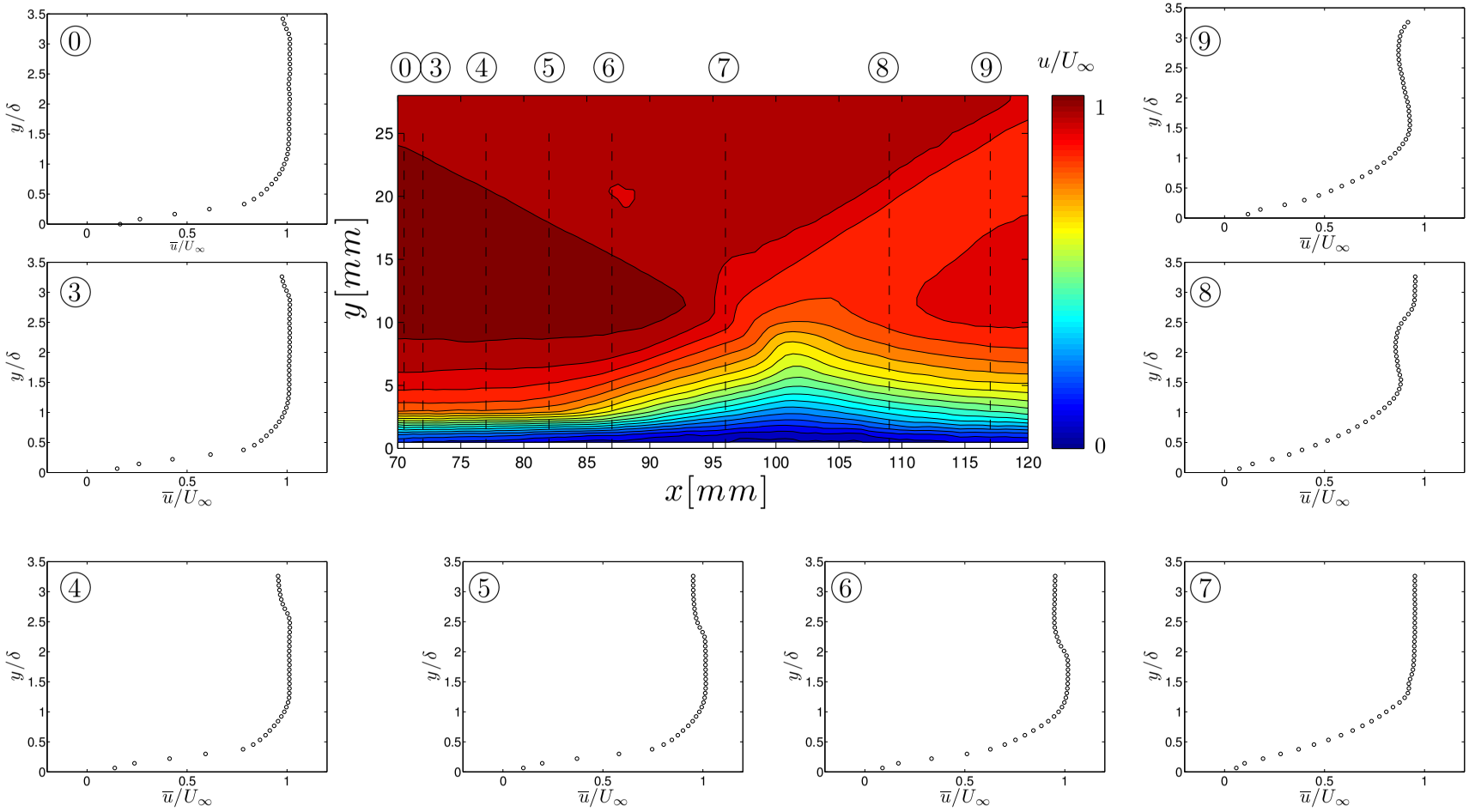

Figure B.2: Evolution of $\overline{u}$ through the z=29mm SBLI region for a flow deflection angle of $\theta = 6$ deg. Sampling numbers correspond to transverse plane sampling locations, location '0' indicating the region where U_∞ is calculated. At top, colors show the $\overline{u}$ field throughout each sampling plane, and also indicate their relative locations.

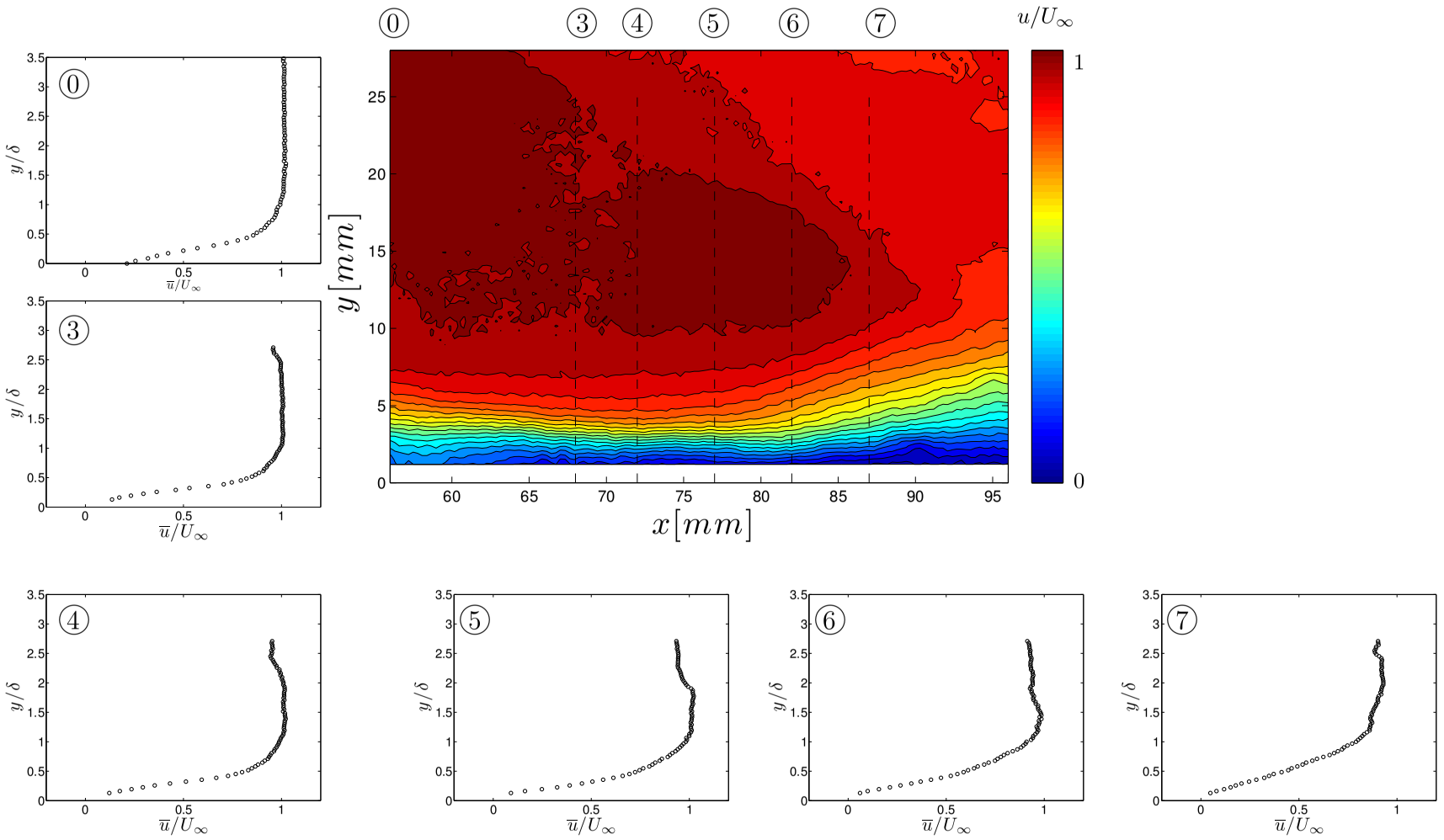

Figure B.3: Evolution of $\overline{u}$ through the z=21mm SBLI region for a flow deflection angle of $\theta = 6$ deg. Sampling numbers correspond to transverse plane sampling locations, location '0' indicating the region where U_∞ was calculated. At top, colors show the $\overline{u}$ field throughout each sampling plane, and also indicate their relative locations.

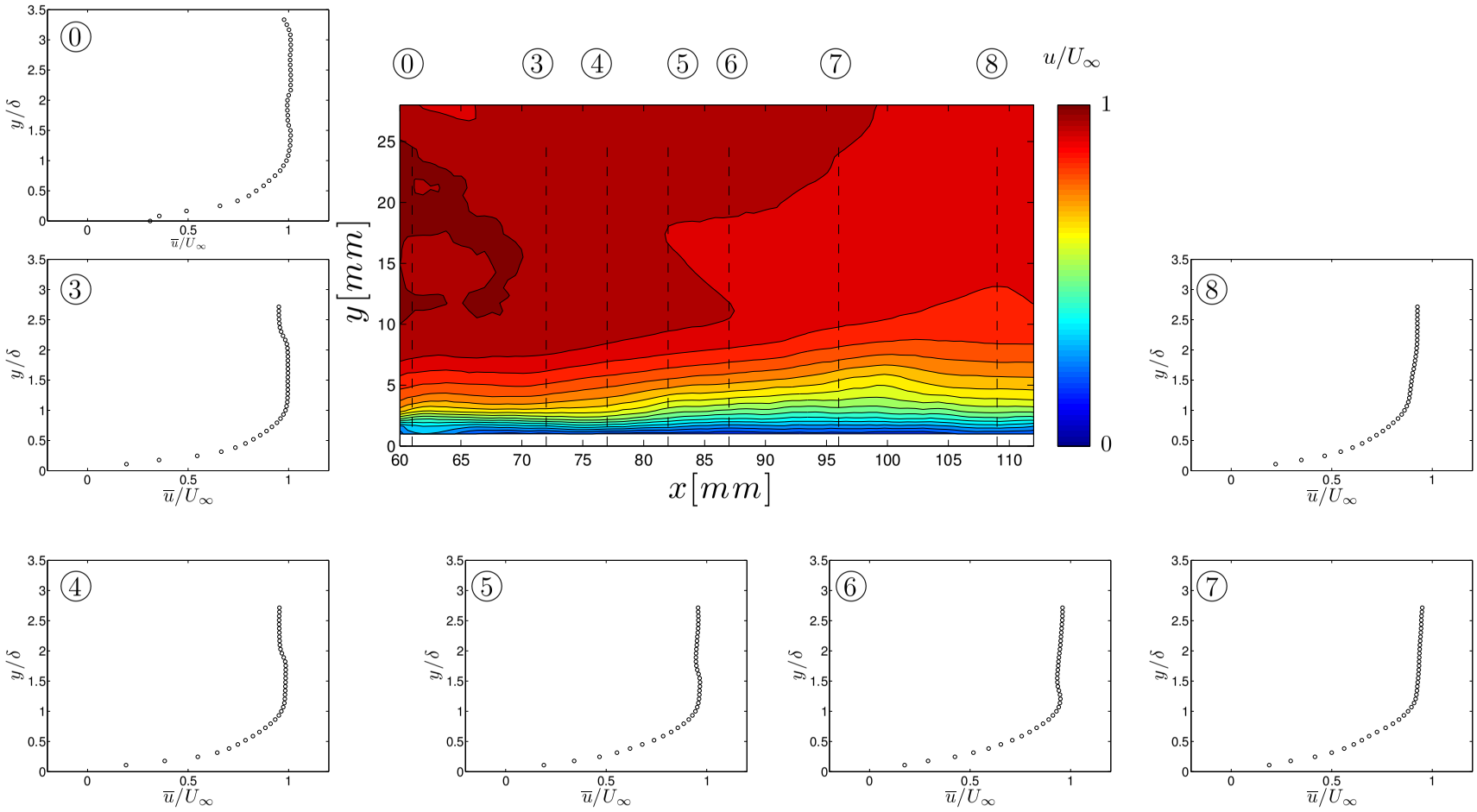

Figure B.4: Evolution of $\overline{u}$ through the z=18mm SBLI region for a flow deflection angle of $\theta = 6$ deg. Sampling numbers correspond to transverse plane sampling locations, location '0' indicating the region where U_∞ was calculated. At top, colors show the $\overline{u}$ field throughout each sampling plane, and also indicate their relative locations.

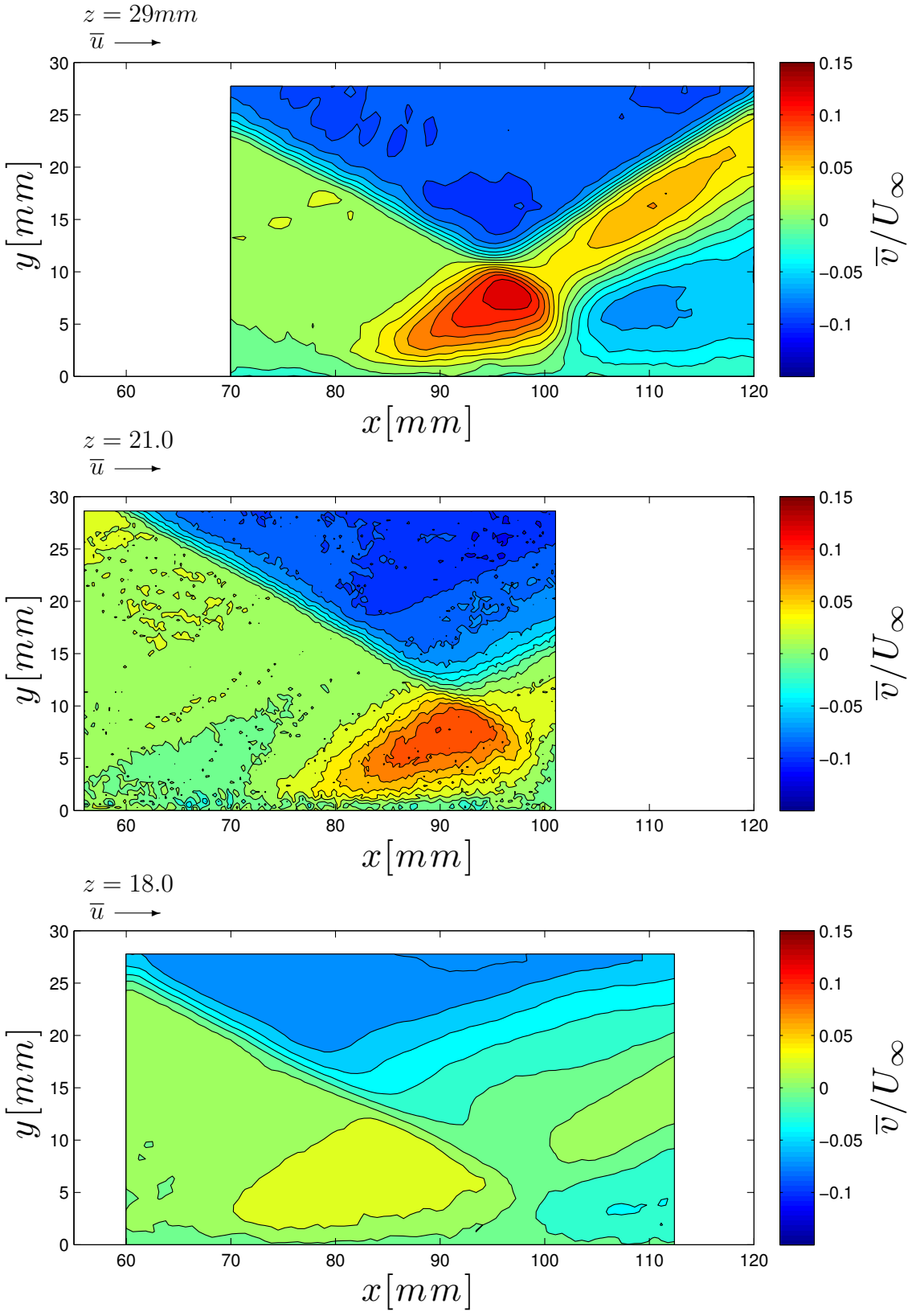

Figure B.5: Visualizations of the streamwise velocity component $\overline{v}$ for each of the three vertical planes oriented in the streamwise direction.

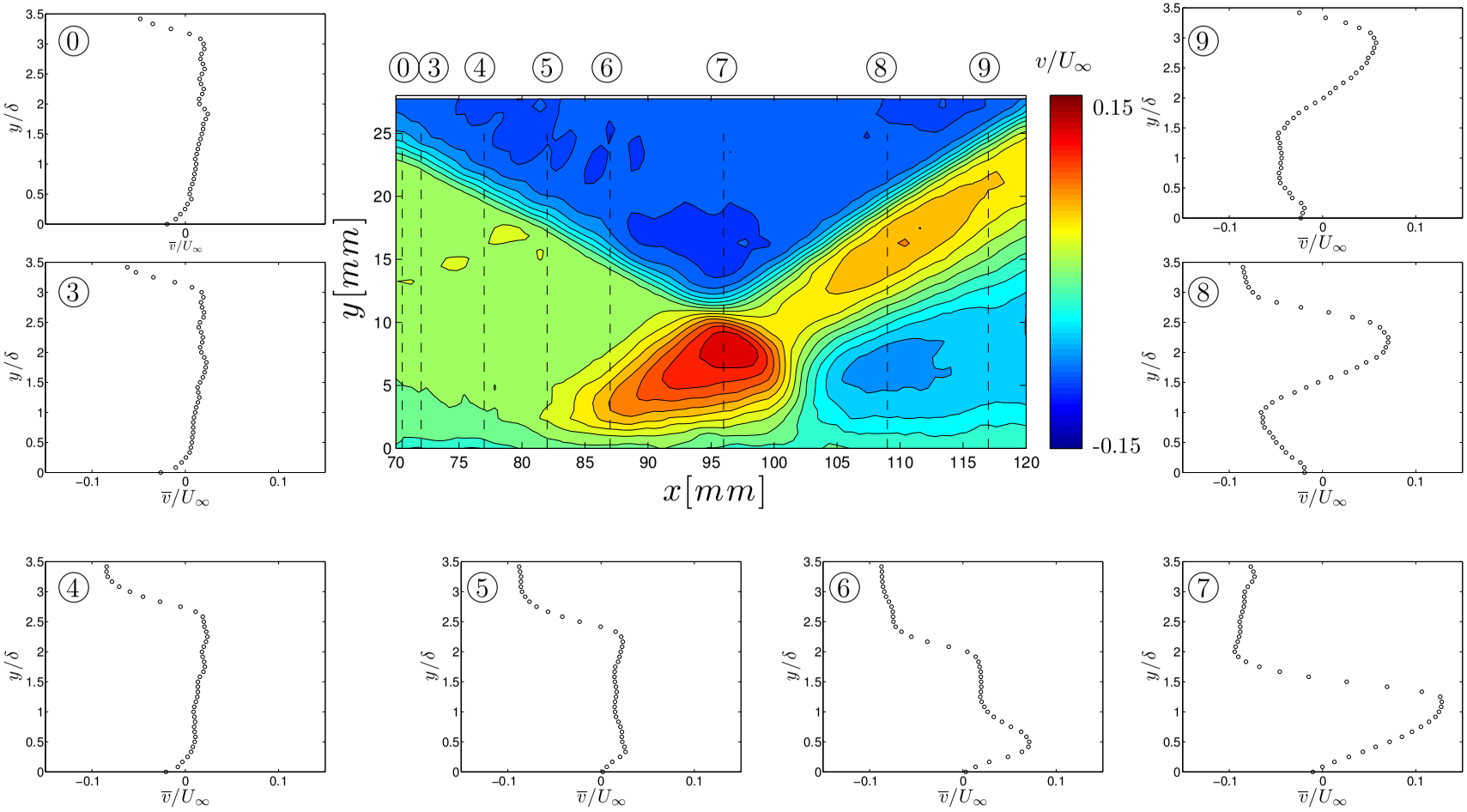

Figure B.6: Evolution of $\overline{v}$ through the z=29mm SBLI region for a flow deflection angle of $\theta = 6$ deg. Sampling numbers correspond to transverse plane sampling locations, location '0' indicating the region where U_∞ is calculated. At top, colors show the $\overline{v}$ field throughout each sampling plane, and also indicate their relative locations.

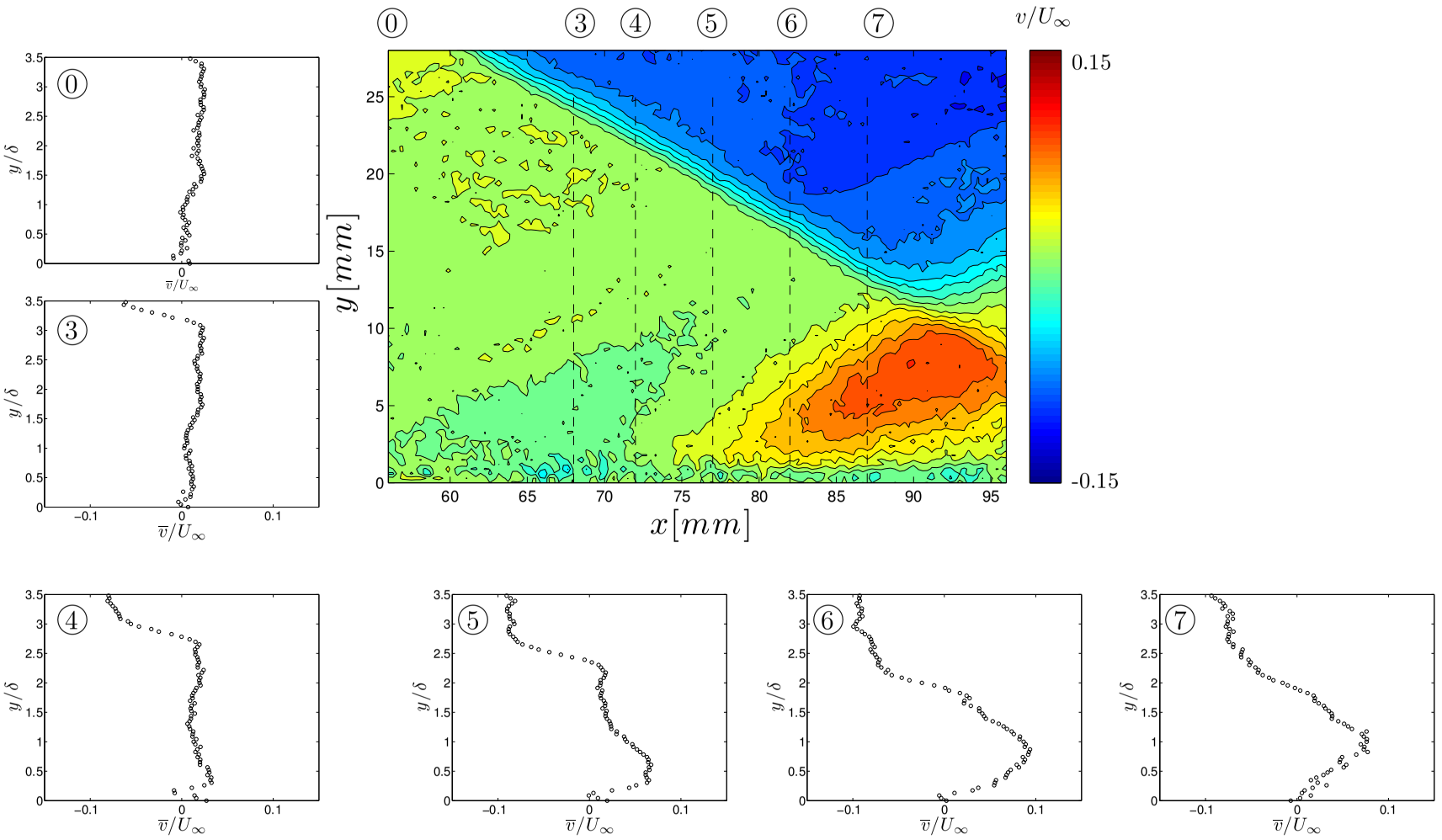

Figure B.7: Evolution of $\overline{v}$ through the z=21mm SBLI region for a flow deflection angle of $\theta = 6$ deg. Sampling numbers correspond to transverse plane sampling locations, location '0' indicating the region where U_∞ was calculated. At top, colors show the $\overline{v}$ field throughout each sampling plane, and also indicate their relative locations.

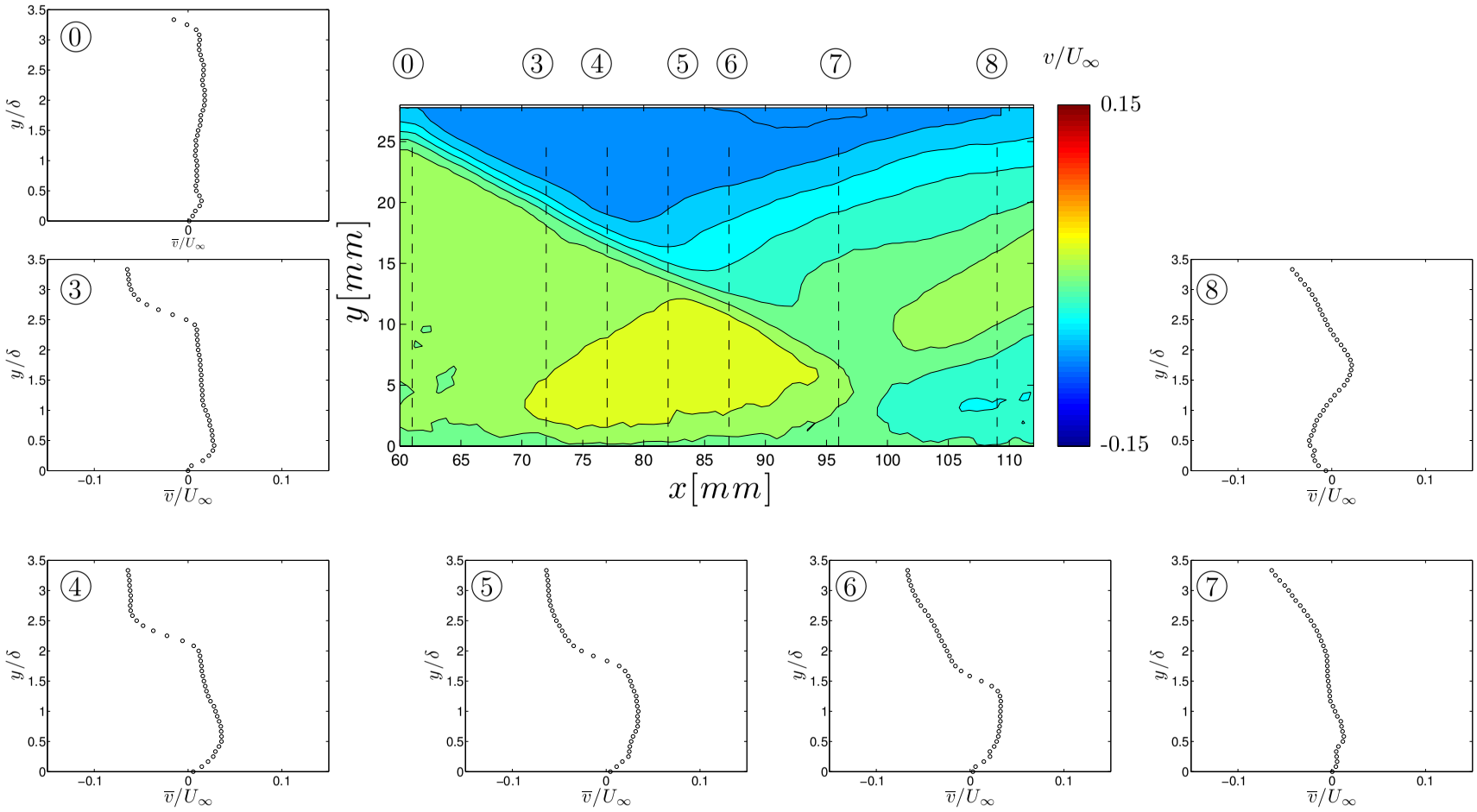

Figure B.8: Evolution of $\overline{v}$ through the z=18mm SBLI region for a flow deflection angle of $\theta = 6$ deg. Sampling numbers correspond to transverse plane sampling locations, location '0' indicating the region where U_∞ was calculated. At top, colors show the $\overline{v}$ field throughout each sampling plane, and also indicate their relative locations.

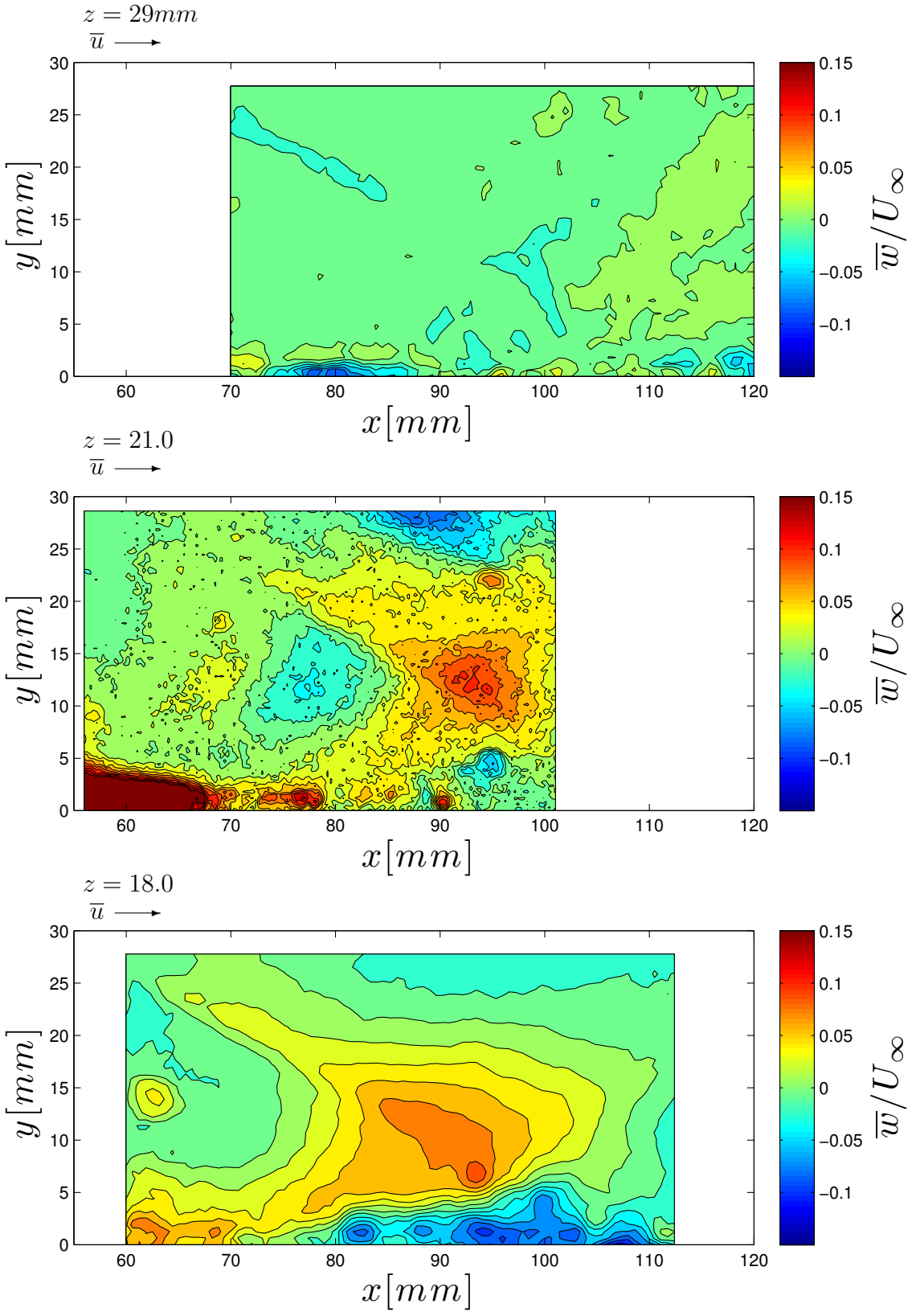

Figure B.9: Visualizations of the velocity component $\overline{w}$ for each of the three vertical planes oriented in the streamwise direction.

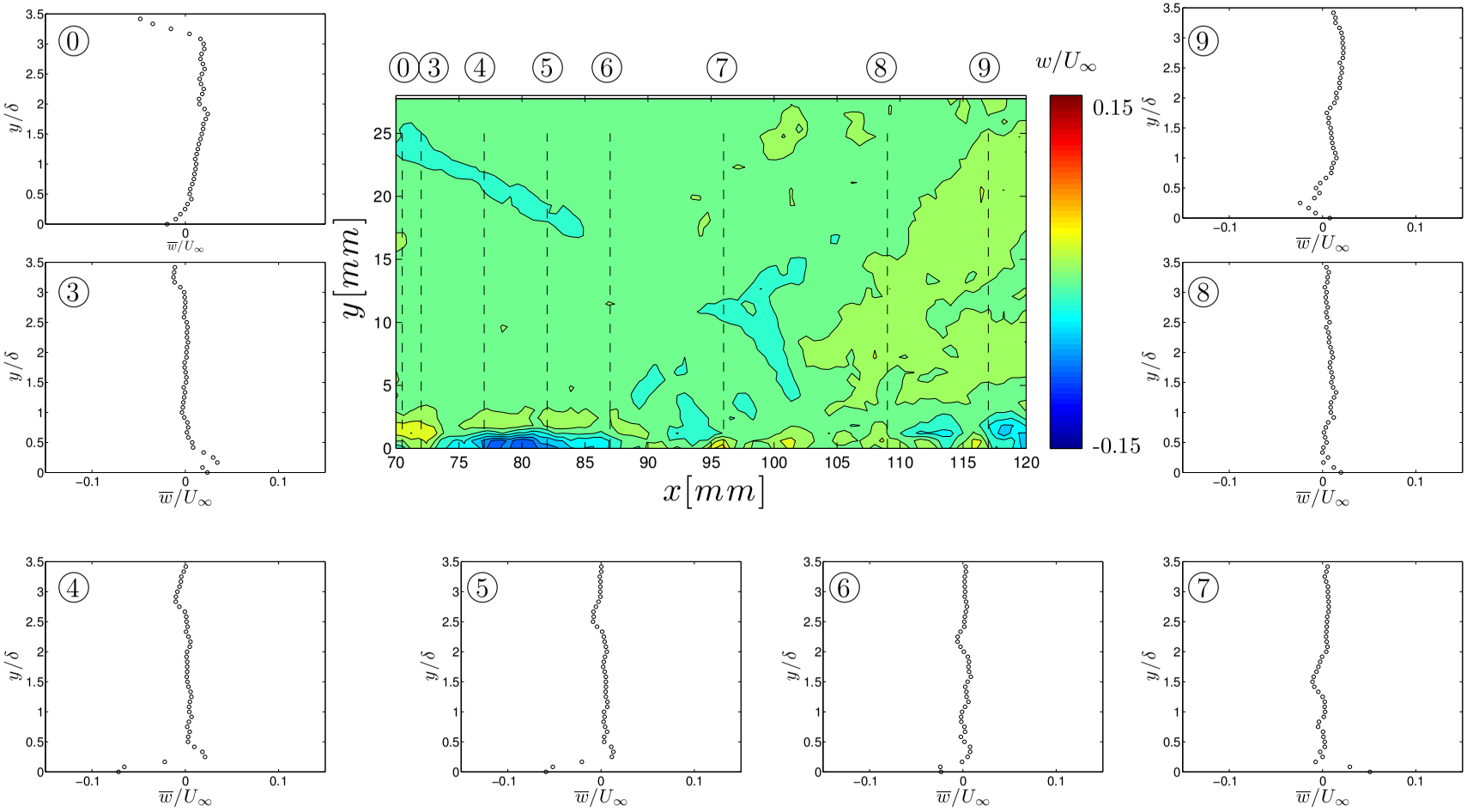

Figure B.10: Evolution of $\overline{w}$ through the z=29mm SBLI region for a flow deflection angle of $\theta = 6$ deg. Sampling numbers correspond to transverse plane sampling locations, location '0' indicating the region where U_∞ was calculated. At top, colors show the $\overline{w}$ field throughout each sampling plane, and also indicate their relative locations.

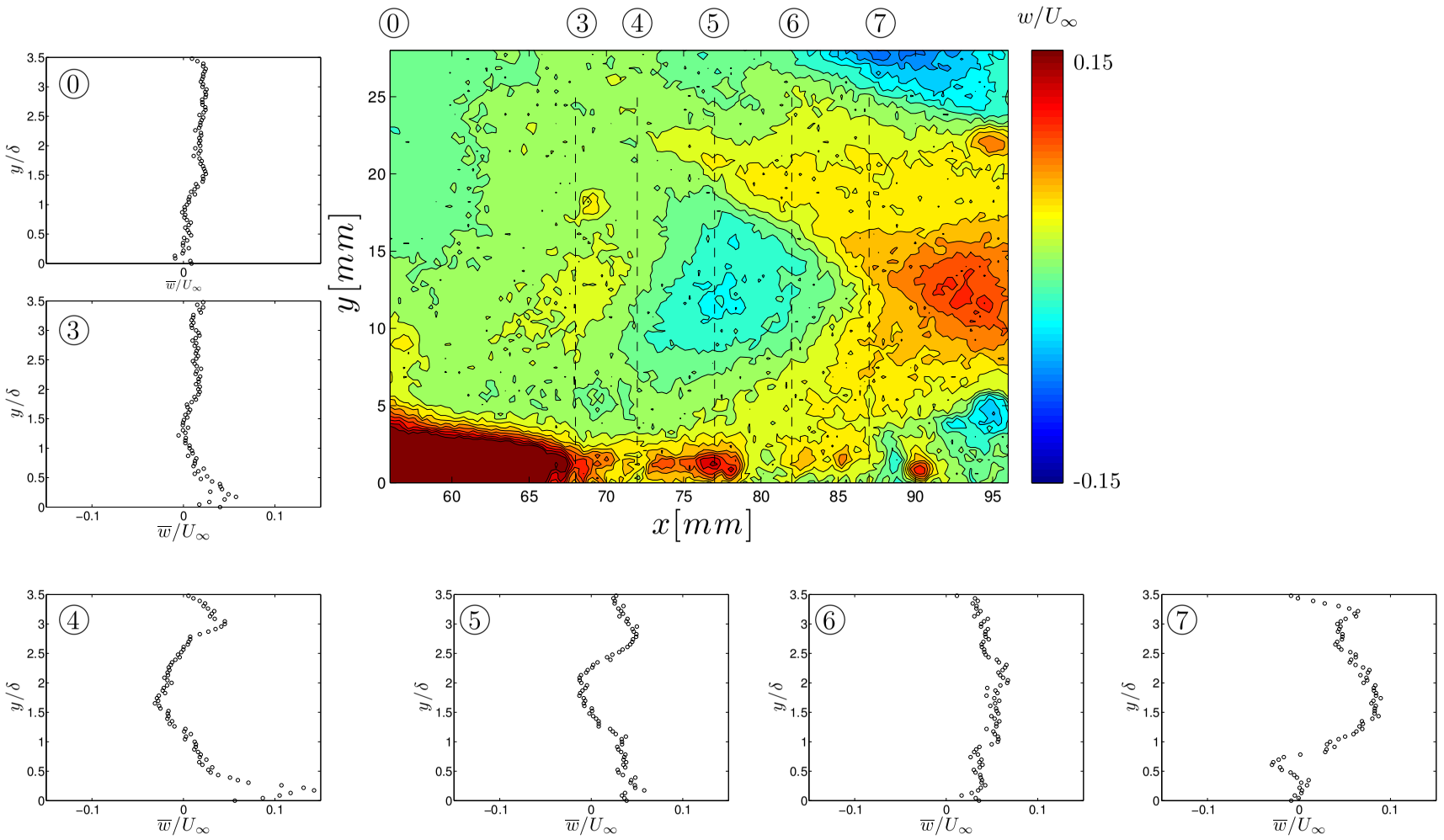

Figure B.11: Evolution of $\overline{w}$ through the z=21mm SBLI region for a flow deflection angle of $\theta = 6$ deg. Sampling numbers correspond to transverse plane sampling locations, location '0' indicating the region where U_∞ was calculated. At top, colors show the $\overline{w}$ field throughout each sampling plane, and also indicate their relative locations.

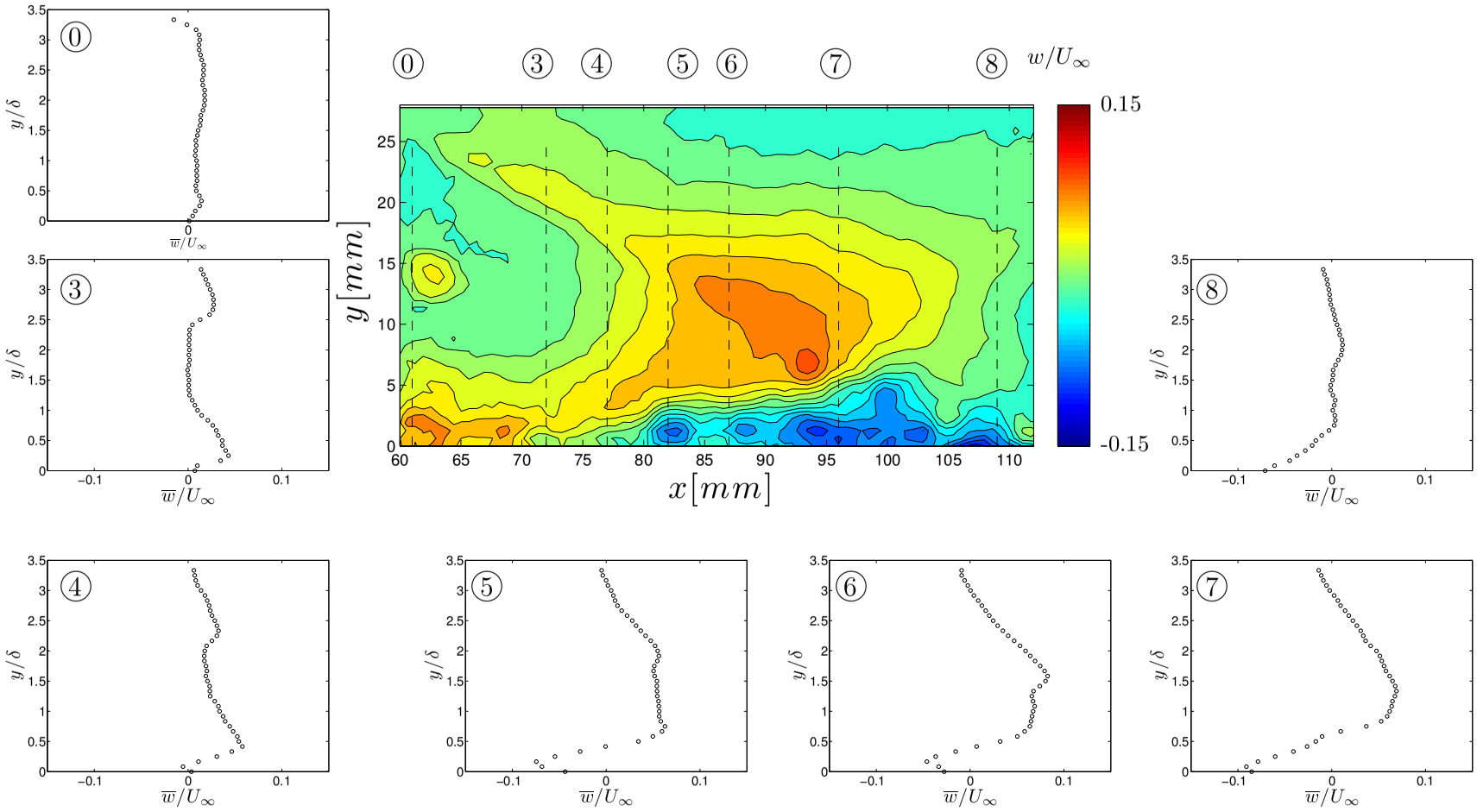

Figure B.12: Evolution of $\overline{w}$ through the z=18mm SBLI region for a flow deflection angle of $\theta = 6$ deg. Sampling numbers correspond to transverse plane sampling locations, location '0' indicating the region where U_∞ was calculated. At top, colors show the $\overline{w}$ field throughout each sampling plane, and also indicate their relative locations.

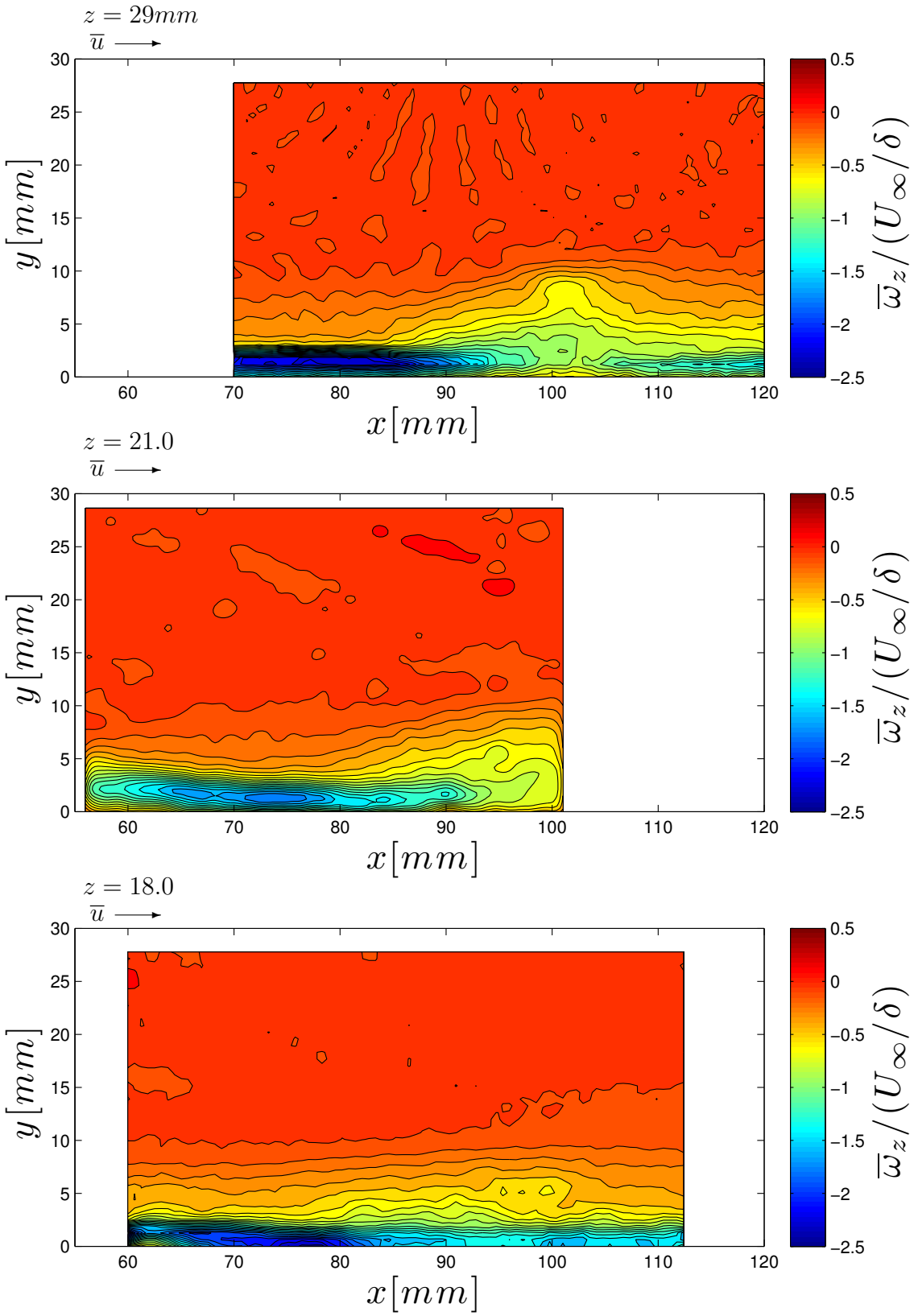

Figure B.13: Vorticity, $\overline{\omega}_z/(U_\infty/\delta)$ for each of the three vertical planes oriented in the streamwise direction.

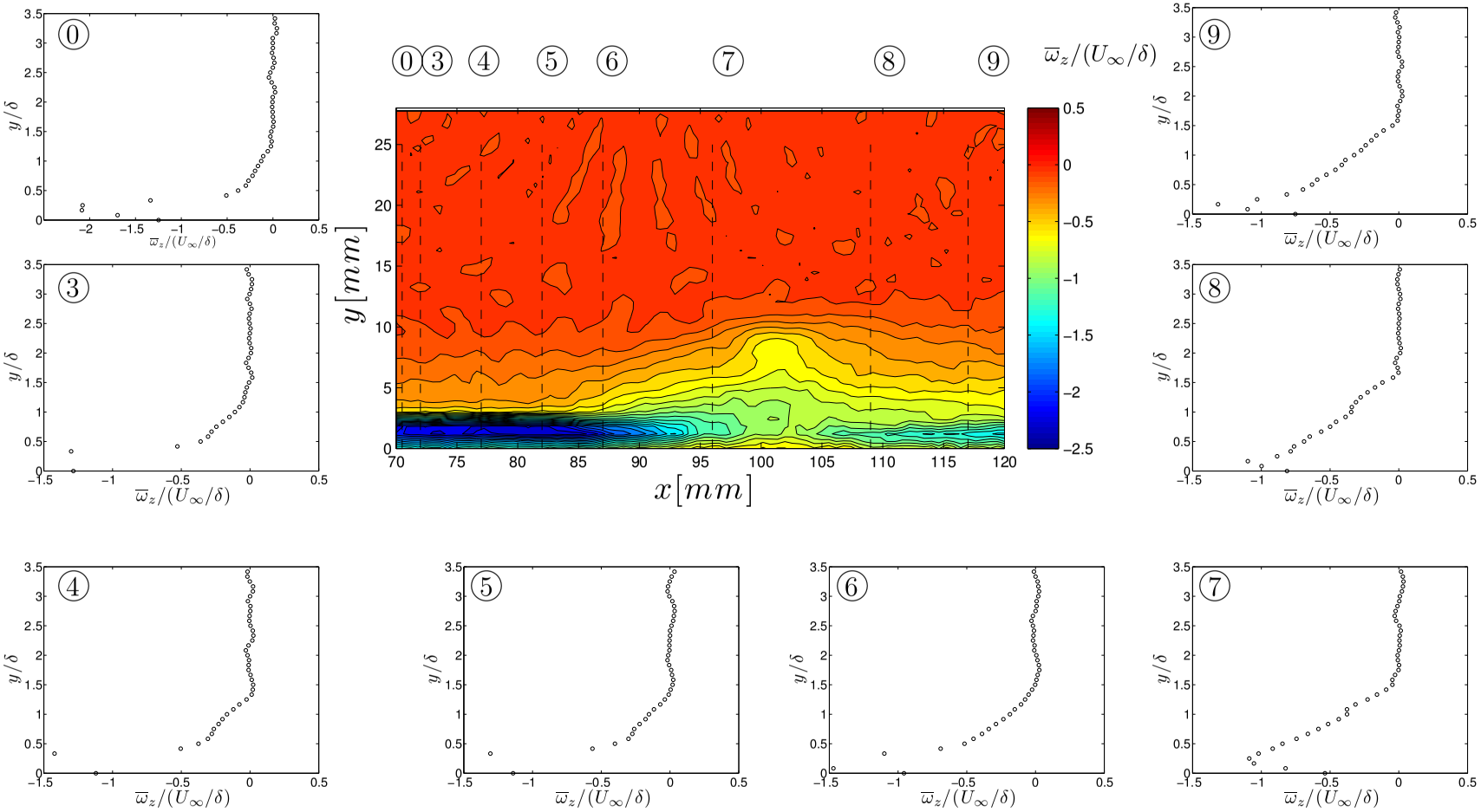

Figure B.14: Evolution of $\overline{\omega}_z/(U_\infty/\delta)$ through the z=29mm SBLI region for a flow deflection angle of $\theta = 6$ deg. Sampling numbers correspond to transverse plane sampling locations, location '0' indicating the region where U_∞ was sampled. At top, colors show the $\overline{\omega}_z/(U_\infty/\delta)$ field throughout each sampling plane, and also indicate their relative locations.

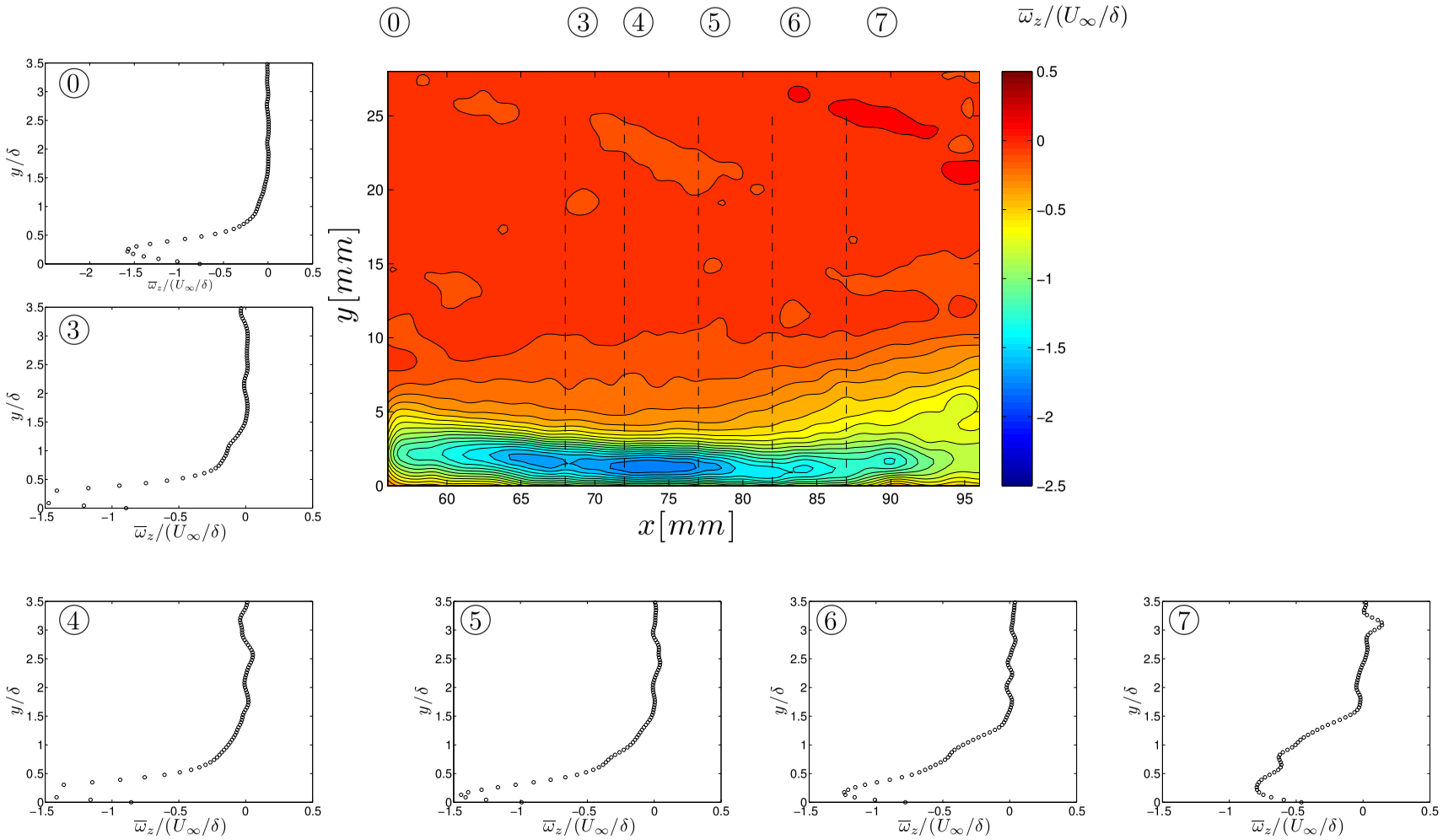

Figure B.15: Evolution of $\overline{\omega}_z/(U_\infty/\delta)$through the z=21mm SBLI region for a flow deflection angle of $\theta = 6$ deg. Sampling numbers correspond to transverse plane sampling locations, location '0' indicating the region where U_∞ was sampled. At top, colors show the $\overline{\omega}_z/(U_\infty/\delta)$ field throughout each sampling plane, and also indicate their relative locations.

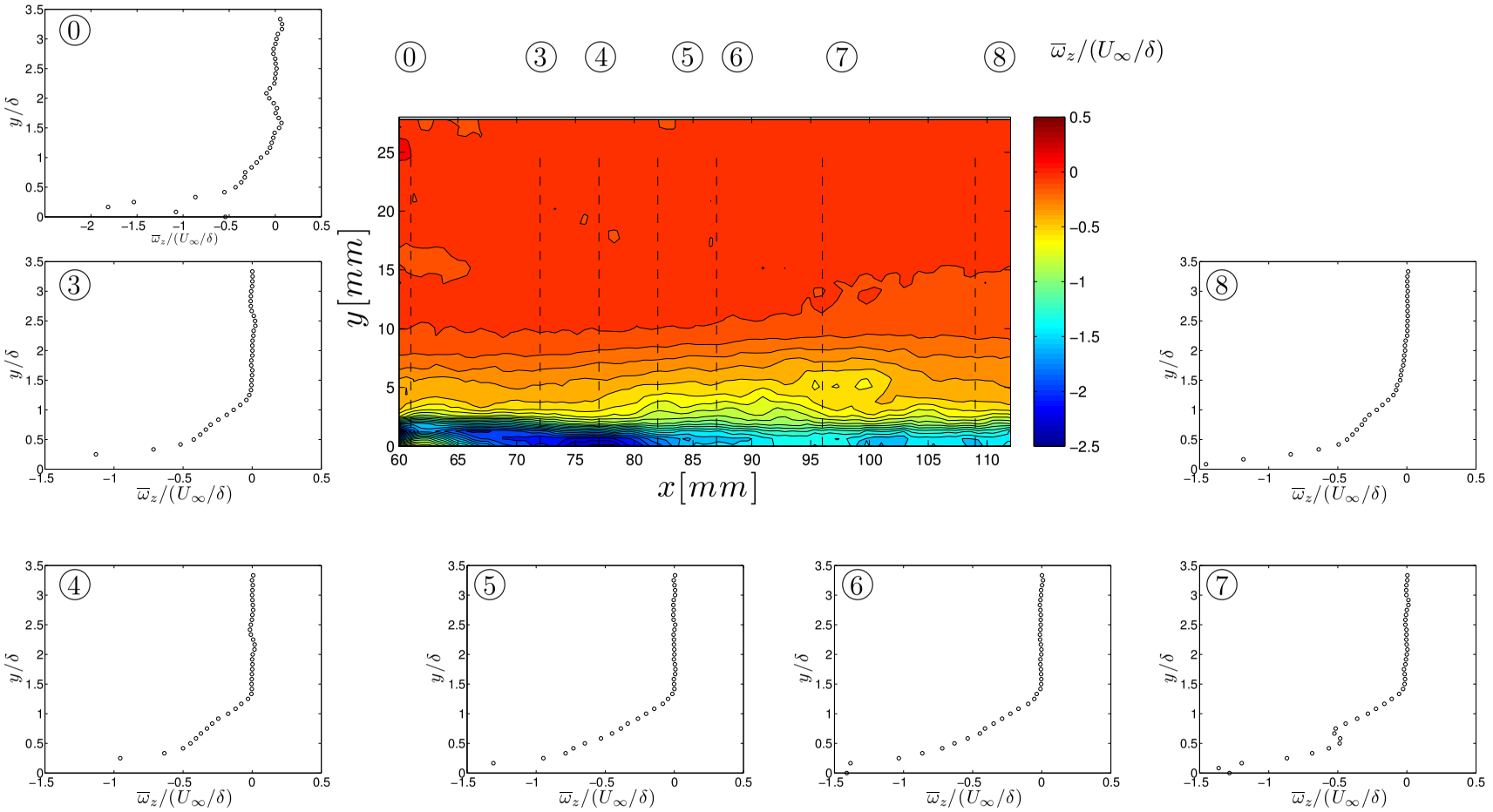

Figure B.16: Evolution of $\overline{\omega}_z/(U_\infty/\delta)$ through the z=18mm SBLI region for a flow deflection angle of $\theta = 6$ deg. Sampling numbers correspond to transverse plane sampling locations, location '0' indicating the region where U_∞ was sampled. At top, colors show the $\overline{\omega}_z/(U_\infty/\delta)$ field throughout each sampling plane, and also indicate their relative locations.

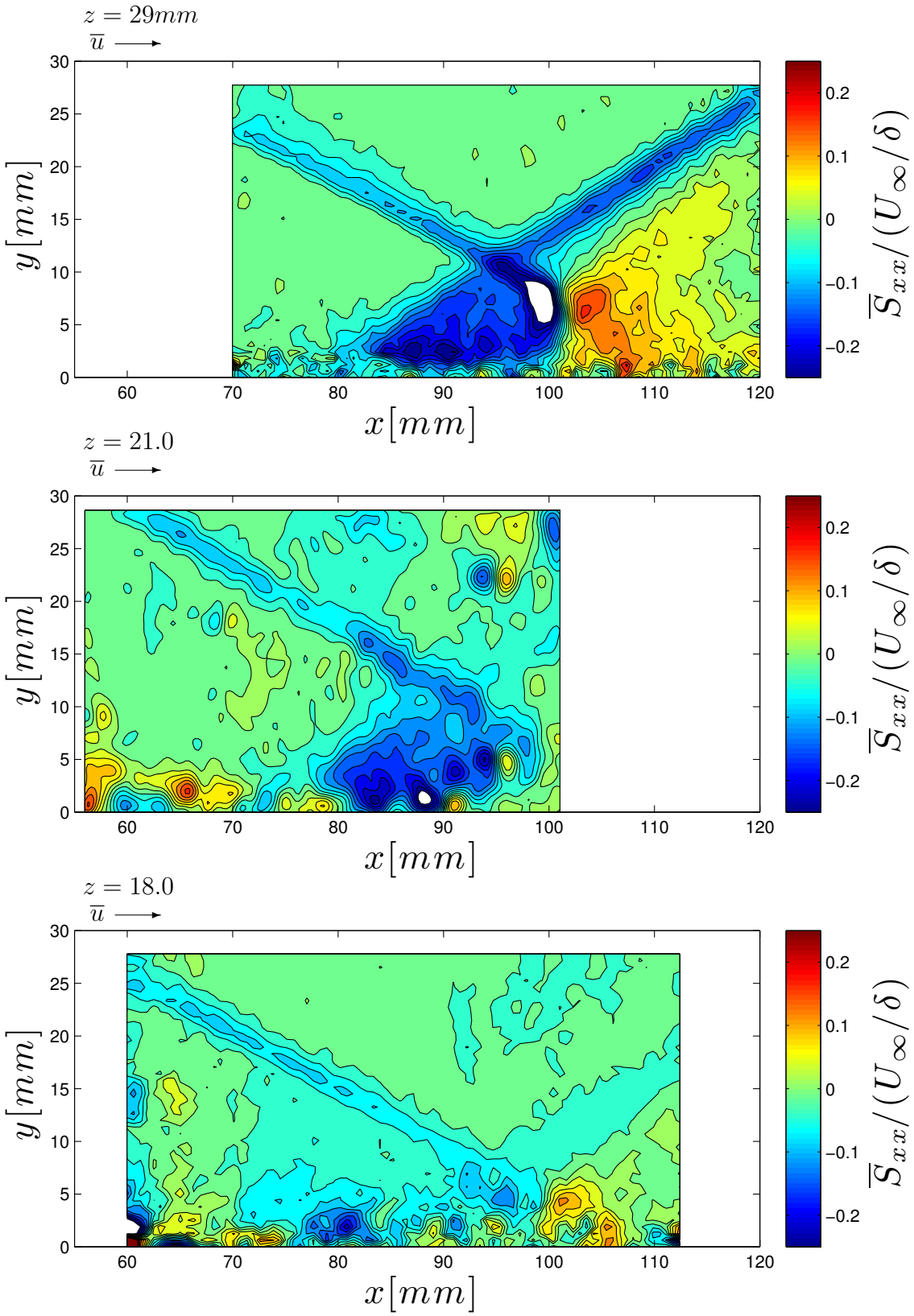

Figure B.17: Normal strain component $\overline{S}_{xx}/U_\infty/\delta)$ for each of the three planes oriented in the streamwise direction.

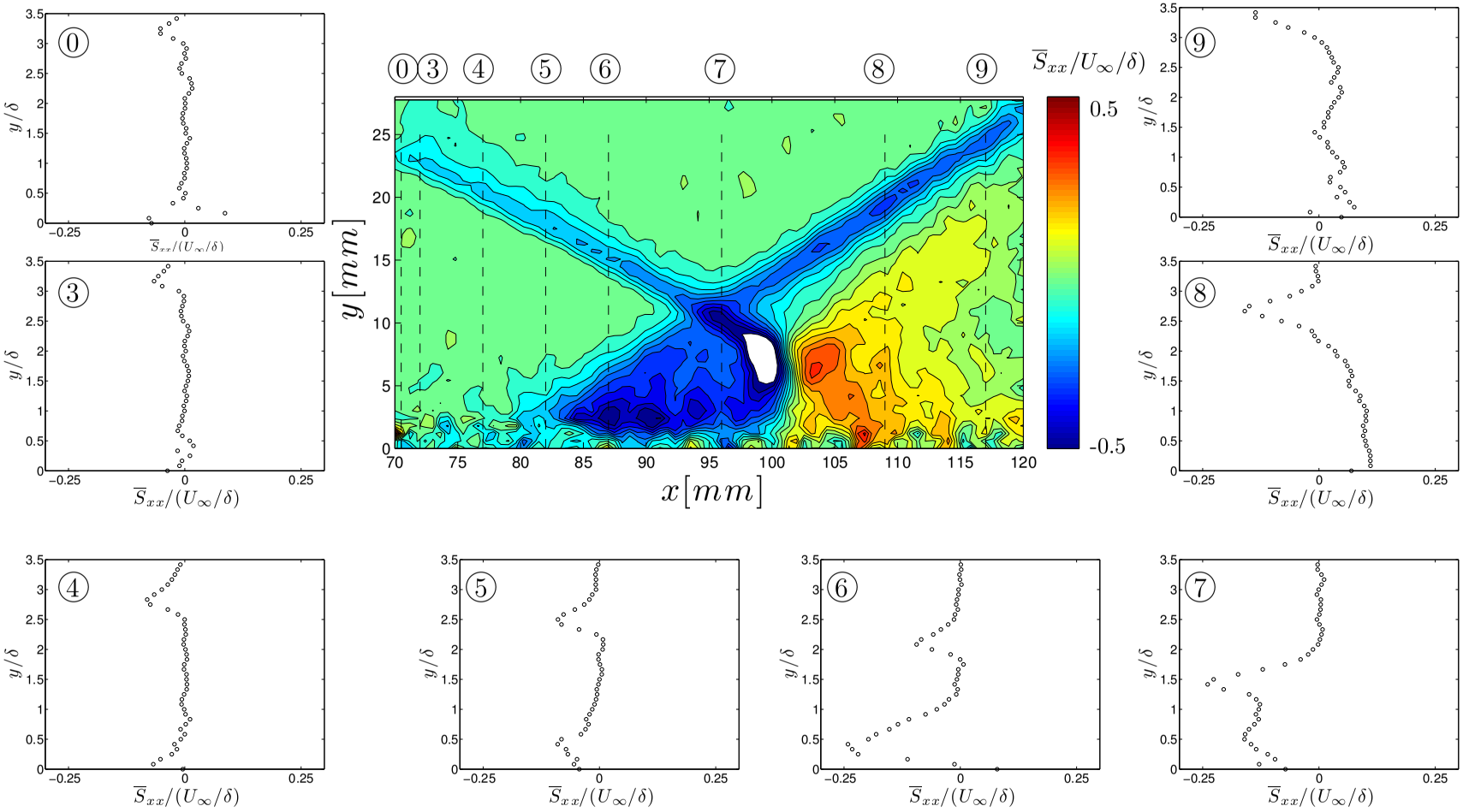

Figure B.18: Evolution of $\overline{S}_{xx}/U_\infty/\delta)$ through the z=29mm SBLI region for a flow deflection angle of $\theta = 6$ deg. Sampling numbers correspond to transverse plane sampling locations, location '0' indicating the region where U_∞ was calculated. At top, colors show the $\overline{S}_{xx}/(U_\infty/\delta)$ field throughout each sampling plane, and also indicate their relative locations.

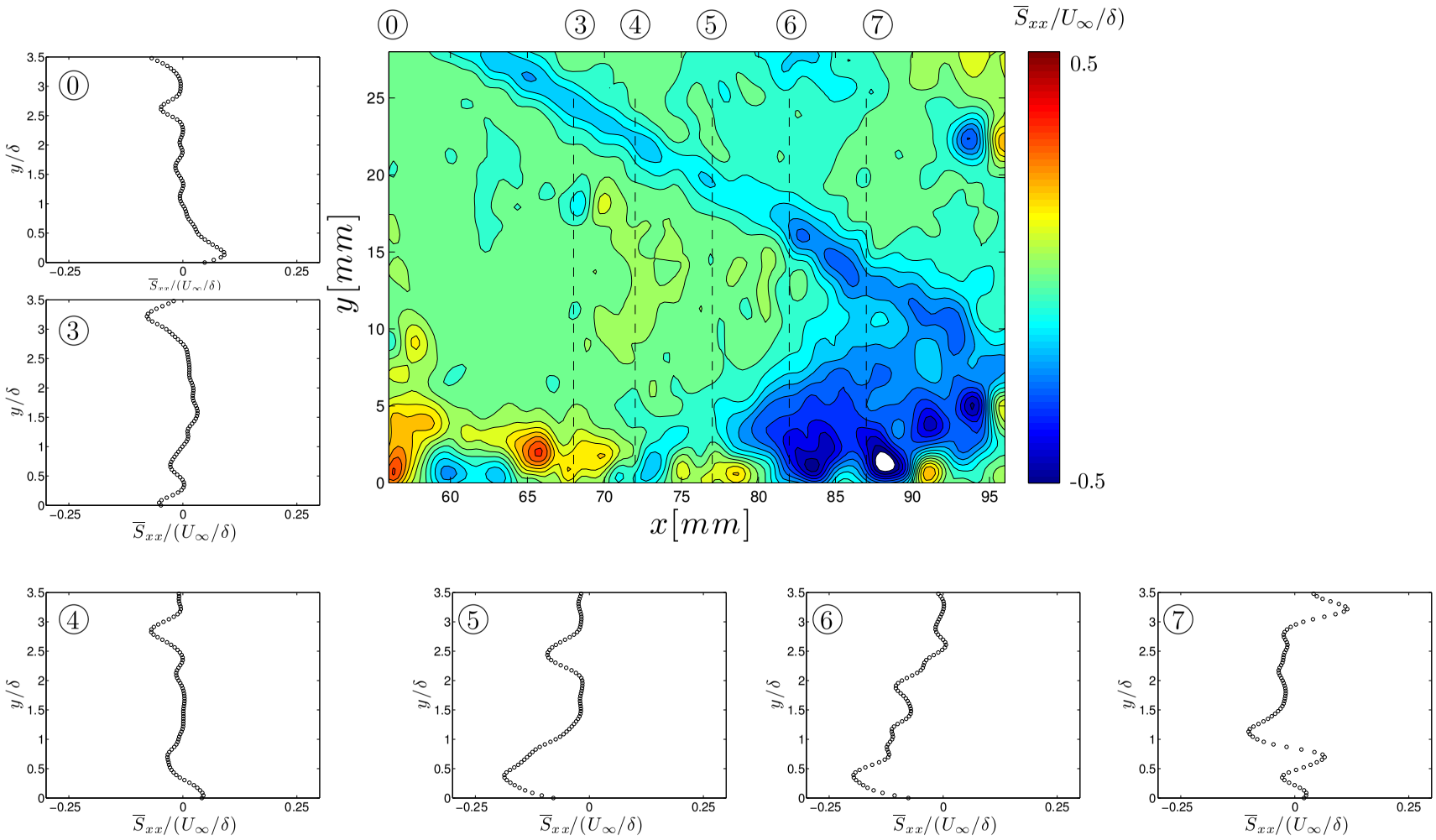

Figure B.19: Evolution of $\overline{S}_{xx}/(U_\infty/\delta)$through the z=21mm SBLI region for a flow deflection angle of $\theta = 6$ deg. Sampling numbers correspond to transverse plane sampling locations, location '0' indicating the region where U_∞ was calculated. At top, colors show the $\overline{S}_{xx}/(U_\infty/\delta)$ field throughout each sampling plane, and also indicate their relative locations.

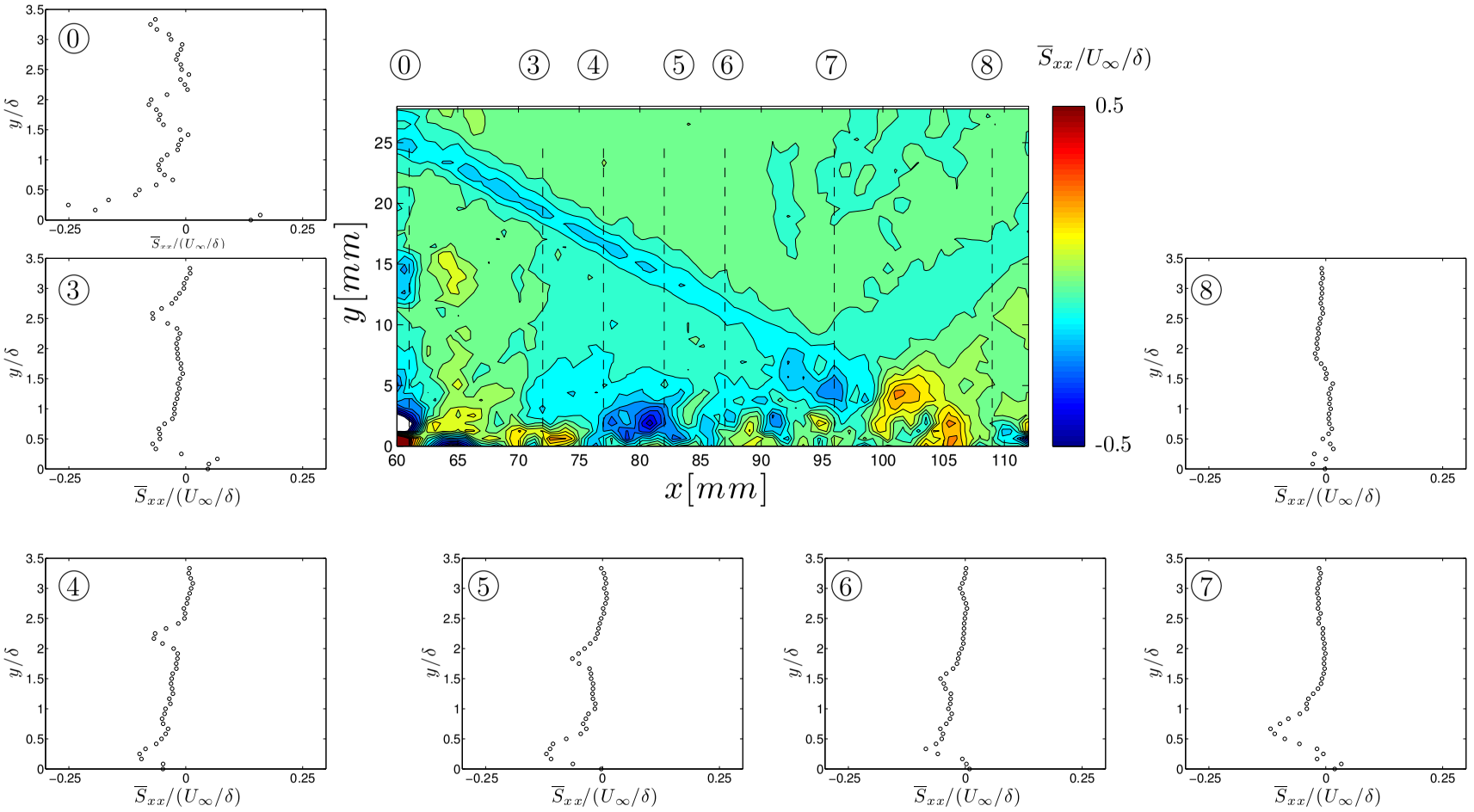

Figure B.20: Evolution of $\overline{S}_{xx}/(U_\infty/\delta)$ through the z=18mm SBLI region for a flow deflection angle of $\theta = 6$ deg. Sampling numbers correspond to transverse plane sampling locations, location '0' indicating the region where U_∞ was calculated. At top, colors show the $\overline{S}_{xx}/(U_\infty/\delta)$ field throughout each sampling plane, and also indicate their relative locations.

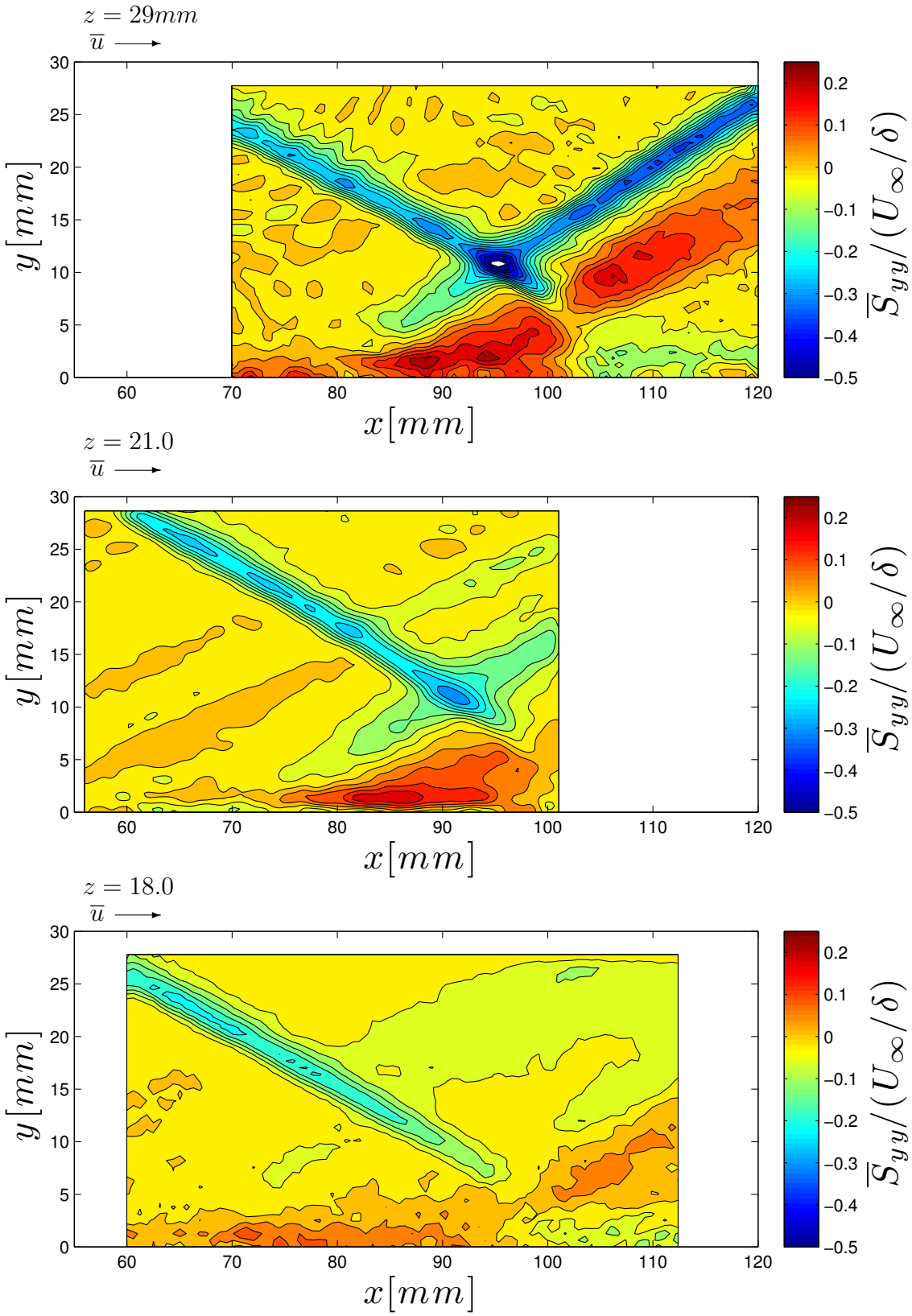

Figure B.21: Normal strain component $\overline{S}_{yy}/(U_\infty/\delta)$ for each of the three planes oriented in the streamwise direction.

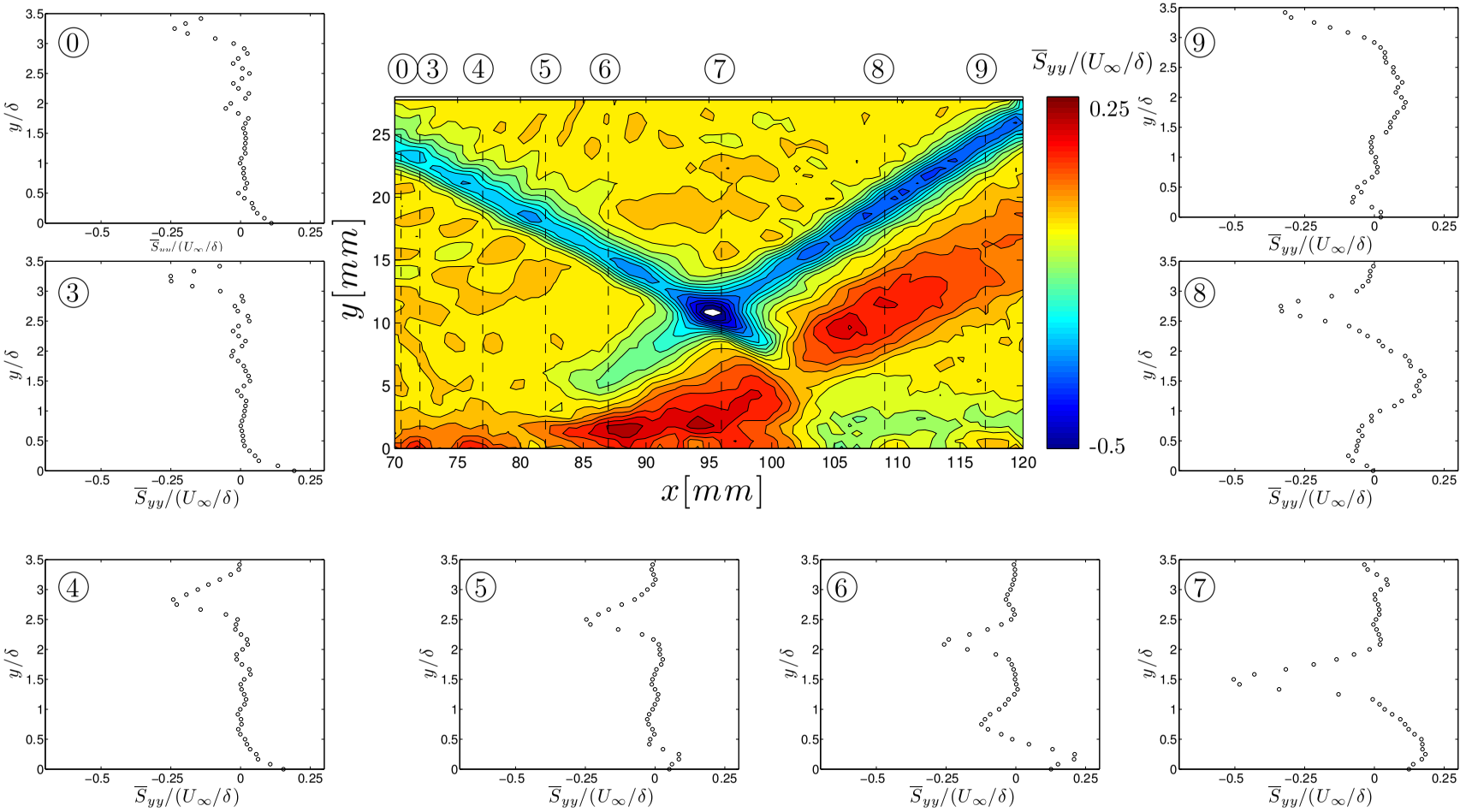

Figure B.22: Evolution of $\overline{S}_{yy}/(U_\infty/\delta)$ through the z=29mm SBLI region for a flow deflection angle of $\theta = 6$ deg. Sampling numbers correspond to transverse plane sampling locations, location '0' indicating the region where U_∞ was calculated. At top, colors show the $\overline{S}_{yy}/(U_\infty/\delta)$ field throughout each sampling plane, and also indicate their relative locations.

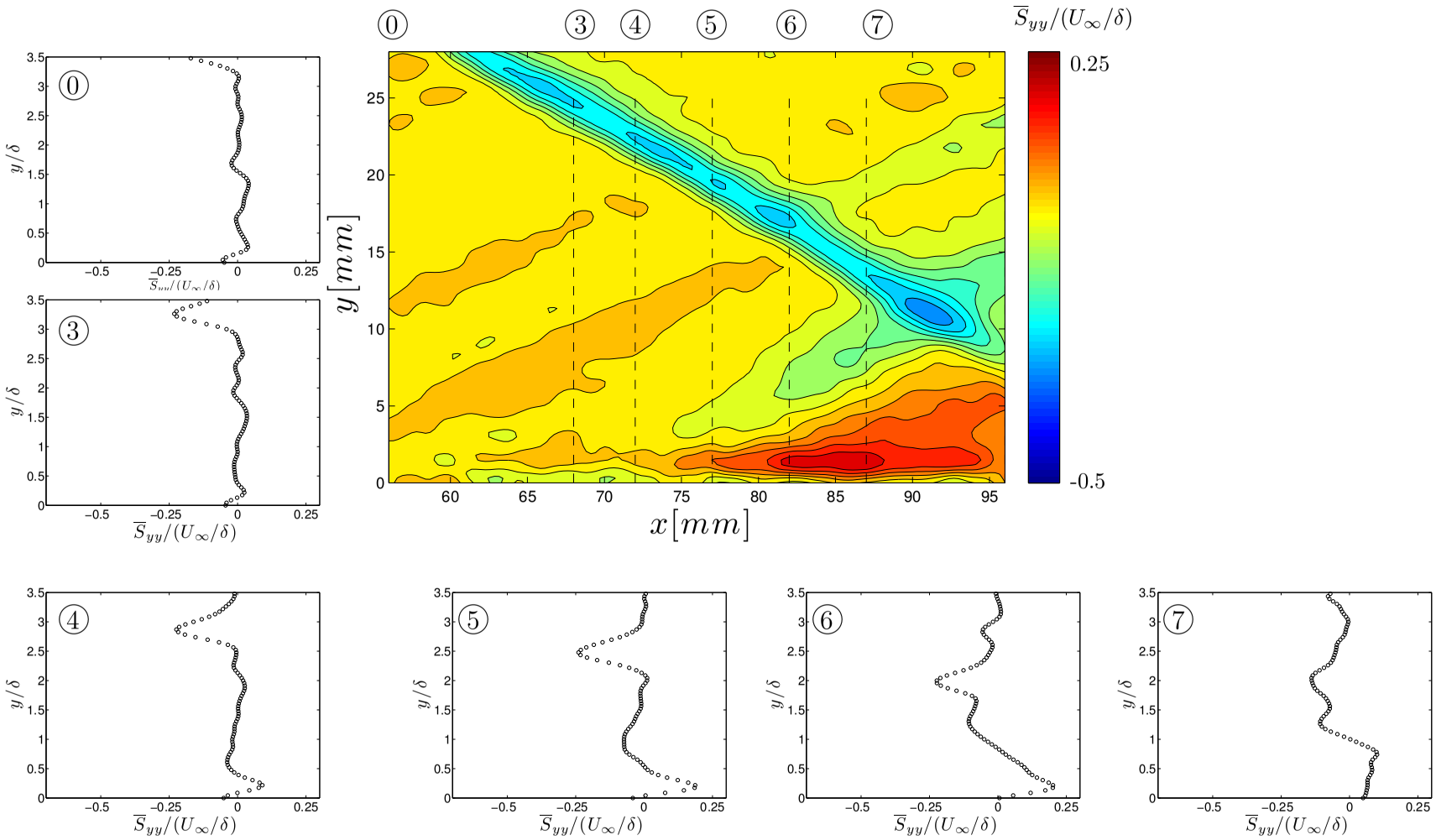

Figure B.23: Evolution of $\overline{S}_{yy}/(U_\infty/\delta)$through the z=21mm SBLI region for a flow deflection angle of $\theta = 6$ deg. Sampling numbers correspond to transverse plane sampling locations, location '0' indicating the region where U_∞ was calculated. At top, colors show the $\overline{S}_{yy}/(U_\infty/\delta)$ field throughout each sampling plane, and also indicate their relative locations.

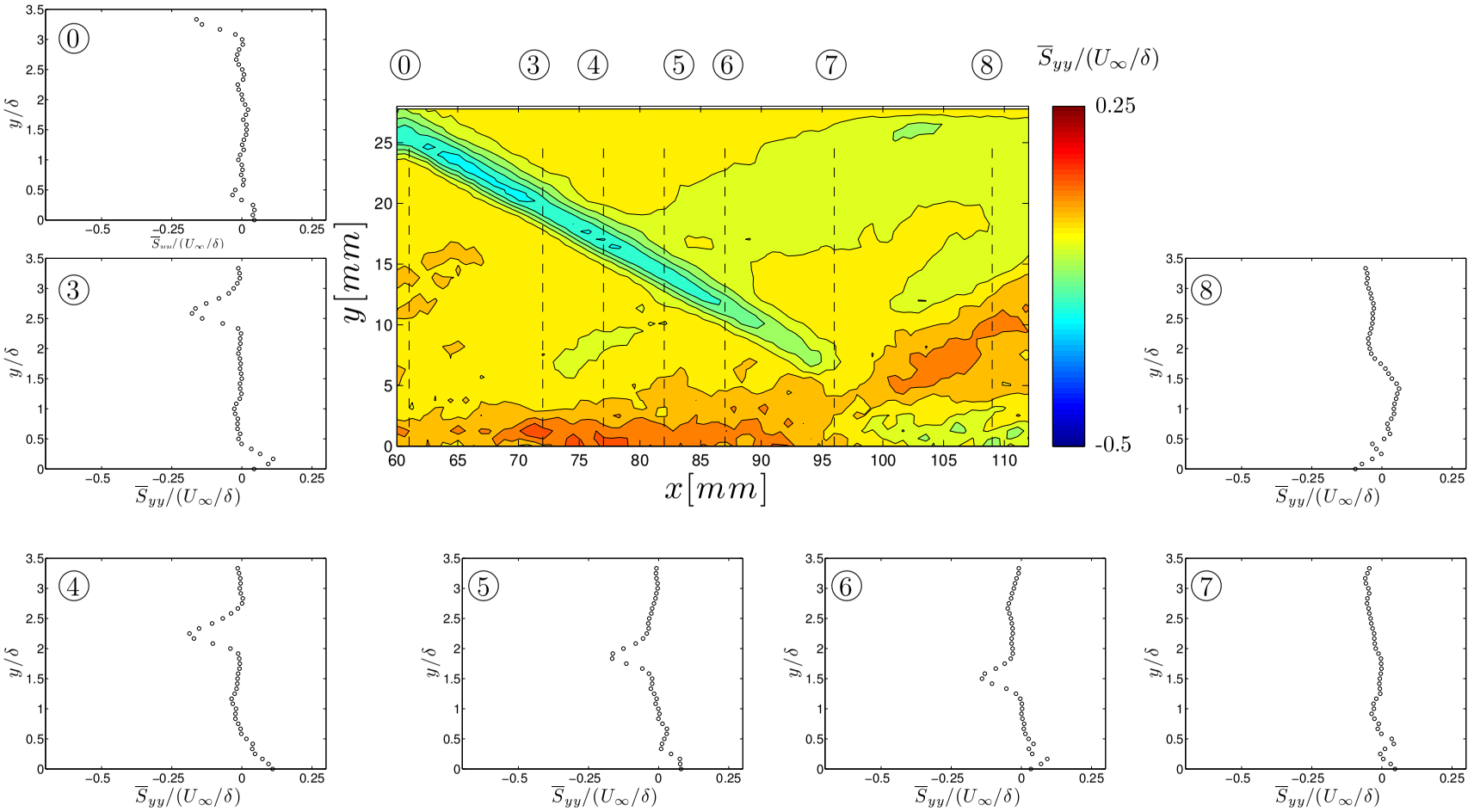

Figure B.24: Evolution of $\overline{S}_{yy}/(U_\infty/\delta)$ through the z=18mm SBLI region for a flow deflection angle of $\theta = 6$ deg. Sampling numbers correspond to transverse plane sampling locations, location '0' indicating the region where U_∞ was calculated. At top, colors show the $\overline{S}_{yy}/(U_\infty/\delta)$ field throughout each sampling plane, and also indicate their relative locations.

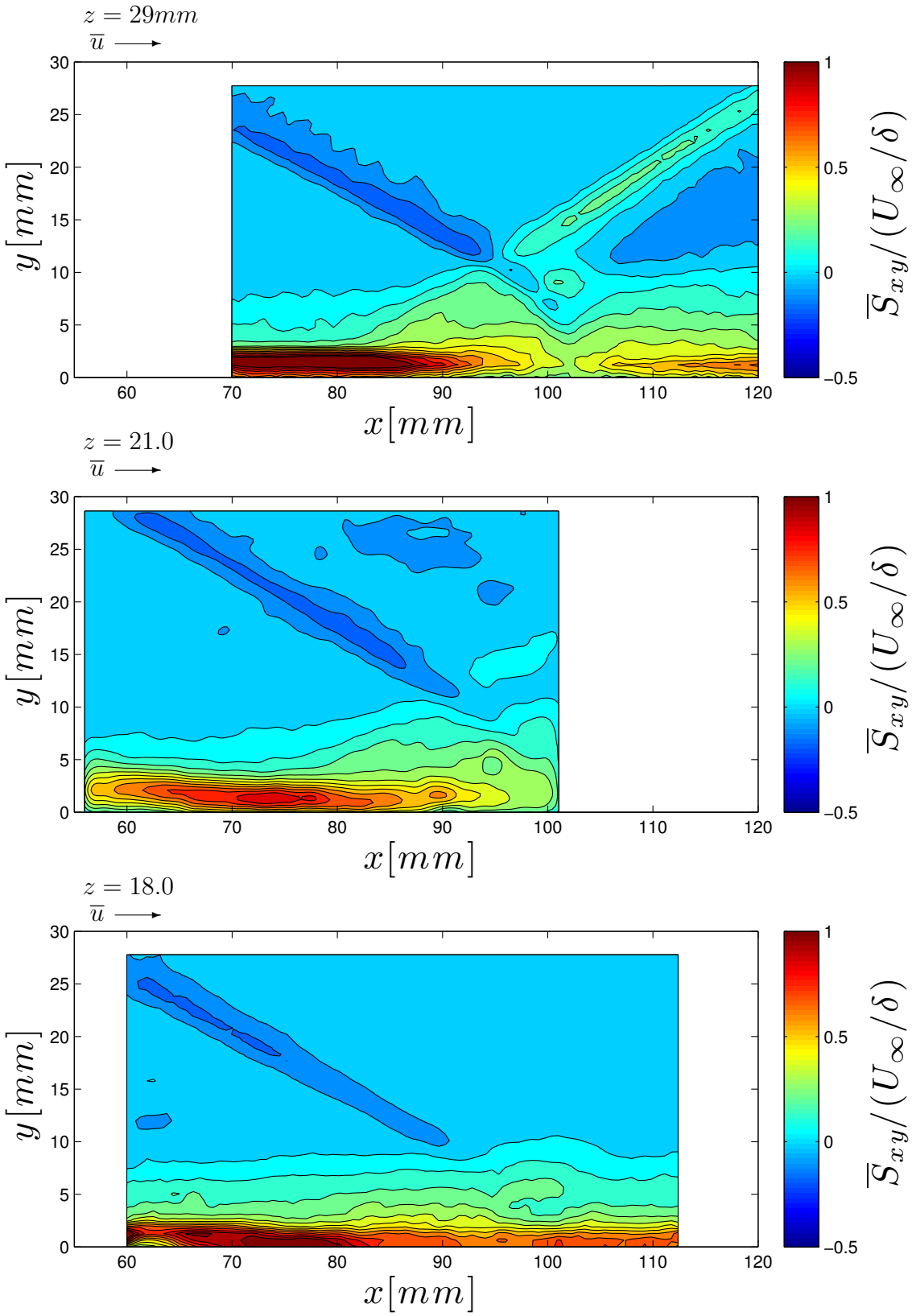

Figure B.25: Shear strain component $\overline{S}_{xy}/(U_\infty/\delta)$ for each of the three planes oriented in the streamwise direction.

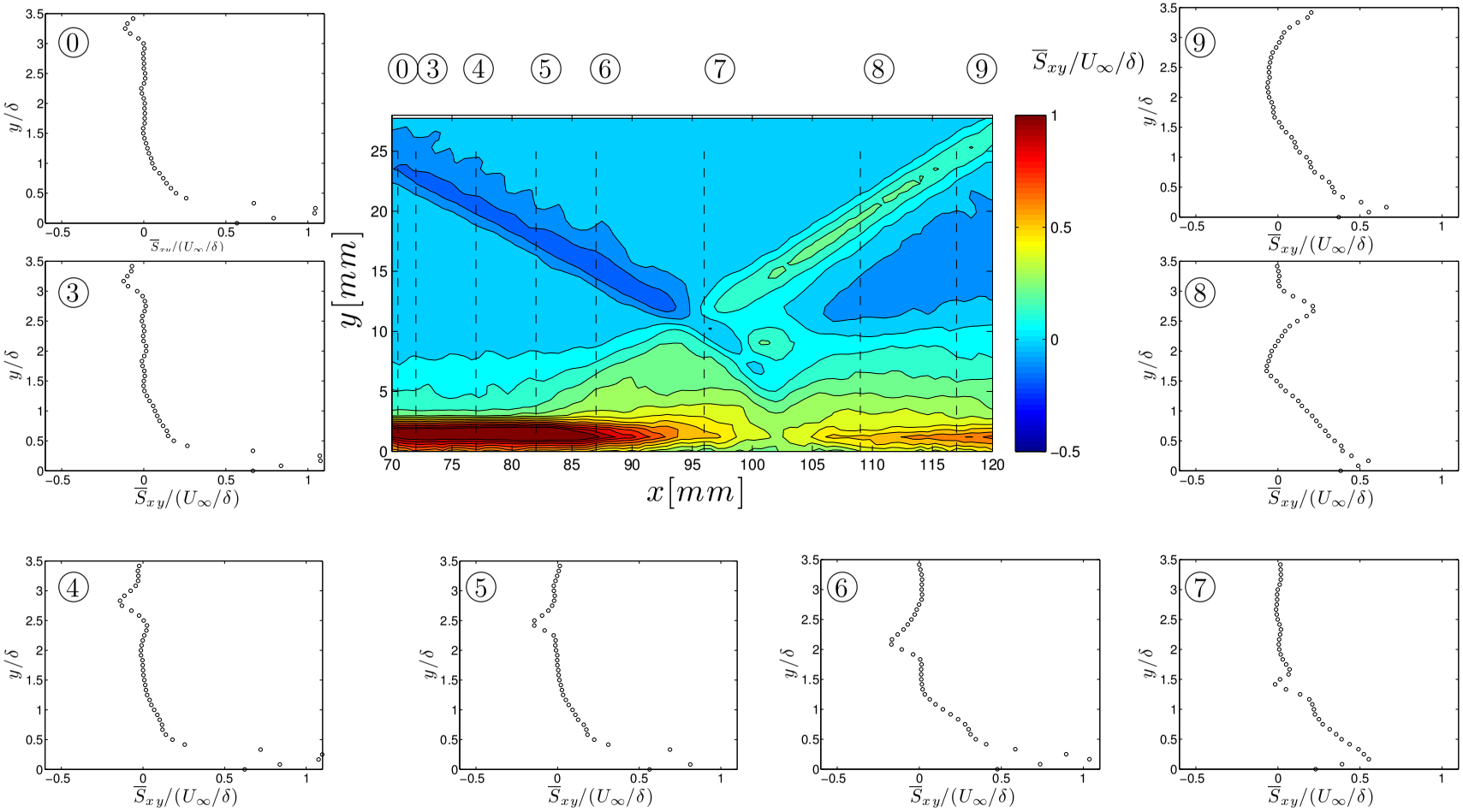

Figure B.26: Evolution of $\overline{S}_{xy}/(U_\infty/\delta)$ through the z=29mm SBLI region for a flow deflection angle of $\theta = 6$ deg. Sampling numbers correspond to transverse plane sampling locations, location '0' indicating the region where U_∞ was calculated. At top, colors show the $\overline{S}_{xy}/(U_\infty/\delta)$ field throughout each sampling plane, and also indicate their relative locations.

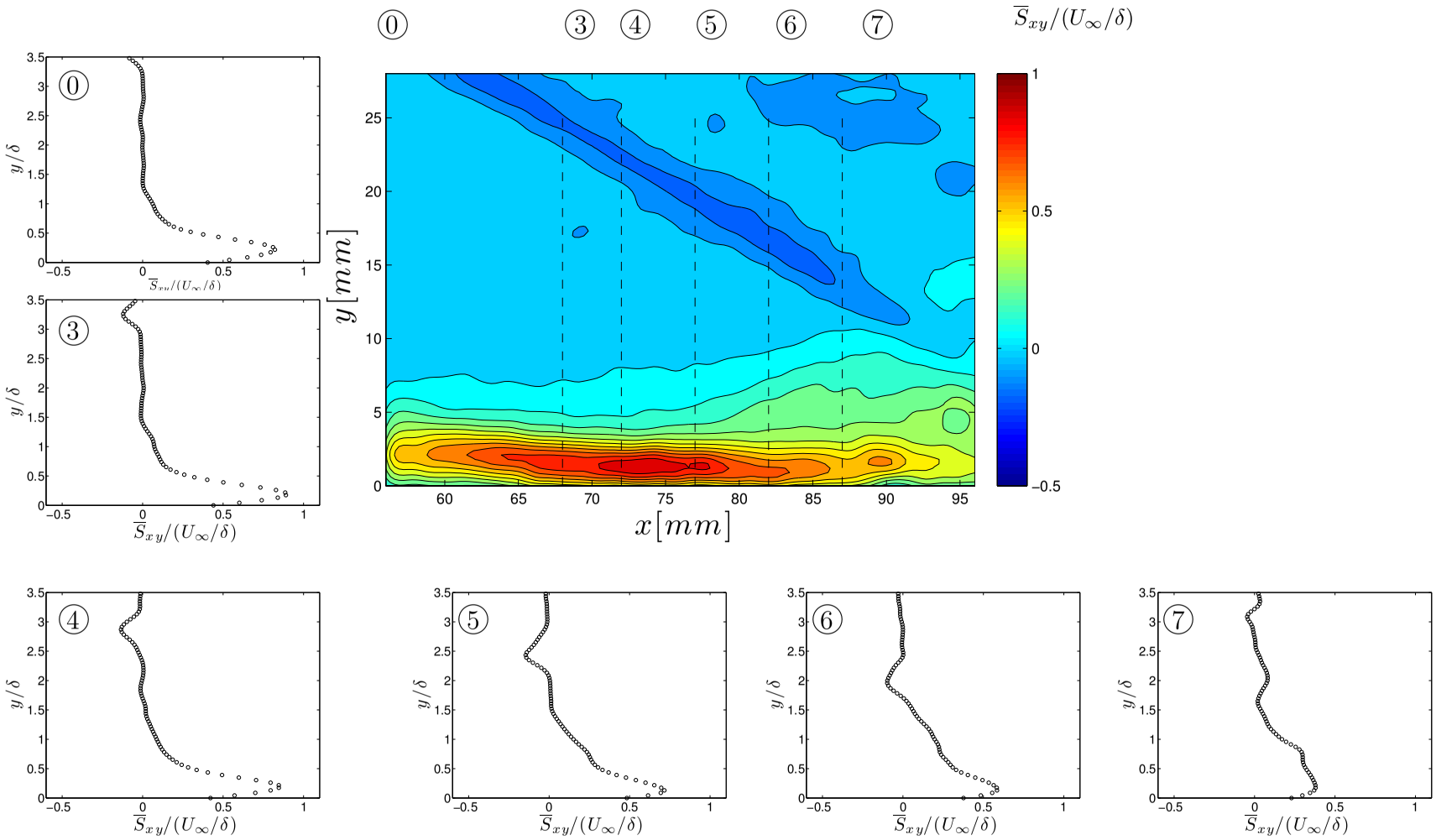

Figure B.27: Evolution of $\overline{S}_{xy}/(U_\infty/\delta)$through the z=21mm SBLI region for a flow deflection angle of $\theta = 6$ deg. Sampling numbers correspond to transverse plane sampling locations, location '0' indicating the region where U_∞ was calculated. At top, colors show the $\overline{S}_{xy}/(U_\infty/\delta)$ field throughout each sampling plane, and also indicate their relative locations.

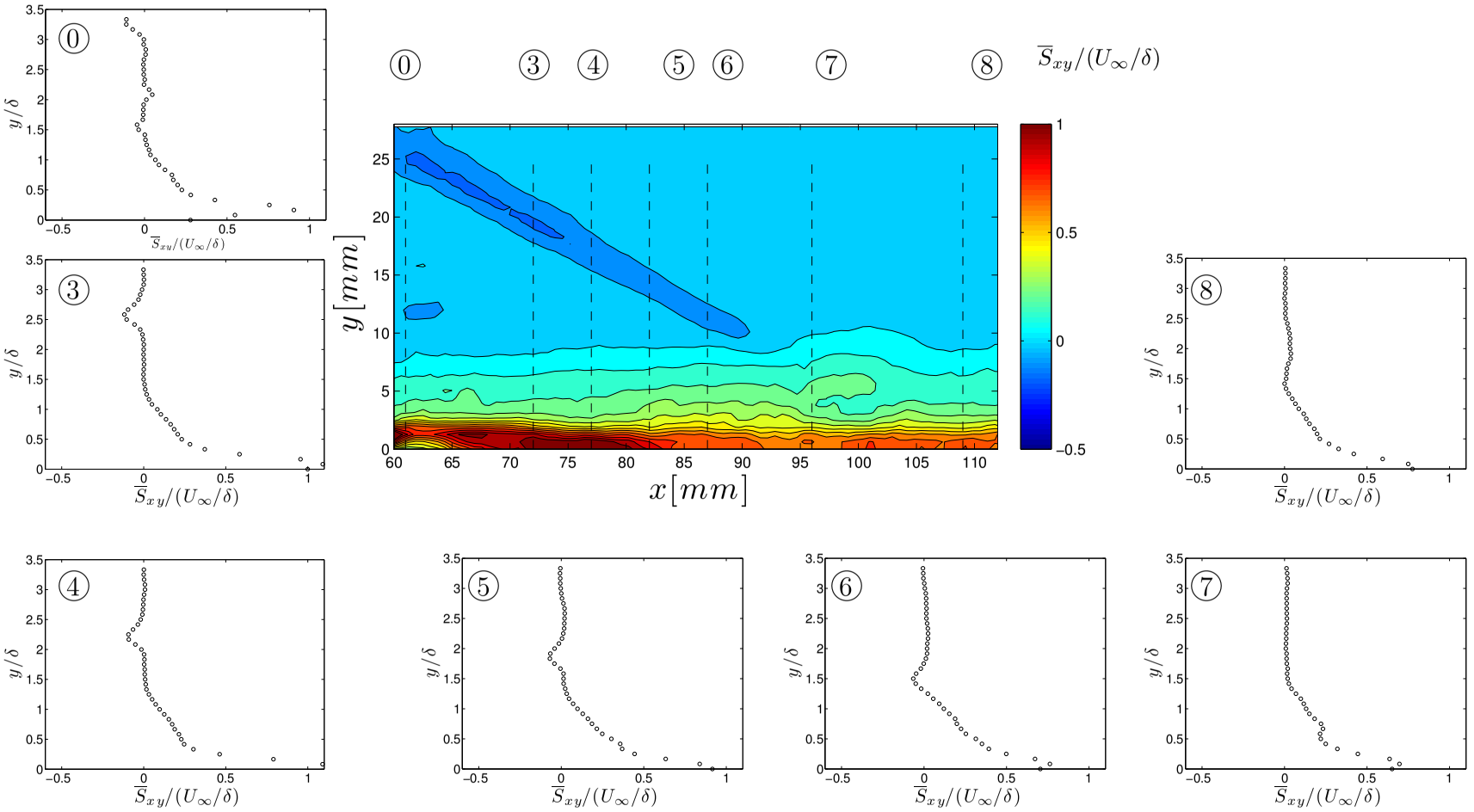

Figure B.28: Evolution of $\overline{S}_{xy}/(U_\infty/\delta)$ through the z=18mm SBLI region for a flow deflection angle of $\theta = 6$ deg. Sampling numbers correspond to transverse plane sampling locations, location '0' indicating the region where U_∞ was calculated. At top, colors show the $\overline{S}_{xy}/(U_\infty/\delta)$ field throughout each sampling plane, and also indicate their relative locations.

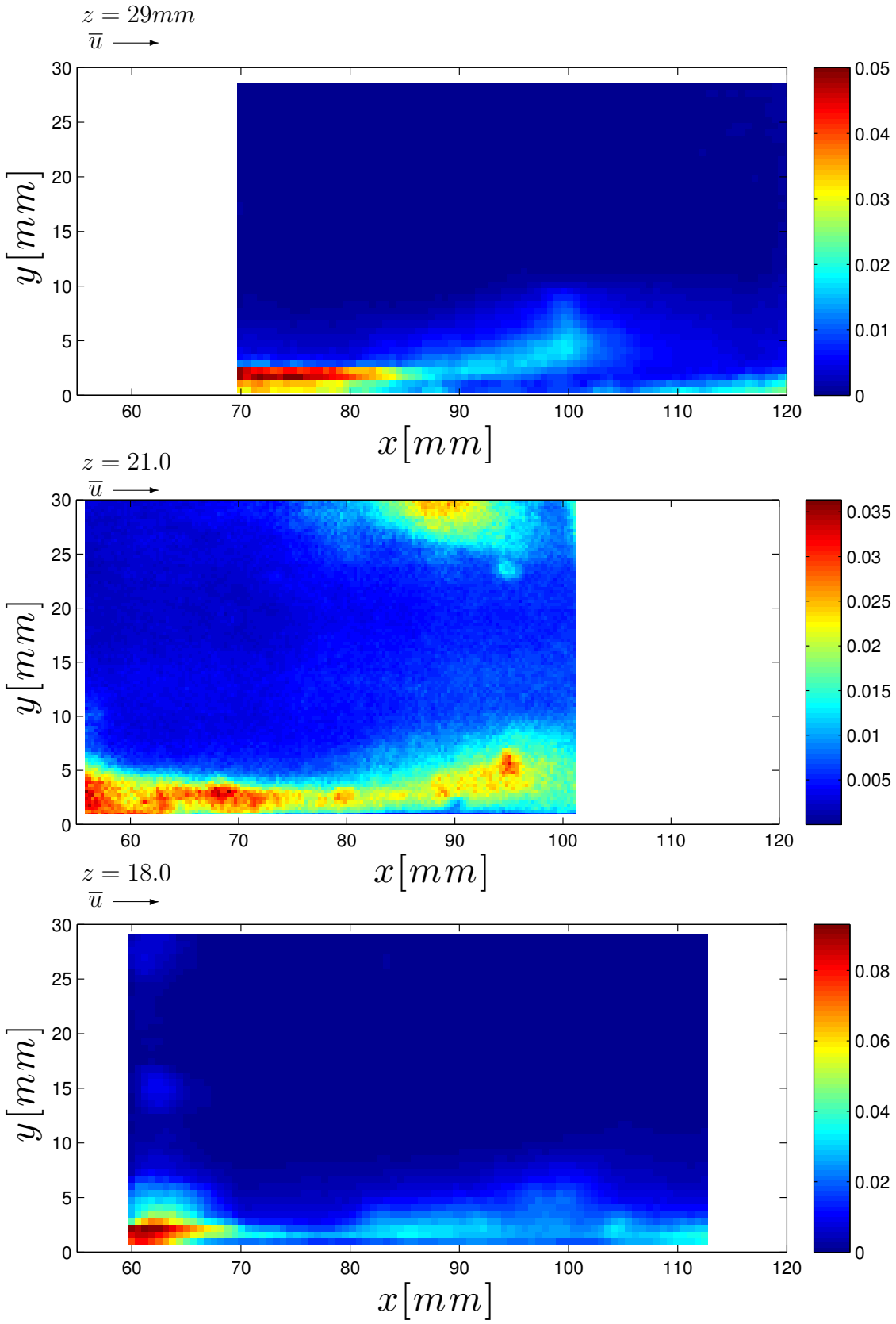

Figure B.29: RMS Fluctuations of the velocity, $\overline{u'^2}$ for each of the three planes oriented in the streamwise direction.

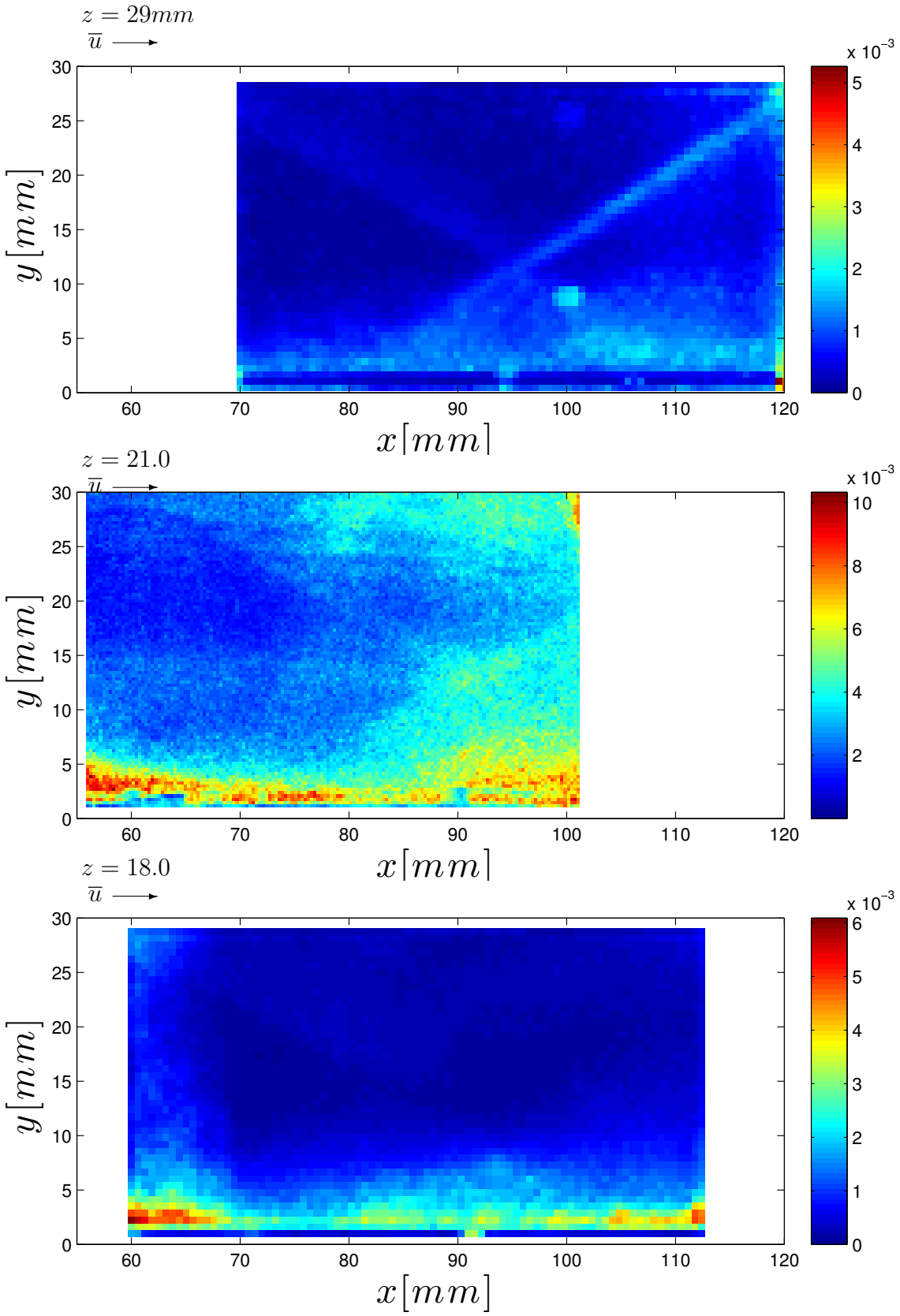

Figure B.30: RMS Fluctuations of the velocity, $\overline{v'^2}$ for each of the three planes oriented in the streamwise direction.

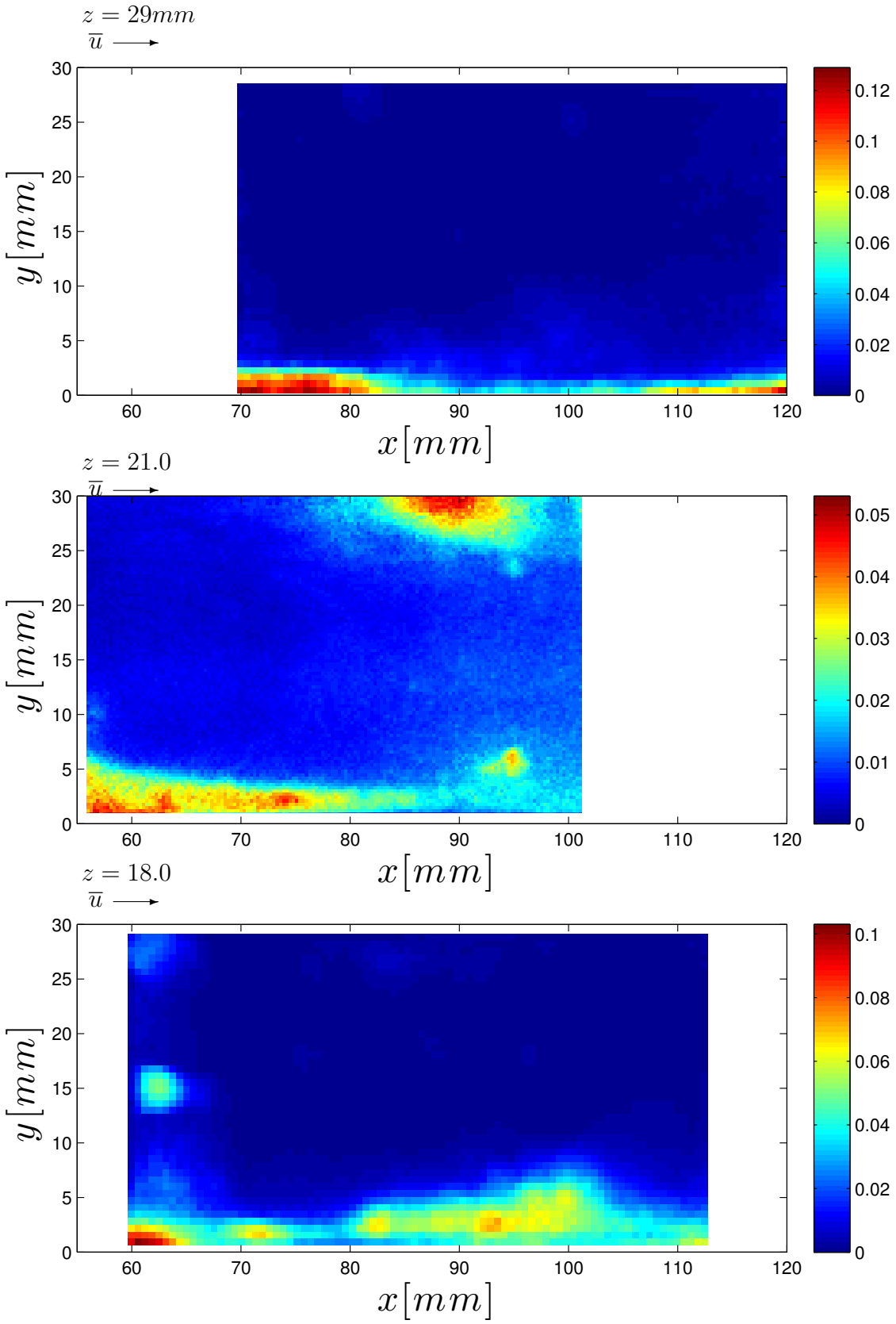

Figure B.31: RMS Fluctuations of the velocity, $\overline{w'^2}$ for each of the three planes oriented in the streamwise direction.

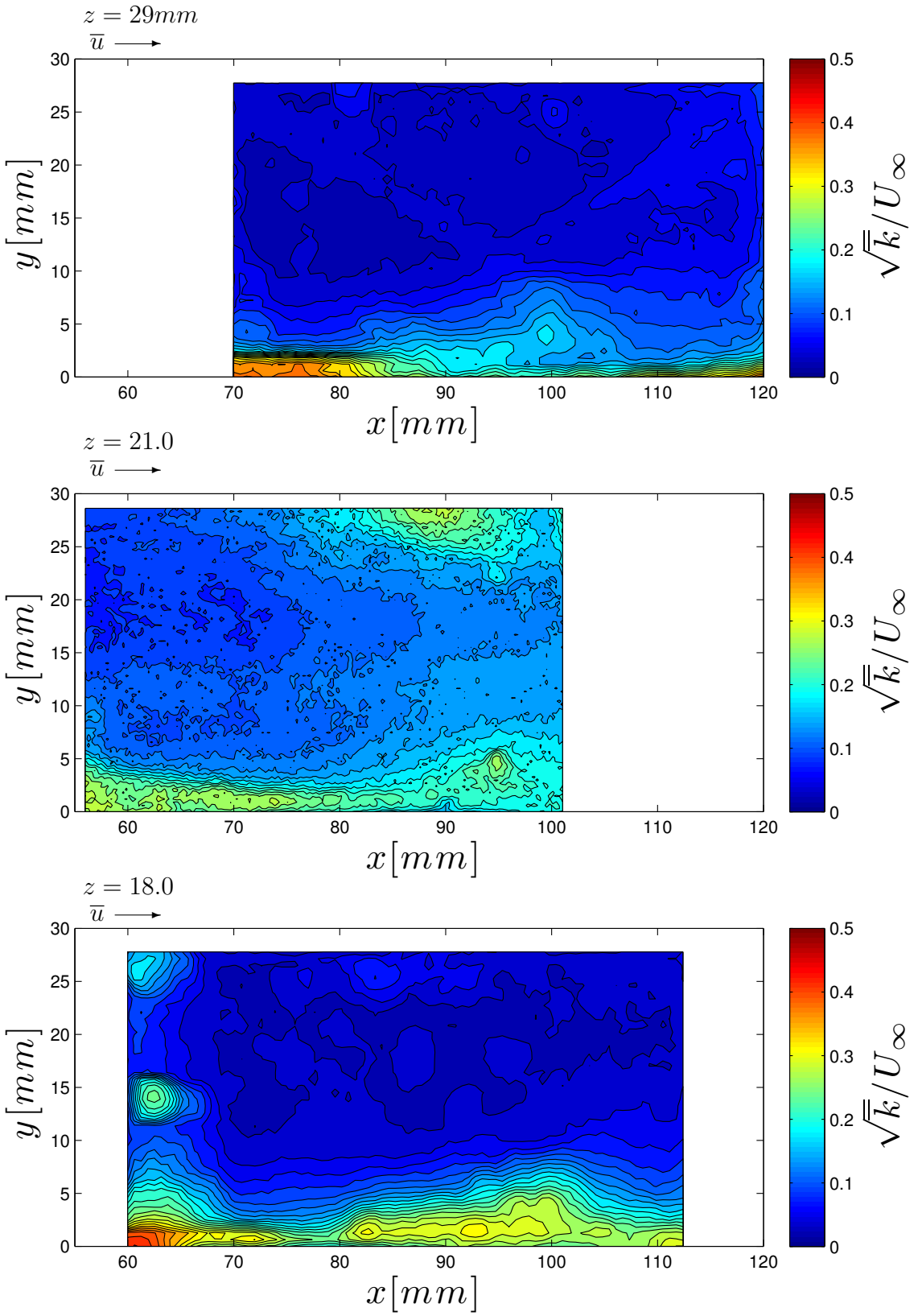

Figure B.32: Turbulent kinetic energy $\sqrt{\overline{k}}/U_\infty$ for each of the three vertical planes oriented in the streamwise direction.

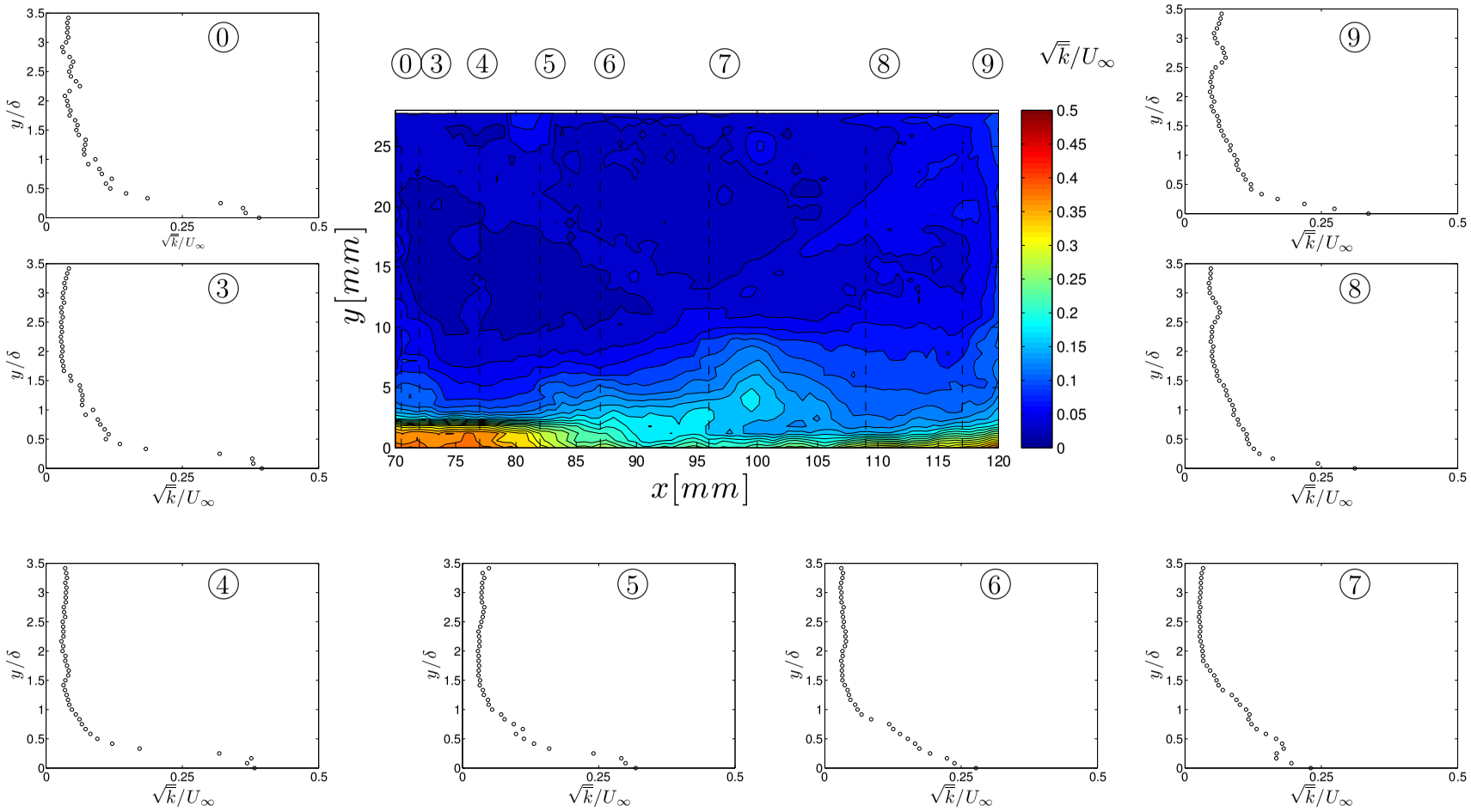

Figure B.33: Evolution of $\sqrt{\overline{k}}/U_\infty$ through the z=29mm SBLI region for a flow deflection angle of $\theta = 6$ deg. Sampling numbers correspond to transverse plane sampling locations, location '0' indicating the region where U_∞ was calculated. At top, colors show the $\sqrt{\overline{k}}/U_\infty$ field throughout each sampling plane, and also indicate their relative locations.

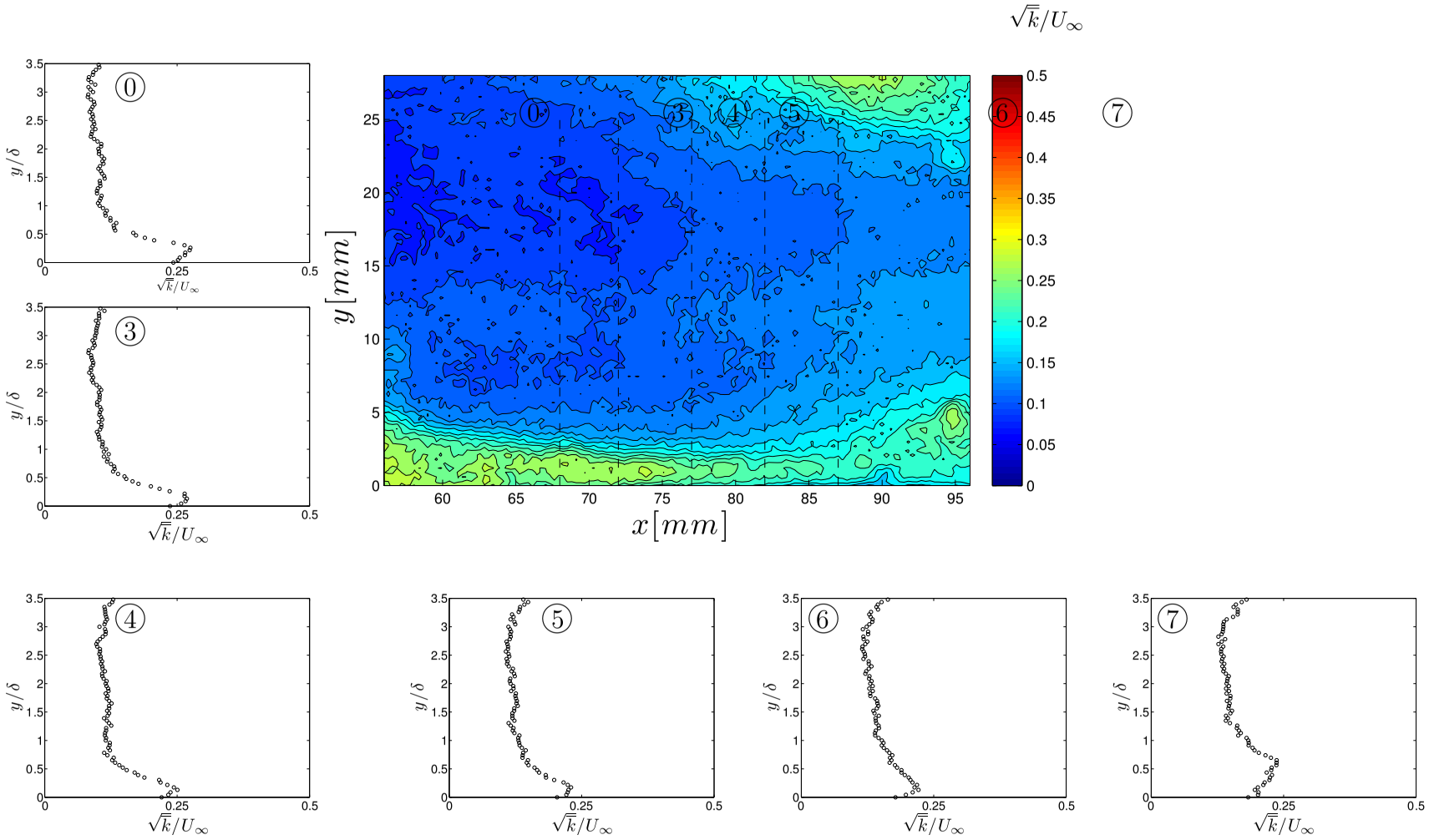

Figure B.34: Evolution of $\sqrt{\overline{k}}/U_\infty$through the z=21mm SBLI region for a flow deflection angle of $\theta = 6$ deg. Sampling numbers correspond to transverse plane sampling locations, location '0' indicating the region where U_∞ was calculated. At top, colors show the $\sqrt{\overline{k}}/U_\infty$ field throughout each sampling plane, and also indicate their relative locations.

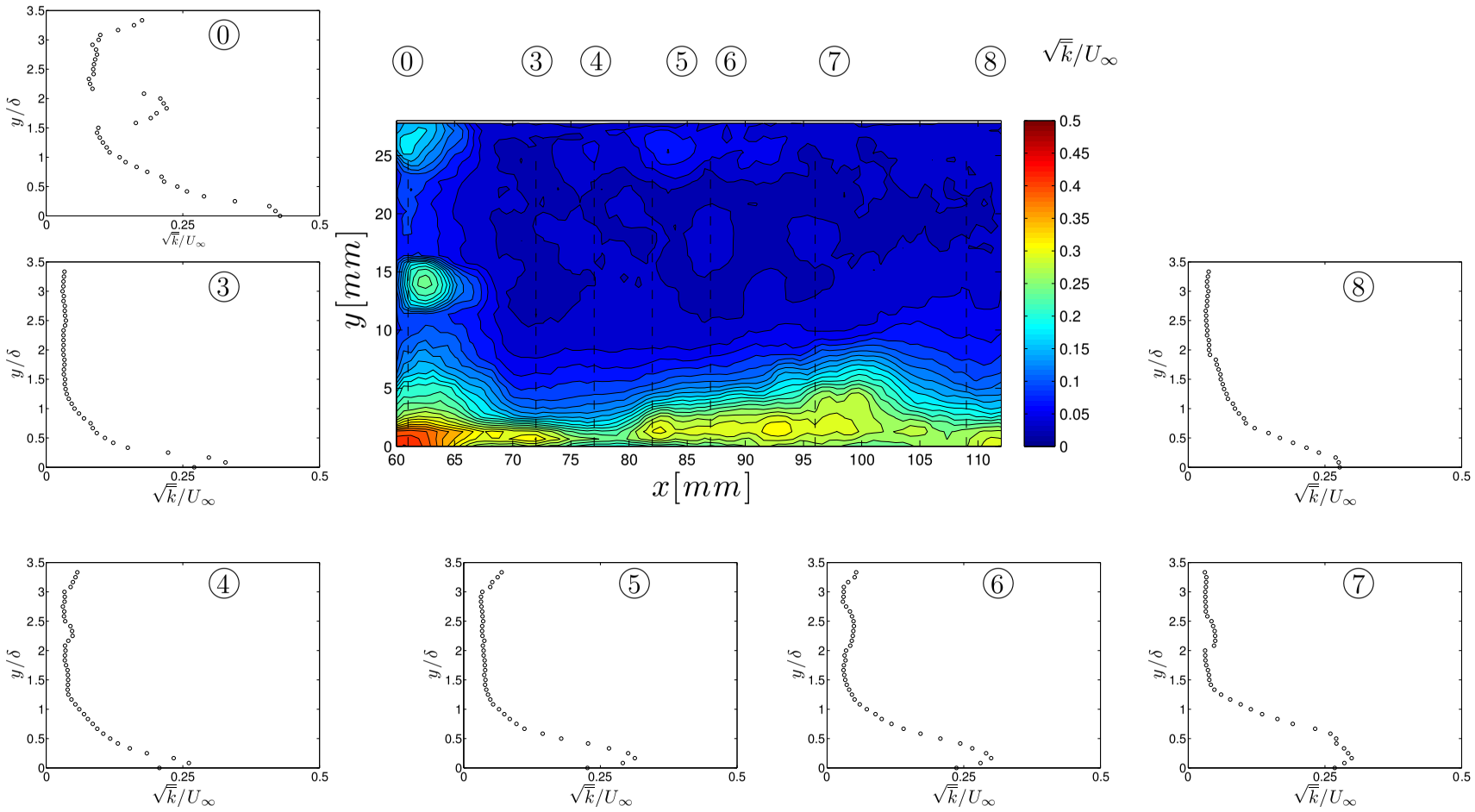

Figure B.35: Evolution of $\sqrt{\overline{k}}/U_\infty$ through the z=18mm SBLI region for a flow deflection angle of $\theta = 6$ deg. Sampling numbers correspond to transverse plane sampling locations, location '0' indicating the region where U_∞ was calculated. At top, colors show the $\sqrt{\overline{k}}/U_\infty$ field throughout each sampling plane, and also indicate their relative locations.

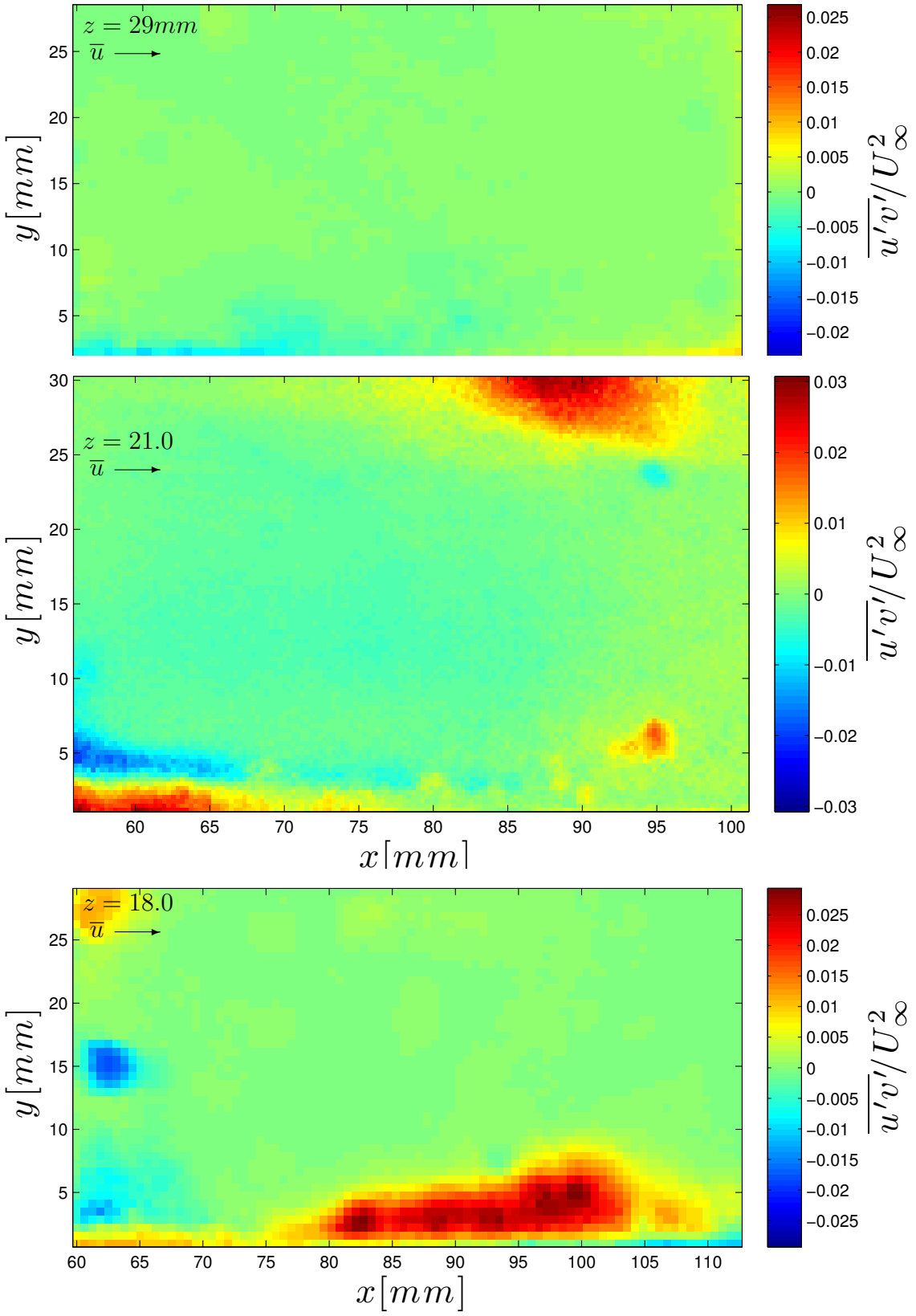

Figure B.36: Visualizations of the normalized Reynold's stress component $\overline{u'v'}$ for each of the three planes oriented in the streamwise direction.

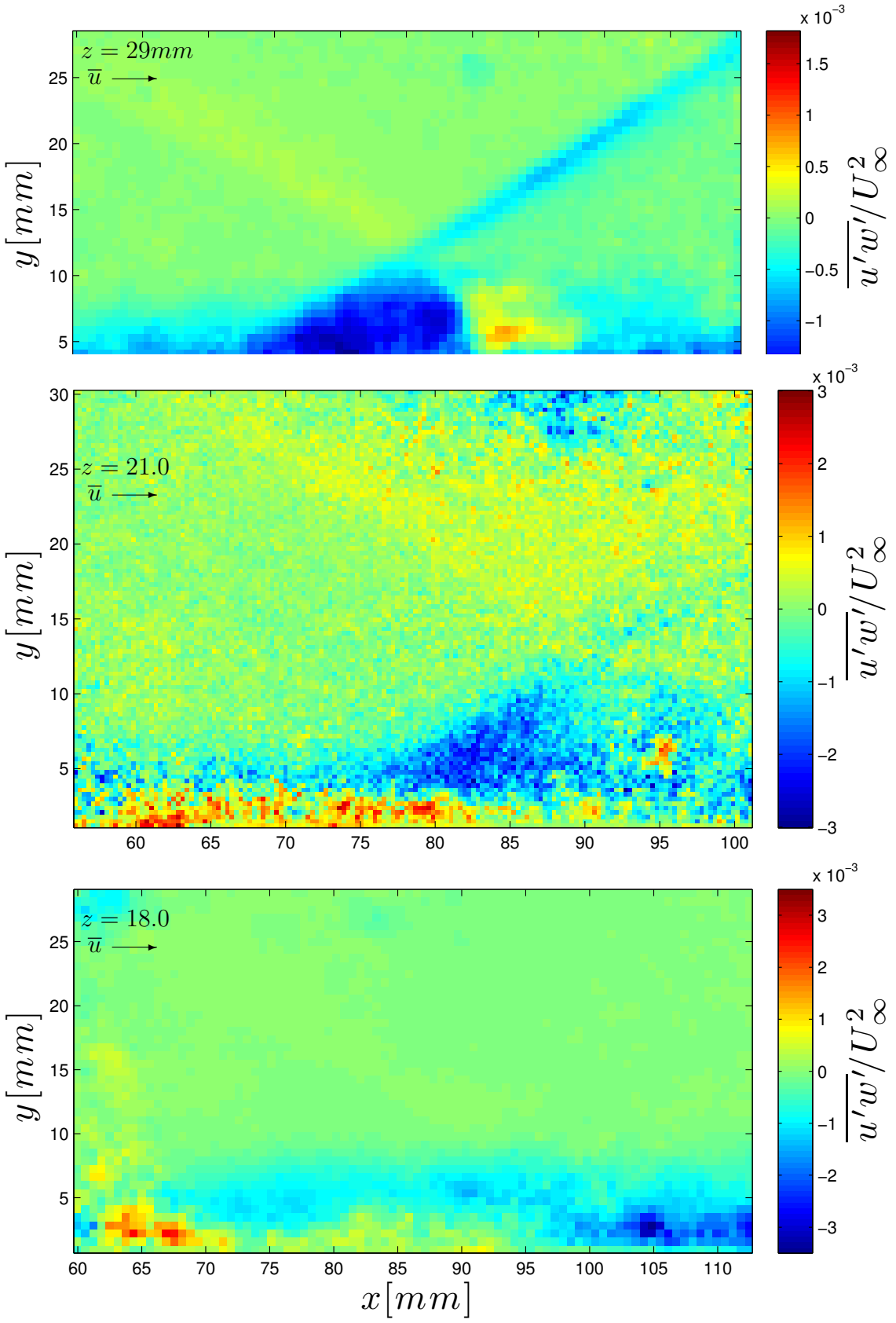

Figure B.37: Visualizations of the normalized Reynold's stress component $\overline{u'w'}$ for each of the three planes oriented in the streamwise direction.

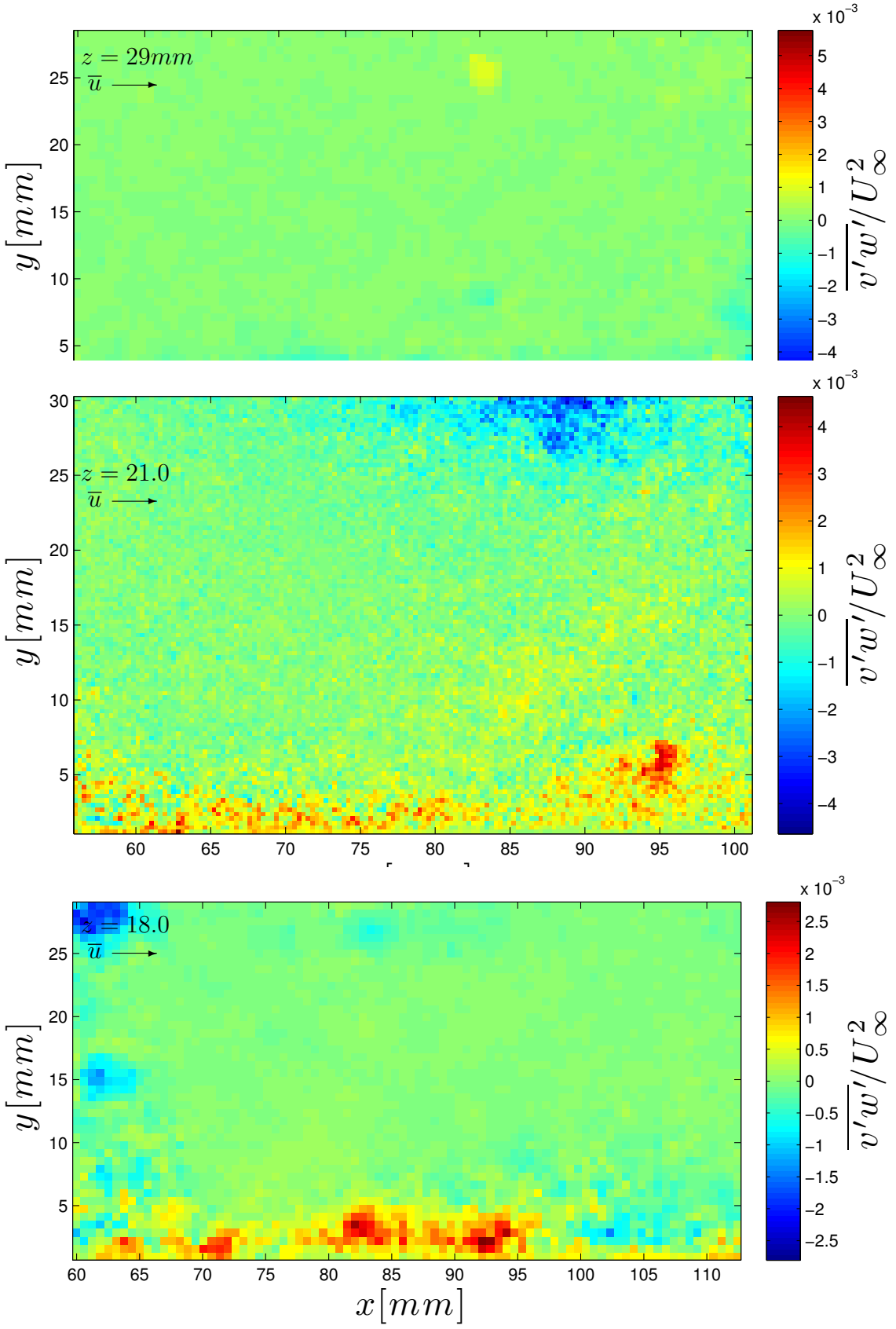

Figure B.38: Visualizations of the normalized Reynold's stress component $\overline{v'w'}$ for each of the three planes oriented in the streamwise direction.

APPENDIX C

Streamwise Horizontal Data

This section presents data from the streamwise horizontal planes which were not presented in the main body of the thesis. The data is presented in a consistent format first in a perspective view of all three planes oriented along a consistent axis, followed by individual profiles from each plane. Table C.1 presents the order of the quantities considered. The individual profiles displayed from the the contour map are presented along horizontal planes cut by the transverse views in Appendix D and labeled 3 to 9. Profile '0' is closest profile possible to an 'input' location for each view.

U Velocity	u_x
V Velocity	u_y
W Velocity	u_z
Vertical Vorticity	ω_y
X Normal Strain	S_{xx}
Z Normal Strain	S_{zz}
X-Y Shear Strain	S_{xz}
X Reynolds Stress	u'^2
Y Reynolds Stress	v'^2
Z Reynolds Stress	w'^2
Turbulence Kinetic Energy	$\sqrt{\overline{k}}$
XY Reynolds Stress	$u\prime v\prime$
XZ Reynolds Stress	$u\prime w\prime$
YZ Reynolds Stress	$v\prime w\prime$

Table C.1: Presented PIV velocity data and derived quantities.

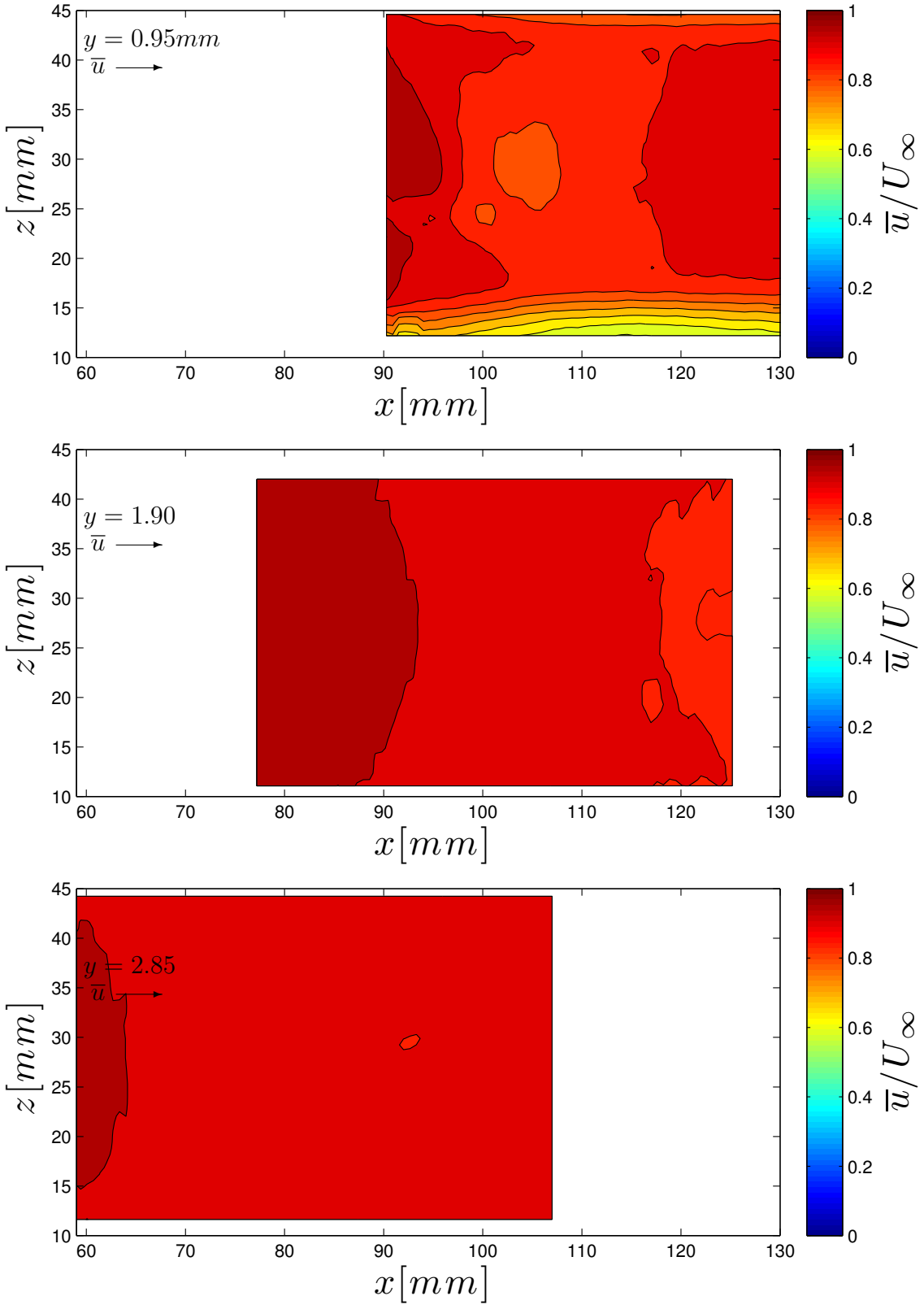

Figure C.1: Visualizations of the velocity component $\overline{u}$ for each of the three horizontal planes oriented in the streamwise direction.

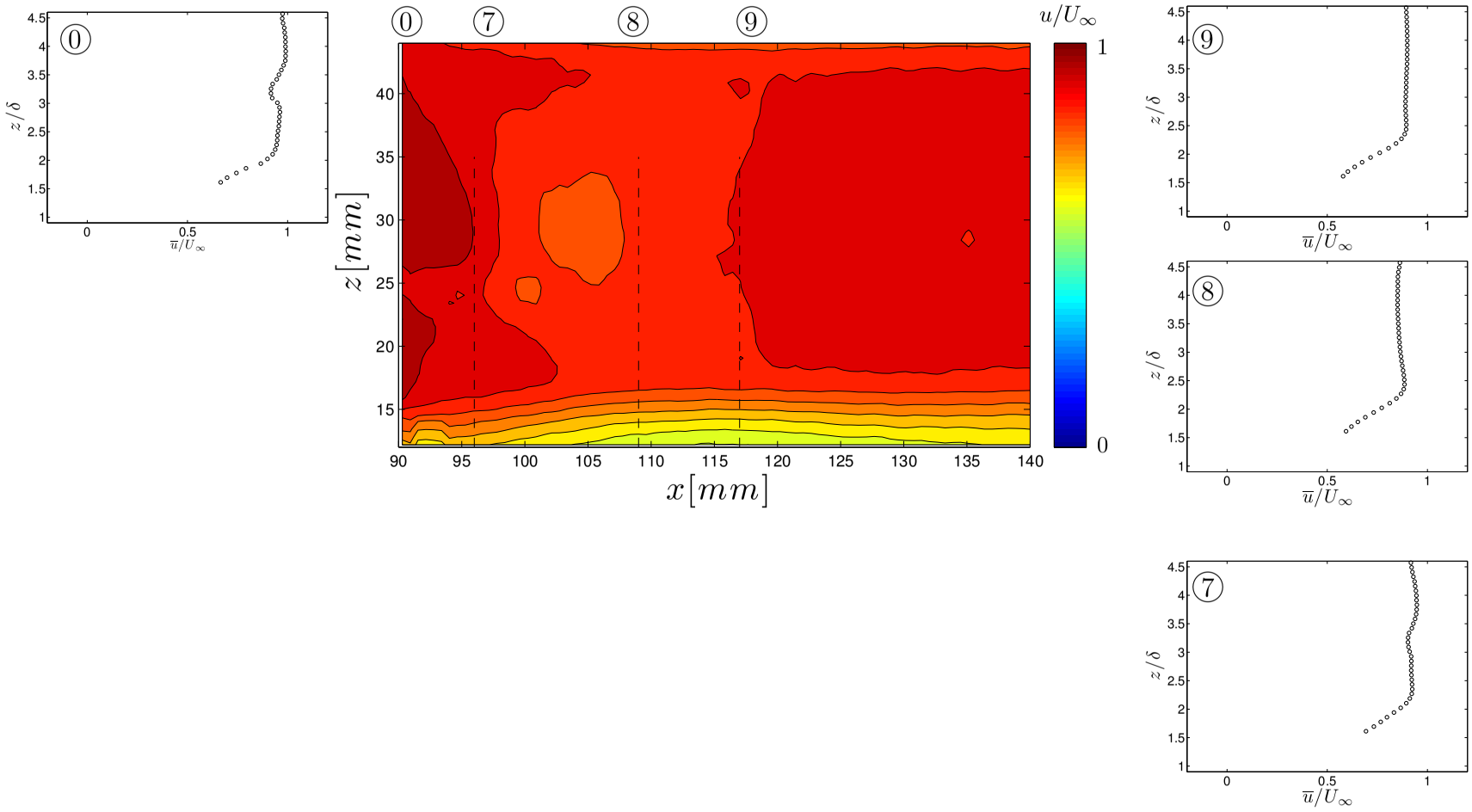

Figure C.2: Evolution of $\overline{u}$ through the y=0.95mm SBLI region for a flow deflection angle of $\theta = 6$ deg. Sampling numbers correspond to transverse plane sampling locations, location '0' indicating the region where U_∞ is calculated. At top, colors show the $\overline{u}$ field throughout each sampling plane, and also indicate their relative locations.

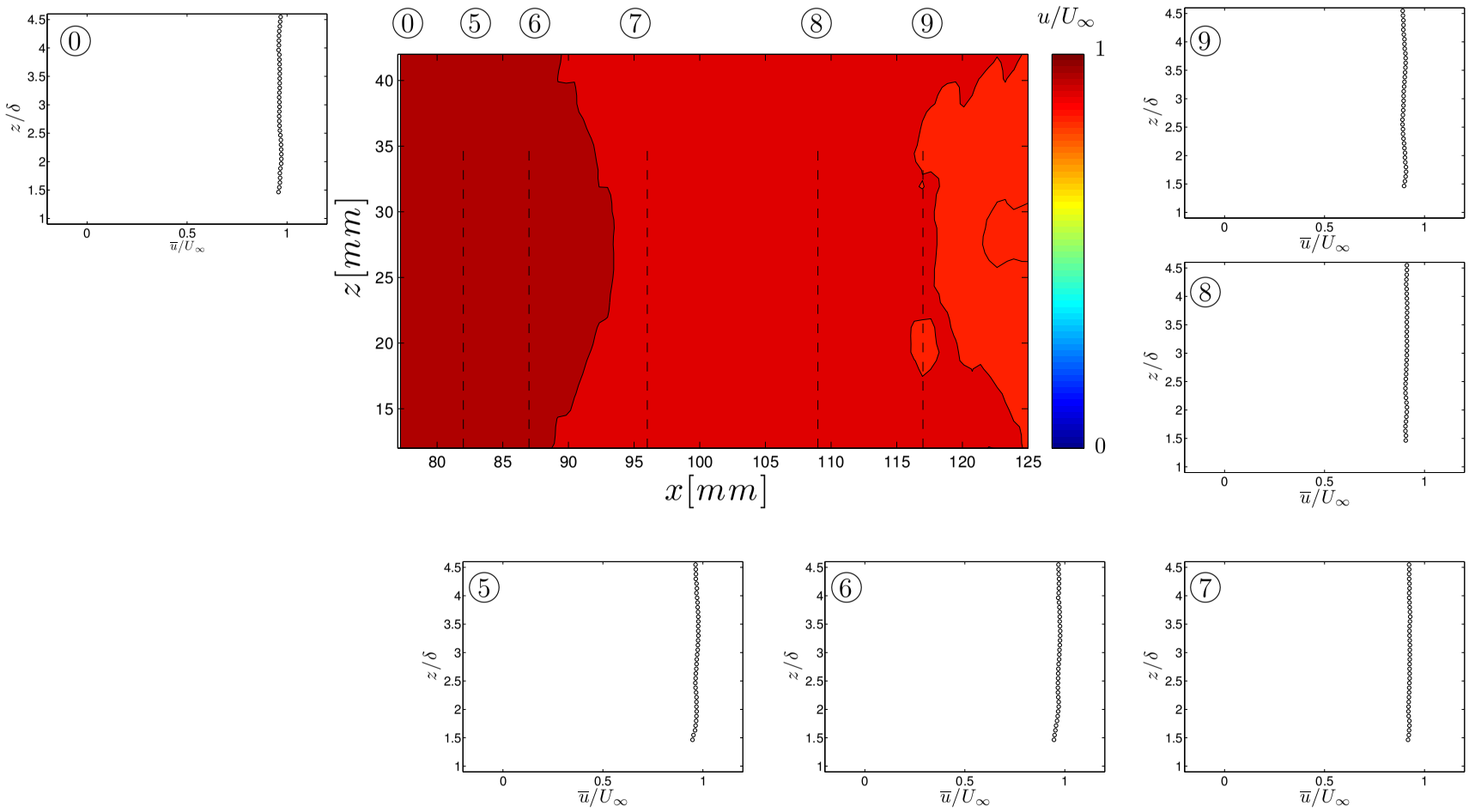

Figure C.3: Evolution of $\overline{u}$ through the y=1.9mm SBLI region for a flow deflection angle of $\theta = 6$ deg. Sampling numbers correspond to transverse plane sampling locations, location '0' indicating the region where U_∞ was calculated. At top, colors show the $\overline{u}$ field throughout each sampling plane, and also indicate their relative locations.

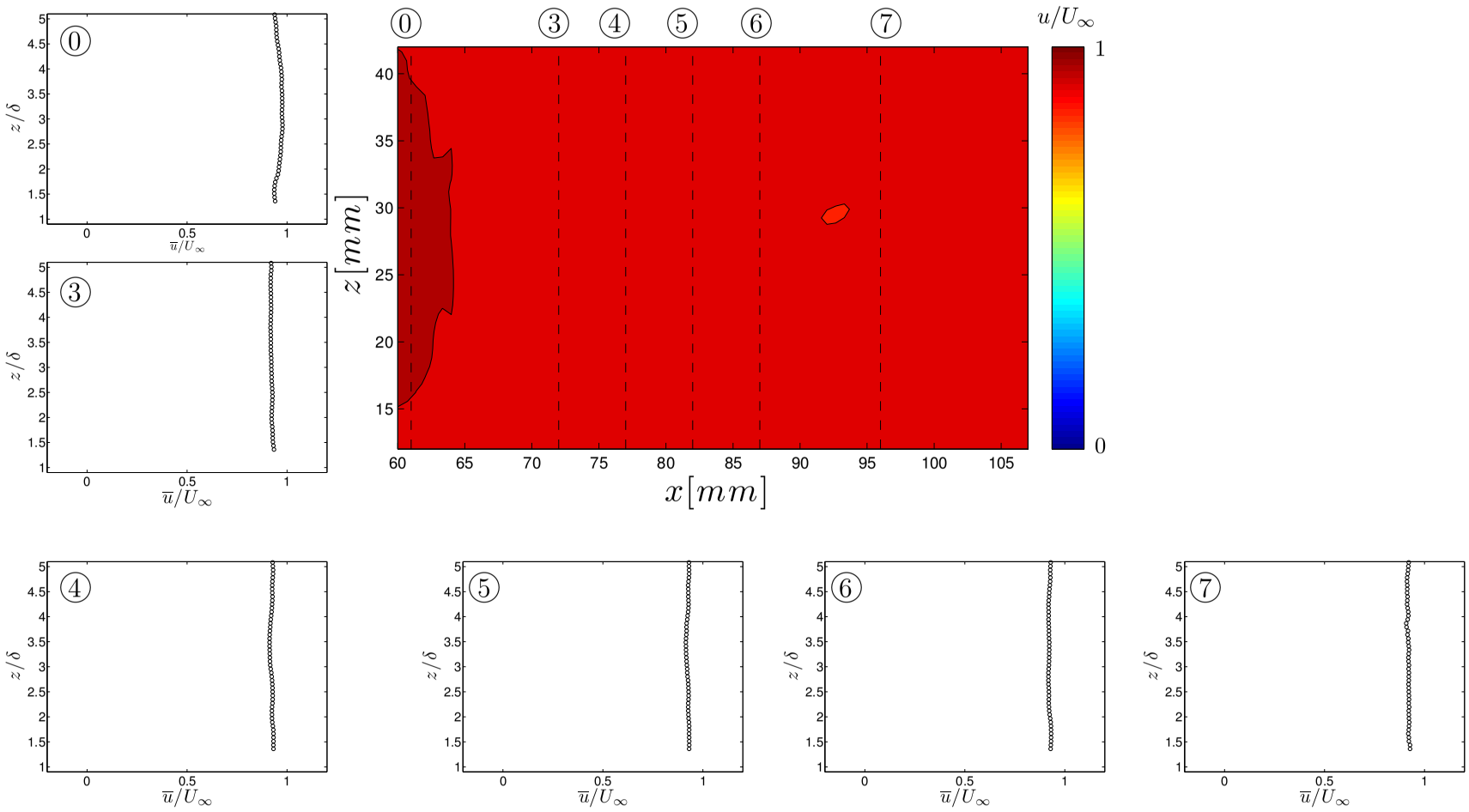

Figure C.4: Evolution of $\overline{u}$ through the y=2.85mm SBLI region for a flow deflection angle of $\theta = 6$ deg. Sampling numbers correspond to transverse plane sampling locations, location '0' indicating the region where U_∞ was calculated. At top, colors show the $\overline{u}$ field throughout each sampling plane, and also indicate their relative locations.

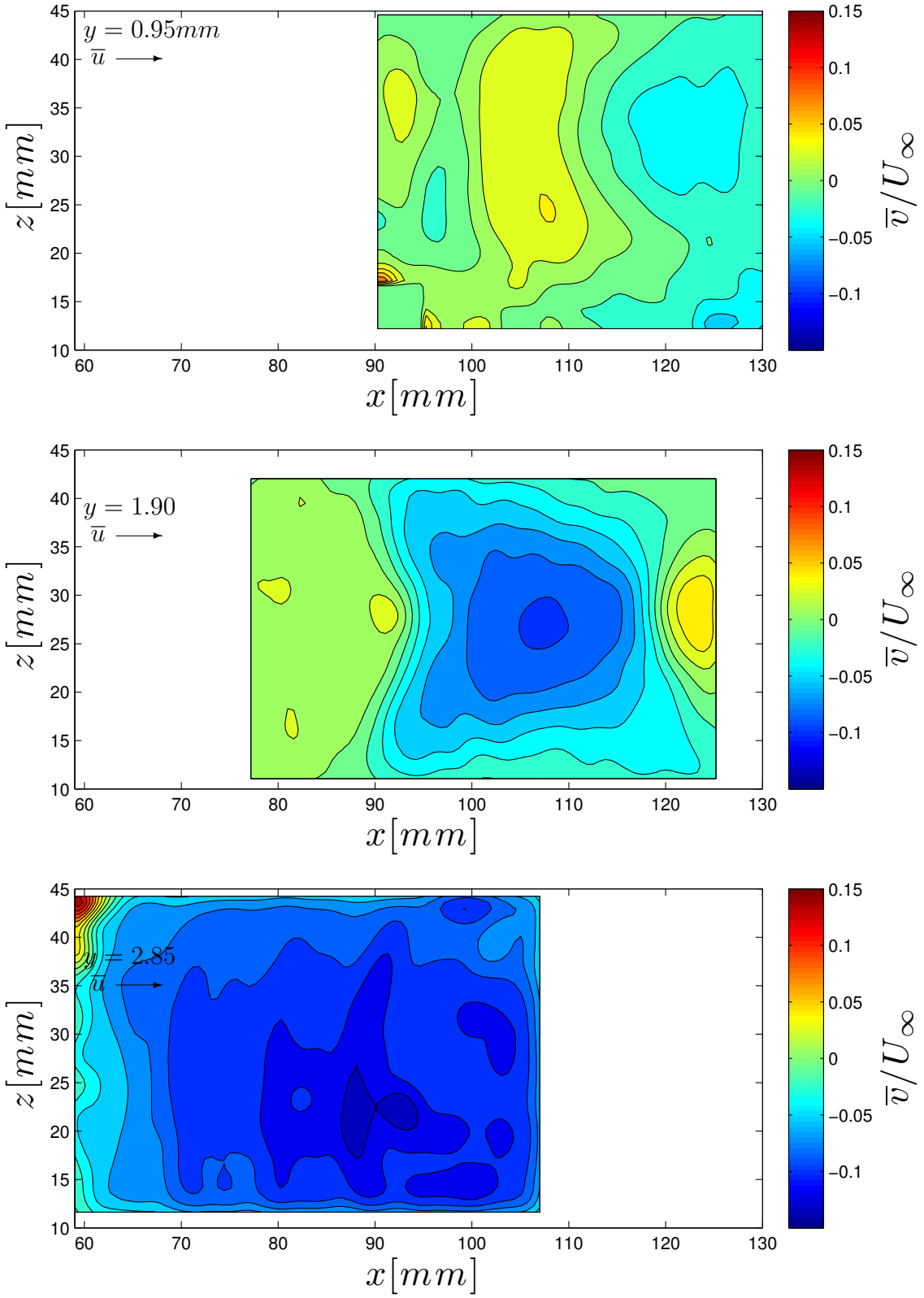

Figure C.5: Visualizations of the velocity component $\overline{v}$ for each of the three horizontal planes oriented in the streamwise direction.

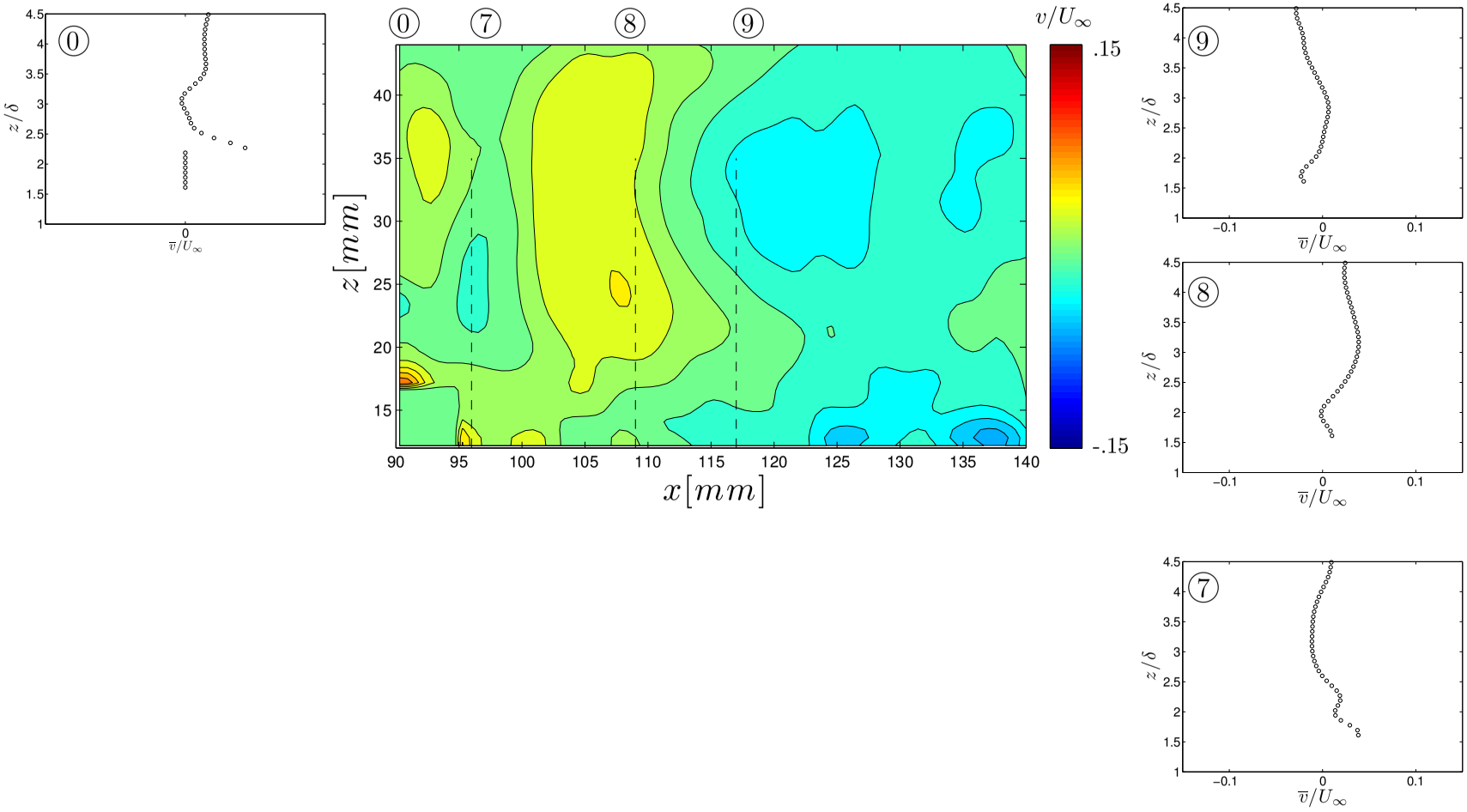

Figure C.6: Evolution of $\overline{v}$ through the y=0.95mm SBLI region for a flow deflection angle of $\theta = 6$ deg. Sampling numbers correspond to transverse plane sampling locations, location '0' indicating the region where U_∞ is calculated. At top, colors show the $\overline{v}$ field throughout each sampling plane, and also indicate their relative locations.

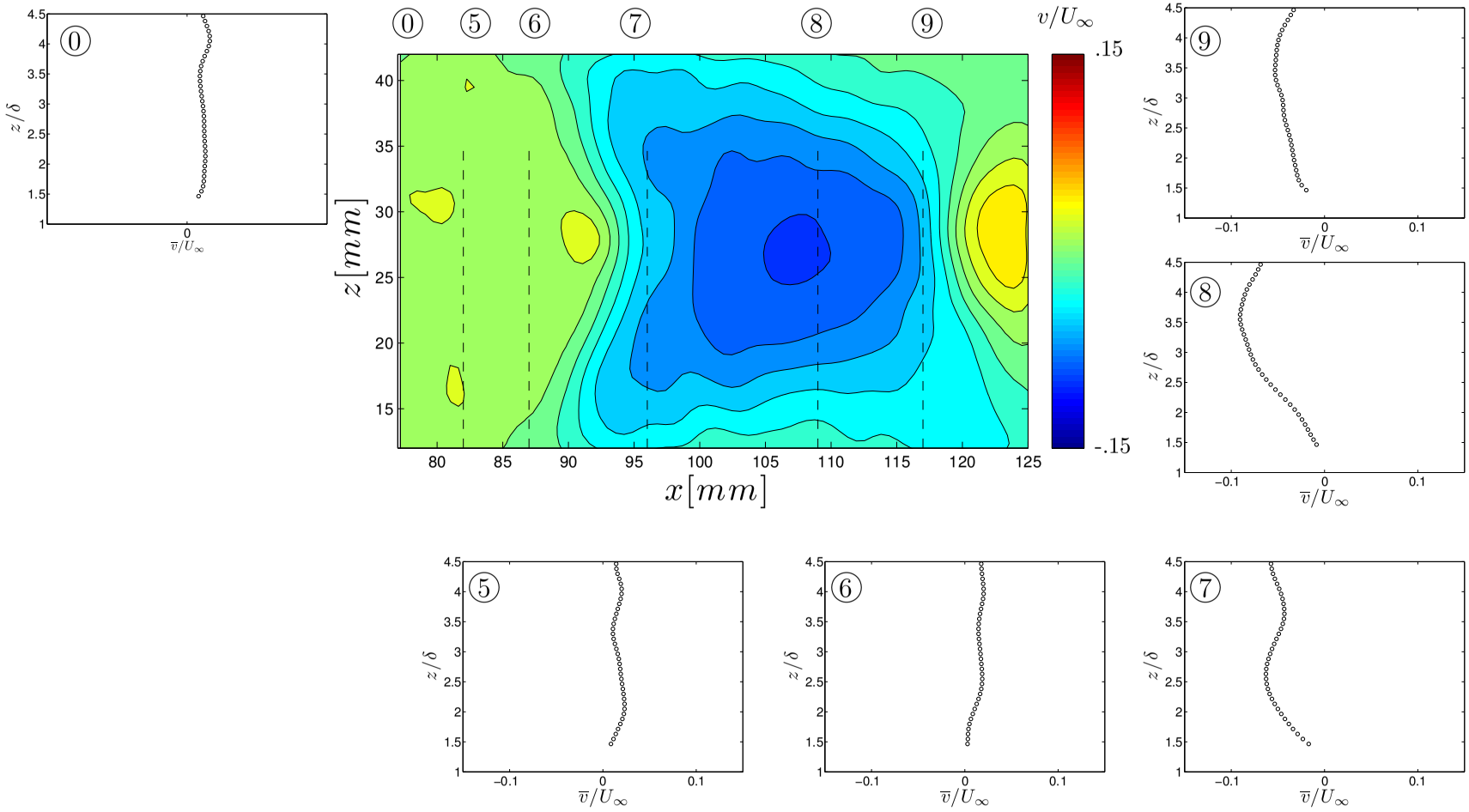

Figure C.7: Evolution of $\overline{v}$ through the y=1.9mm SBLI region for a flow deflection angle of $\theta = 6$ deg. Sampling numbers correspond to transverse plane sampling locations, location '0' indicating the region where U_∞ was calculated. At top, colors show the $\overline{v}$ field throughout each sampling plane, and also indicate their relative locations.

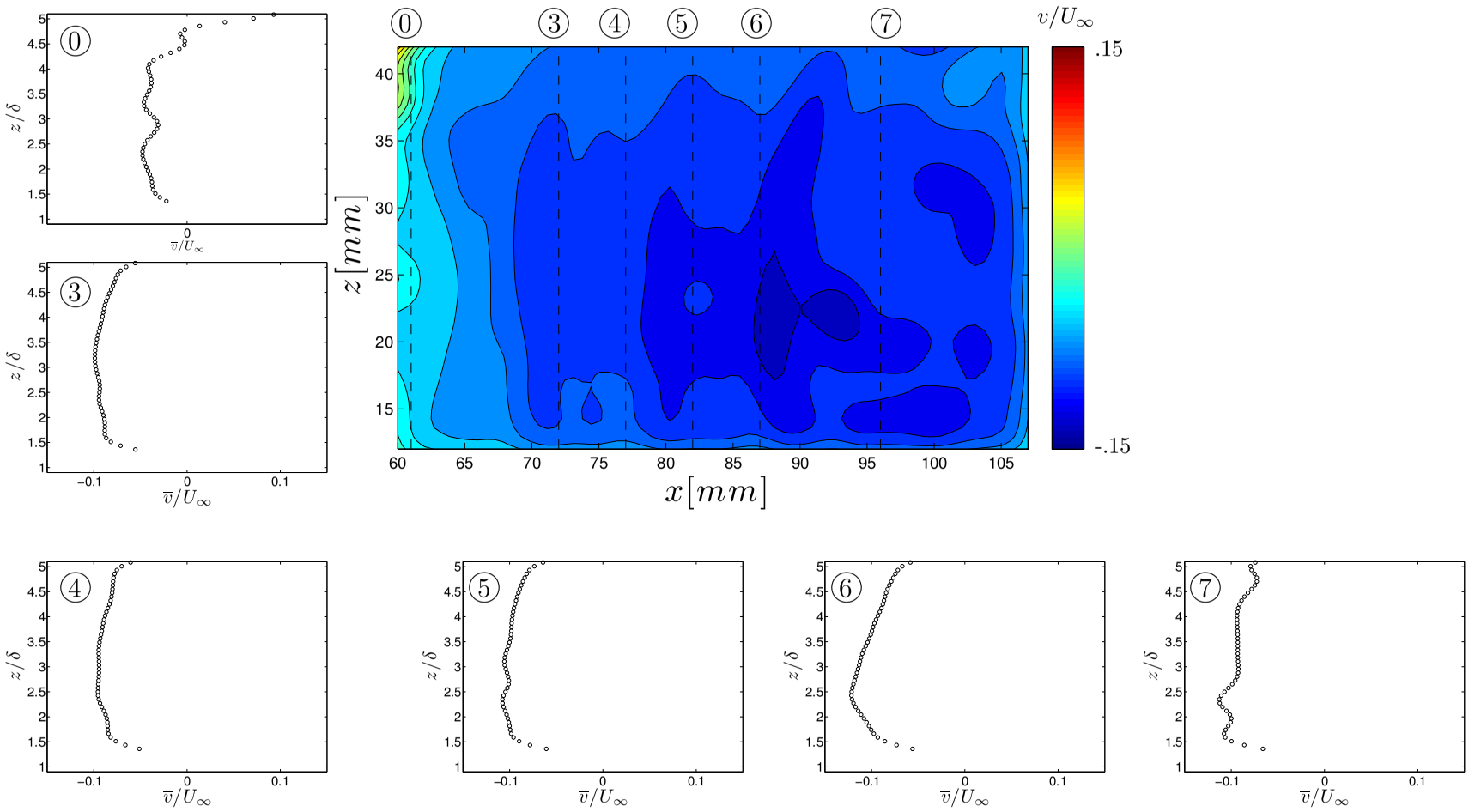

Figure C.8: Evolution of $\overline{v}$ through the y=2.85mm SBLI region for a flow deflection angle of $\theta = 6$ deg. Sampling numbers correspond to transverse plane sampling locations, location '0' indicating the region where U_∞ was calculated. At top, colors show the $\overline{v}$ field throughout each sampling plane, and also indicate their relative locations.

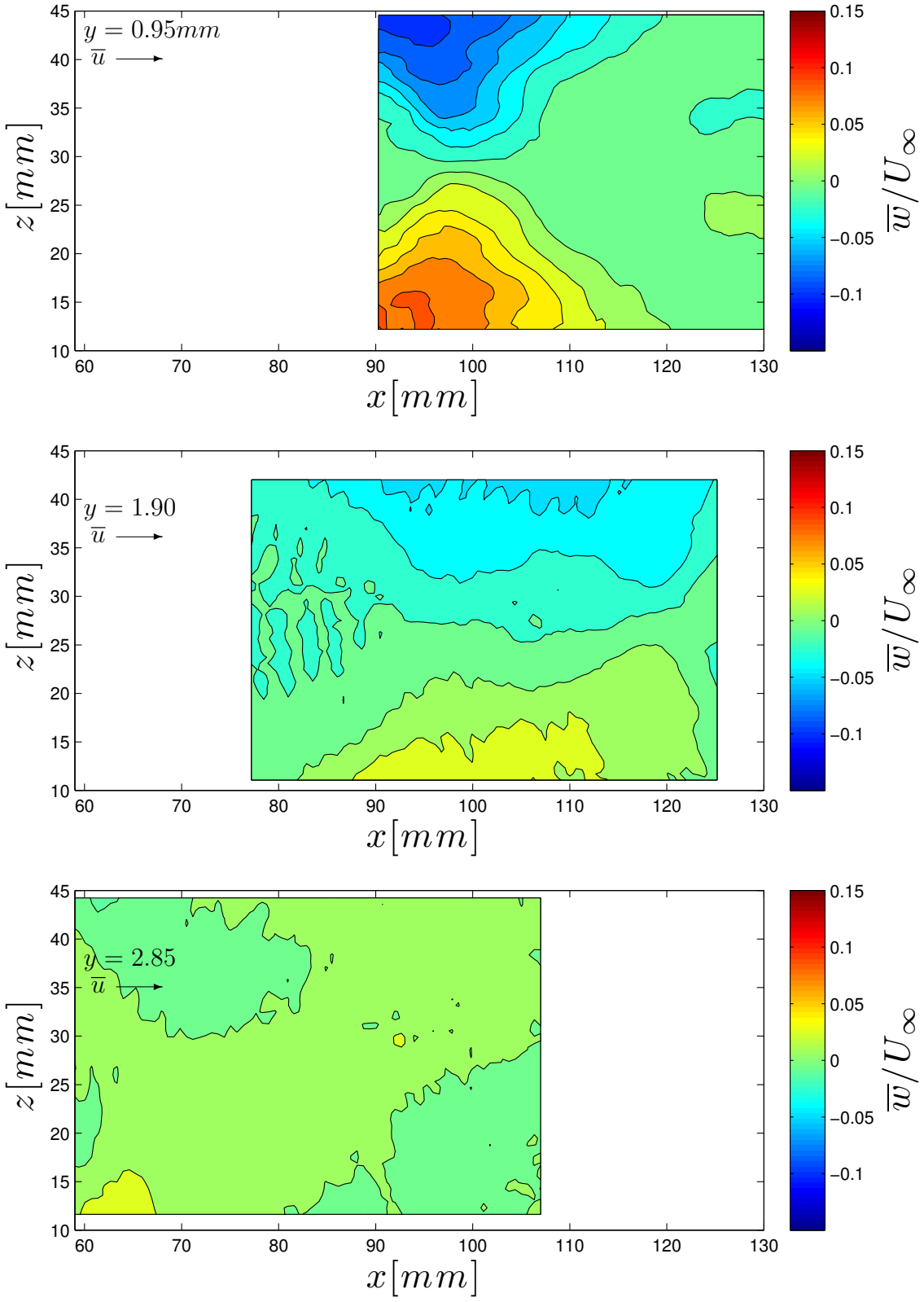

Figure C.9: Visualizations of the velocity component $\overline{w}$ for each of the three horizontal planes oriented in the streamwise direction.

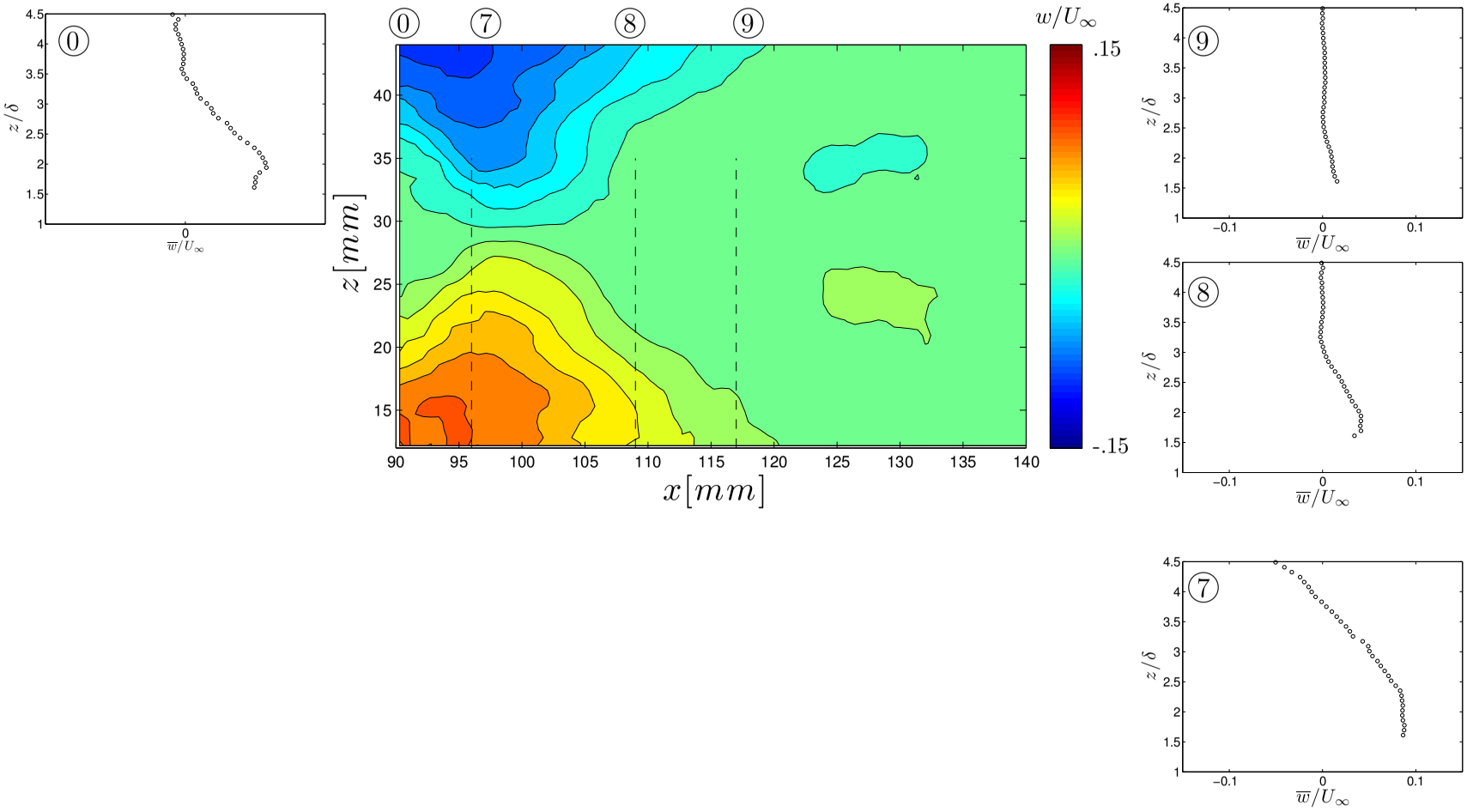

Figure C.10: Evolution of $\overline{w}$ through the y=09.5mm SBLI region for a flow deflection angle of $\theta = 6$ deg. Sampling numbers correspond to transverse plane sampling locations, location '0' indicating the region where U_∞ is calculated. At top, colors show the $\overline{w}$ field throughout each sampling plane, and also indicate their relative locations.

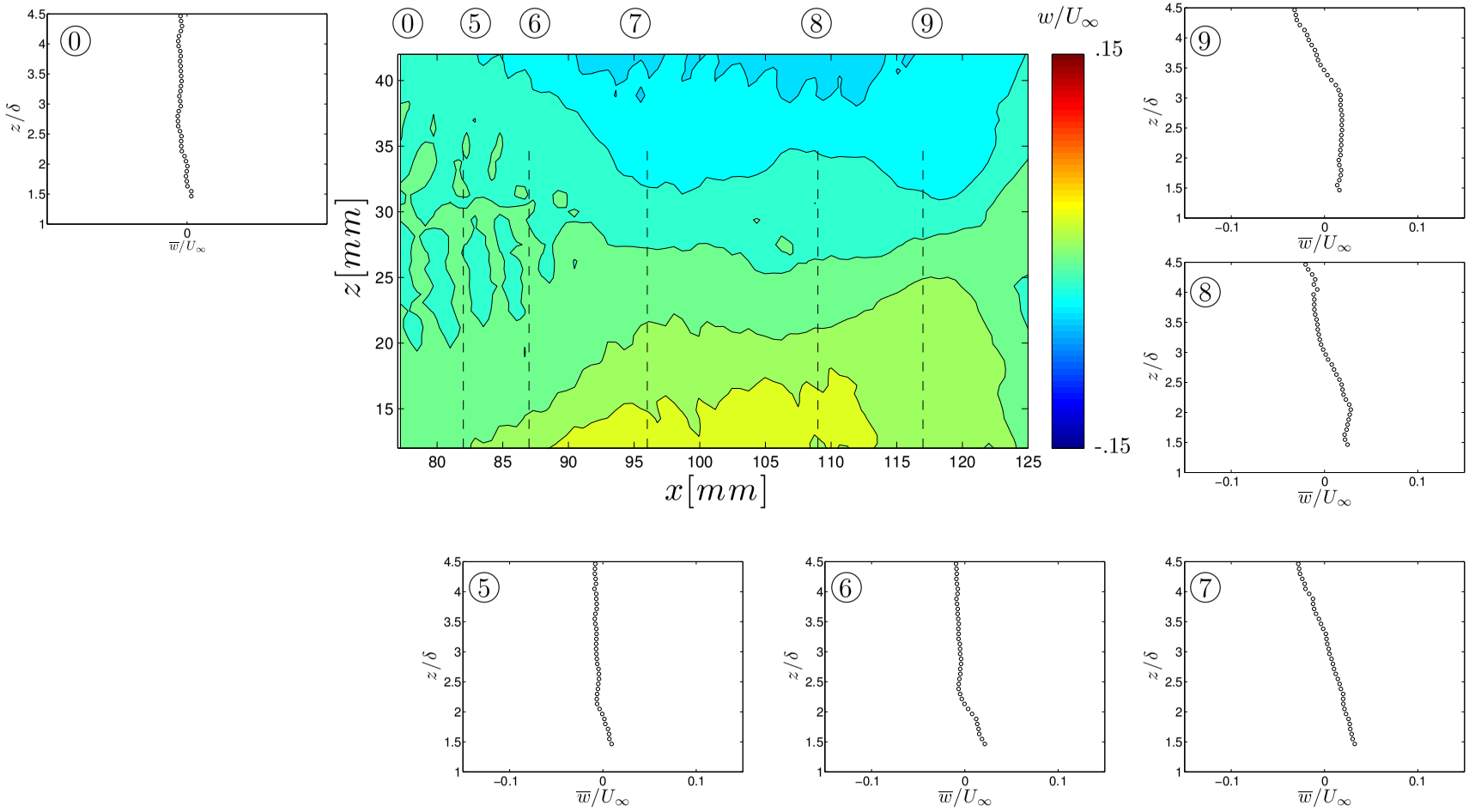

Figure C.11: Evolution of $\overline{w}$ through the y=1.9mm SBLI region for a flow deflection angle of $\theta = 6$ deg. Sampling numbers correspond to transverse plane sampling locations, location '0' indicating the region where U_∞ was calculated. At top, colors show the $\overline{w}$ field throughout each sampling plane, and also indicate their relative locations.